universität wien

MASTERARBEIT

Titel der Masterarbeit

„Exploration of matter wave interferometry in the Talbot-Lau design“

Verfasser

Xiaxi Cheng BSc.

angestrebter akademischer Grad

Master of Science (M.Sc.)

Wien, 2014

Studienkennzahl lt. Studienblatt:	A 066 876
Studienrichtung lt. Studienblatt:	Masterstudium Physik
Betreuerin / Betreuer:	Prof. Dr. Markus Arndt

Abstract

In this thesis I will describe two matter-wave interferometers, the Talbot-Lau interferometer at the University of Southampton and the Kapitza-Dirac-Talbot-Lau interferometer at the University of Vienna.
At the University of Southampton I worked on setting up a Talbot-Lau interferometer with three fixed material gratings and employed a time-of-flight technique for interference measurements.
At the University of Vienna I worked on the Kapitza-Dirac-Talbot-Lau interferometer with a central optical phase grating. Here, we demonstrated the absolute absorption cross section measurement as an application of matter-wave interferometry.

Zusammenfassung

In der vorliegenden Arbeit werden zwei Materiewellen-Interferometer vorgestellt, das Talbot-Lau Interferometer an der University of Southampton und das Kapitza-Dirac-Talbot-Lau Interferometer an der Universität Wien.
Diese Arbeit umfasst den Aufbau eines Talbot-Lau Interferometers mit drei materiellen Gittern an der University of Southampton. Die Flugzeit Technik wird angewendet, um zufünftige Interferenzmessungen zu ermöglichen.
In dem Kapitza-Dirac-Talbot-Lau Interferometer an der Universität Wien ist das mittlere materielle Gitter durch ein optisches Phasengitter ersetzt. Wir konnten damit absolute Absorptionsquerschnitte messen und damit eine neue Anwendung von Materiewellen zeigen.

Contents

Chapter 1

Introduction

The question about the nature of light dates back to the ancient Greece. Two different theories for light, the wave theory and the particle theory, have been developed over the past centuries. These two perspectives represent a cornerstone of modern quantum mechanics, the wave-particle duality. The validation of this principle is not restricted to the light. In 1923, Louis de Broglie postulated [1] a wave-particle duality for any massive object. Today, we refer to the so-called matter-wave.

Shortly after de Broglie's proposal, Davisson and Germer observed the interference of electrons reflected from a nickel surface [2]. Thomson confirmed this by observing the interference of electrons transmitted through a thin platinum plate in the same year [3]. Evidence of neutron [5] and atom interference [6, 7, 8] were found afterwards. More recently, molecules have also shown quantum interference patterns [4, 10, 11, 13, 38].

Diffraction experiments conducted in the far-field discretely visualize the wave property. However due to source brilliance it is difficult to extend those experiments to more massive objects.

However in the near-field diffraction regime, matter-wave interferometers in the Talbot-Lau design stand out as promising candidates to probe the wave property of large molecules. Without the need for a highly collimated particle beam and a spatially resolving detector, experiments using Talbot-Lau interferometer (TLI) proved its advantages by measuring the interference pattern of potassium atoms

[12]. Our group at the University of Vienna demonstrates quantum interference for molecules. Using the Kapitza-Dirac-Talbot-Lau interferometer [41] (KDTLI), a newer version of the Talbot-Lau interferometer with an optical phase grating as the central diffraction grating, the group broke and reset the mass record of molecules showing interference repeatedly. The current mass record exceeds 10000 u [43]. Testing the wave property of massive particles gives deeper insight into the quantum superposition principle and decoherence [16, 50, 56]. It also enables studies of molecular internal properties [18, 44, 64, 77] and inertial force sensing [57]. This new area of quantum enhanced metrology has proven its bright future. Recently, another Talbot-Lau interferometer has been established by Hendrik Ulbricht at the University of Southampton.

My master's thesis is divided into two parts. The first part covers the project of setting up a Talbot-Lau interferometer at the University of Southampton during my year abroad. Chapter 2 briefly reviews the conceptual basis for the theoretical background. It shortly covers the theoretical treatment of the Talbot-Lau interferometer using Wigner formalism and compares the quantum mechanical prediction with the classical prediction. The experimental setup is described with a detailed specification of critical components in chapter 3. The concept of measuring the interference pattern using time-of-flight technique is presented by a numerical simulation in chapter 4 where the data analysis and an extensive discussion are provided.

At the University of Vienna I continued my thesis working on a Kapitza-Dirac-Talbot-Lau interferometer, as described in the second part. In a short theory chapter 5, I will review the conceptual difference between the TLI and the KDTLI in the theoretical analysis. Due to the similarity between the two experimental setups, only the different components are described in chapter 6. Chapter 7 covers the measured interference patterns of C_{70}, $\beta-$carotene and resveratrol. In chapter 8, we experimentally demonstrate an application of the KDTLI for the absolute absorption cross section measurement using momentum transfer by photon recoil [44]. The main advantages of this technique are the high precision in the estimate and the relaxed interferometer conditions.

Part I

The Talbot-Lau interferometer (Southampton)

Chapter 2

Theory of the Talbot-Lau interferometer

In this thesis, we will be working with near-field matter-wave interferometers in the Talbot-Lau design. Before diving into the theory of the Talbot-Lau interferometer let us shortly review some basic concepts.

2.1 Coherence

Coherence describes a property of the correlation between physical quantities of a single wave, or several waves. It can be understood as the requirement to observe stationary interference of waves. In most cases, coherence is related to a phase relation between waves.
There are two types of coherence, temporal (longitudinal) and spatial (transversal) coherence. Temporal coherence describes the interference between the fields of a wave observed at different times. The temporal coherence is present if the phase difference at the certain delay time remains constant at any time. The time duration where the variance of the phase difference $\Delta\phi$ remains below π is called the coherence time. Specifically for light, the distance which the light covers within the coherence time is defined as the coherence length.
The spatial coherence describes the interference between the fields of waves at different points in space. Two points in space are spatially coherent if the phase

difference at these points is constant at any time. However, the spatial coherence is more important for the matter-wave interferometers mentioned in this thesis.

2.2 Diffraction in the far-field and the near-field

The Kirchhoff-Fresnel diffraction integral describes diffraction at any arbitrary aperture. The resulting interference pattern can be understood as constructive and destructive interference of spherical waves emitted from each position of the aperture [15].
Here, we distinguish between diffractions in the far-field and in the near-field. Far-field diffraction (or Fraunhofer diffraction) occurs if the phase contribution of each point of the diffraction aperture can be approximated by a linear function. This is valid if the distance between the image and the aperture exceeds the characteristic distance a^2/λ with aperture diameter a and the incident wavelength λ [15].
At the smaller distance between the image and the aperture near-field (Fresnel) diffraction takes place, when the front curvature of the spherical waves cannot be ignored.
Interferometers based on far-field diffraction appear first to be conceptually the simplest method to test the wave property of particles. But, it requires such a highly collimated particle beam that the collimation angle has to be smaller than the diffraction angle. An increase in beam collimation would reduce drastically the intensity of the particle beam. This source issue makes far-field experiments with larger objects more difficult.
In contrast, interferometers based on near-field phenomena have the advantages of relaxed collimation of the particle beam and coherence condition on source [15]. Let us review the fundamental effects in the following sections, individually.

2.3 Talbot effect

The Talbot effect is a near-field effect and is named after Henry Fox Talbot who first observed this effect in 1836 for light. Fig. 2.1(a) illustrates the idea schematically. When a grating of period d is illuminated by a plane monochromatic wave

constructive and destructive interference create an intensity modulation of the same period d after the grating. However, this lens-less self-imaging effect happens at certain distances, called the **Talbot length** L_T which is given by

$$L_T = \frac{d^2}{\lambda} \tag{2.1}$$

where λ is the wavelength of the plane wave. The same interference pattern occurs for any integer n multiple of the Talbot length in the near-field regime. There is a half-periodic shift in position between the patterns at even and old orders of the Talbot length, as seen in Fig. 2.1(a). Additional patterns with higher periodicities

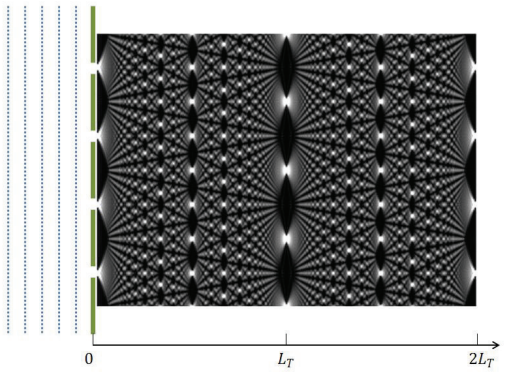

(a) Illustration of the Talbot effect. Figure taken from Ref. [53] and modified by author.

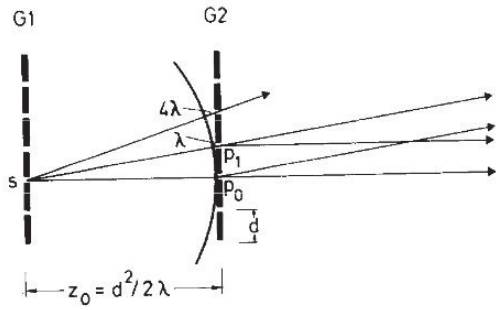

(b) Illustration of the Lau effect. Figure taken from Ref. [22].

Figure 2.1: In (a) diffraction of plane waves (blue dashed line) at a grating results in periodic interference structures with an intensity modulation of the grating period at any integer multiple of L_T. In (b), each slit opening S of the first grating (G1) can be seen as a line source which coherently illuminates the slits of the second grating (G2) with a grating separation z_0. The slits at positions P_0, P_1 behave like coherent secondary sources. One possibility to add up the resulting interference patterns position-synchronously is to choose the periods of the gratings equally, as shown in (b).

are visible at any rational fractions of the Talbot length [21]. The wavelength λ can be replaced by the de Broglie wavelength $\lambda_{\mathrm{dB}} = h/p$ for matter-waves, where $p = mv$ is the momentum of the particle with mass m and velocity v. For this

reason, the purity of the source becomes one important limiting factor for high interference contrast while the velocity class can be manually selected.

2.4 Lau effect

Different from the coherent grating illumination in the Talbot effect, the Lau effect describes grating illumination by coherent spherical waves [23]. Let us first image having two gratings placed at a distance L between each other and consider each opening of the first grating as a line source emitting cylindrical waves. If the grating separation is $L = d^2/2\lambda$ these waves coherently illuminate the second grating. The slits of the second grating become coherent and a geometric illustration is given in Fig. 2.1(b). At infinity an interference pattern can be observed behind the second grating. However, if the line sources given by the first grating have the same periodicity as the diffraction grating, the interference fringe pattern will overlap position-synchronously. This is also observable for any integer numbers of $d^2/2\lambda$. In the near-field regime, this effect can also be explained using the van Cittert-Zernike theorem [24] which implies that the spatial coherence Δr produced by a source with an opening width a at the distance L is given by

$$\Delta r \approx \frac{L\lambda}{a}. \tag{2.2}$$

In order to observe interference, the spatial coherence needs at least to exceed two grating periods.

2.5 Talbot-Lau interferometer

Our near-field interferometers are based on the Talbot and the Lau effect. Fig. 2.2 illustrates the setup of the Talbot-Lau interferometer. A particle beam with a moderate collimation propagates through three parallel material gratings. The first grating prepares required spatial coherence. The second grating prepares a superposition state for the interference. In order to observe the periodic near-field self-imaging after the second grating, the third grating is moved laterally across the molecular beam and the transmitted signal is detected. This interferometer has

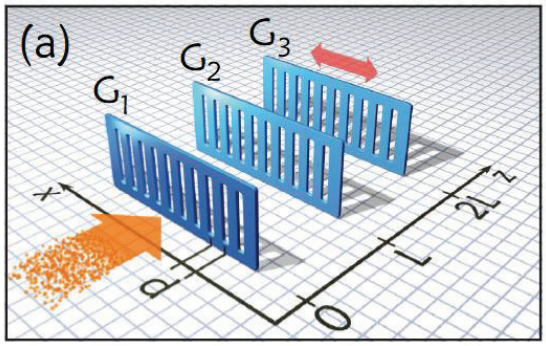

Figure 2.2: The TLI consists of three identical material gratings, denoted by G_1, G_2 and G_3. Figures taken from Ref. [19].

the main advantage that the requirement of a coherent source is overcome by using the three-grating configuration which however is accompanied by a more advanced alignment precision. A theoretical description based on Wigner functions permits a transparent representation of all relevant effects in a closed form. An extensive theoretical study is available in Ref. [29, 30, 71].
First of all, let us review the necessary tools. Wigner function is a real function in phase space which can be positive and negative and includes many features of a classical probability density function. It is defined by [70]

$$w(\mathbf{r},\mathbf{p}) = \frac{1}{(2\pi\hbar)^2}\int d\mathbf{s} e^{i\mathbf{p}\mathbf{s}/\hbar}\rho\left(\mathbf{r}-\frac{\mathbf{s}}{2},\mathbf{r}+\frac{\mathbf{s}}{2}\right) \tag{2.3}$$

where $\mathbf{r}$ and $\mathbf{p}$ are the transversal position and momentum, respectively and ρ is the spatial density matrix. The free propagation in the z-direction over the distance L can be described in terms of the initial Wigner function $w(\mathbf{r},\mathbf{p})$ by means of the shearing-displacement transformation

$$w_L(\mathbf{r},\mathbf{p}) = w\left(\mathbf{r}-\frac{L}{p_z}\mathbf{p},\mathbf{p}\right). \tag{2.4}$$

The passage through a grating is given by the convolution with the grating kernel function $T(\mathbf{r},\mathbf{p})$. The Wigner function directly after a grating has the form [70]

$$w'(\mathbf{r},\mathbf{p}) = \int d\mathbf{q} T(\mathbf{r},\mathbf{p}) w(\mathbf{r},\mathbf{p}-\mathbf{q}) \tag{2.5}$$

with

$$T(\mathbf{r},\mathbf{p}) = \frac{1}{(2\pi\hbar)^2}\int d\mathbf{s} e^{i\mathbf{p}\mathbf{s}/\hbar} t\left(\mathbf{r}-\frac{\mathbf{s}}{2}\right) t^*\left(\mathbf{r}+\frac{\mathbf{s}}{2}\right) \tag{2.6}$$

where $t(\mathbf{r})$ is the grating transmission function.

Let us now simplify the situation by taking a symmetric Talbot-Lau setup with three identical material gratings where the distances between two neighbouring gratings are equal and denoted by L. In the case of an uncollimated monochromatic beam, the normalized one-dimensional Wigner function before the first grating w_0 is given by [70]

$$w_0(x,p) = 1. \tag{2.7}$$

Due to the periodicity of the binary transmission function of the first grating of period d we can describe it by a Fourier series $t_1(x) = \sum_m a_m \exp(2\pi i m x/d)$ which only takes the value 0 or 1. The Fourier coefficient is given by $a_m = f \cdot \mathrm{sinc}(\pi f m)$ with opening fraction f. After the first grating, the density function has the form [70]

$$w_1(x,p) = |t_1(x)|^2 = \sum_l A_l \exp\left(2\pi i l \frac{x}{d}\right) \tag{2.8}$$

with $A_l = \sum_j a_j a_{j-l}^*$. Since the second grating has the same transmission function as t_1 we denote its Fourier coefficient by b_m and describe the convolution kernel by [70]

$$T(x,p) = \sum_{l,j} b_j b_{j-l}^* \exp\left(2\pi i l \frac{x}{d}\right) \delta\left(p-(j-l/2)\frac{h}{d}\right). \tag{2.9}$$

For simplicity, we use the same transmission function for the third grating as for the first grating, $t_3 = t_1$. The transmitted signal $S(x_s)$ after the third grating is a function of the third grating position x_s [70]

$$S(x_s) \propto \sum_l (A_l^*)^2 B_{2l}\left(l\frac{L}{L_T}\right) \exp\left(2\pi i l \frac{x_s}{d}\right) \tag{2.10}$$

where $B_l = \sum_j b_j b_{j-l}^* \exp\left(i\pi \frac{l^2-2jl}{2}\frac{L}{L_T}\right)$ is a function of Talbot length L_T and therefore velocity-dependent. In order to characterize the interference pattern we use

the parameter Visibility [70]

$$\mathrm{Vis} = \frac{S_{\max} - S_{\min}}{S_{\max} + S_{\min}} \tag{2.11}$$

where $S_{\max}$ and $S_{\min}$ are the maximum and the minimum of Eq. 2.10, respectively.

2.5.1 Molecule-grating interaction

The interaction between the molecules and the grating walls can not be neglected. It depends on the thickness and the material of the grating, the position and the velocity of the molecules. As a good approximation [32], the gratings can be described by an absorptive mask and a phase modulation. The binary transmission function $t(x)$ of the grating will include a phase factor depending on the interaction potential V, the velocity v_z ($p_z = mv_z$) and the mass m of the molecule. The new transmission function is given by [70]

$$t'(x) = t(x) \exp\left(-\frac{im}{\hbar p_z} \int dz V(x,z)\right). \tag{2.12}$$

Our main concern is the attractive dispersion potential. In general, it is inappropriate to describe this dispersion potential between the polarizable particle and the material surface only by an attractive van der Waals potential $V_{\mathrm{VdW}}(x) = -C_3/x^3$ which appears to be valid for close distances $x \to 0$. We find a "retarded" Casimir-Polder potential $V_{\mathrm{CP}} = -C_4/x^4$ [33] would be more suitable for large distances $x \to \infty$. The exact force is a combination of both potentials [30]. Fig. 2.3 illustrates the effect of this interaction on the molecular interference fringe visibility averaged over 4% velocity spread. The blue curve indicates the simulation with ideal absorptive grating without any additional potential. Orange and pink curve simulate the visibility with either van der Waals or Casimir Polder potential considered for the molecule C_{60} with SiN_x gratings, respectively. Using the exact force law the simulation shows that the interaction can be approximated fully by the van der Waals interaction, as shown in dotted curve.
Attractive forces tend to decrease the effective opening fraction of the grating [30] and this effect becomes more influential with increasing molecular polarizability and lower velocity. This results in a decrease of the peak width of the orange curve

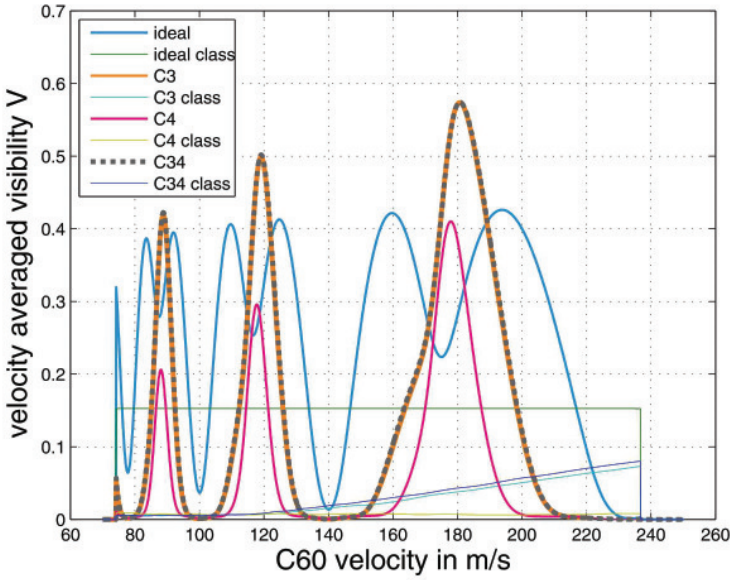

Figure 2.3: A numerical simulation of the visibility as a function of velocity for C_{60} averaged over 4% velocity spread. The simulation is calculated with the parameters (grating period d = 257 nm and thickness b = 190 nm) of our experimental setup with ideal absorptive grating (blue), with van der Waals potential (orange), Casimir Polder potential (pink) and with the exact force (dotted). In comparison, the classical visibility are plotted in thin lines for each cases. Figure taken from Ref. [53].

in Fig. 2.3 which simultaneously leads to a stricter requirement of the velocity selectivity to observe high visibility [41, 48]. For even stronger interactions, the wave front distortion can no longer be described by an additional phase shift alone [71] and the situation becomes more complicated. For these reasons it is appealing to replace the material diffraction grating by a standing light wave, see section 5.2. This additional phase is irrelevant in the first and the third grating because the transmitted signal $S(x_s)$ only depends on the absolute value of the grating transmission functions $|t_1|^2$ and $|t_3|^2$. One can understand this by imagining each slit of the first grating as a point source. Any imprinted phase within the slit can be seen as a global phase which does not influence the interference. At the third grating the additional phase does not influence the visibility since only the total transmitted signal is relevant for the measurement.

2.6 Classical Moiré fringes

A molecular density distribution similar to the quantum interferogram can be explained by the classical Moiré shadow [30]. Interference pattern with a significantly higher visibility than the classically predicted pattern would be sufficient to exclude the possibility of classical phenomena. Therefore, let us take a closer look at the theoretical prediction of the classical visibility.
The classical and the quantum mechanical calculations are similar. However, the convolution kernel differs [30]. For **TLI** with ideal gratings, the classical convolution kernel is given by

$$T_{\mathrm{cl}} = |t_2(r)|^2 \delta(p) \tag{2.13}$$

which also leads to the general expression Eq. 2.11. The only exception is that the Fourier coefficient $B_l = \sum b_j b^*_{j-m}$ becomes velocity independent. The expected density pattern is the same in the quantum mechanical and classical case as long as the grating separation L is an integer multiple of the Talbot length [30]. However, distinctive differences stand out for other velocities, i.e. $L/L_T \neq \mathbb{N}$ or $\lambda_{\mathrm{dB}} \neq nd^2/L$.
However more realistically, when grating material-molecule interactions are considered situation changes tremendously, as shown in Fig. 2.3. Only a small velocity dependence appears in the classical calculation. The quantum mechanical calculation yields in general a significantly different result for any velocity.
Hence, we conclude whenever the results of an observation exceed the classical limitation quantum interference takes place.

Chapter 3

Experimental setup

In this chapter, I will describe the experimental setup of the Talbot-Lau interferometer (TLI) at the University of Southampton. Interference measurement using time-of-flight technique will be presented in a theoretical analysis. A comparison between the theoretical results and the measurement data[1] shows a possible trace of interference.

Fig. 3.1 shows the experimental setup of the Talbot-Lau interferometer. It is divided into two vacuum chambers, the oven and the interferometer chambers. The oven chamber accommodates a resistively heated oven, a rotating chopper and a skimmer. It is separated from the interferometer chamber by a valve for fast vacuum recovery after each oven reload. The three-grating interferometer is located in the centre of the interferometer chamber, together with three additional slits for a better beam collimation. The transmitted signal is detected by a quadrupole mass spectrometer (QMS) combined with electron impact ionization at the end of the interferometer chamber (Fig. 3.1). The whole interferometer is positioned vertically. The distance between the oven orifice and the QMS is 1.74 m while the entire apparatus has a total height of 2.5 m. It is mounted in an Aluminium rig floated on four laminar float isolators (Newport I2000 series) for vibration isolation. A small optics bench is positioned on top for grating alignment, see section 3.3.2.

[1] Measurement data obtained upto 01.09.2013

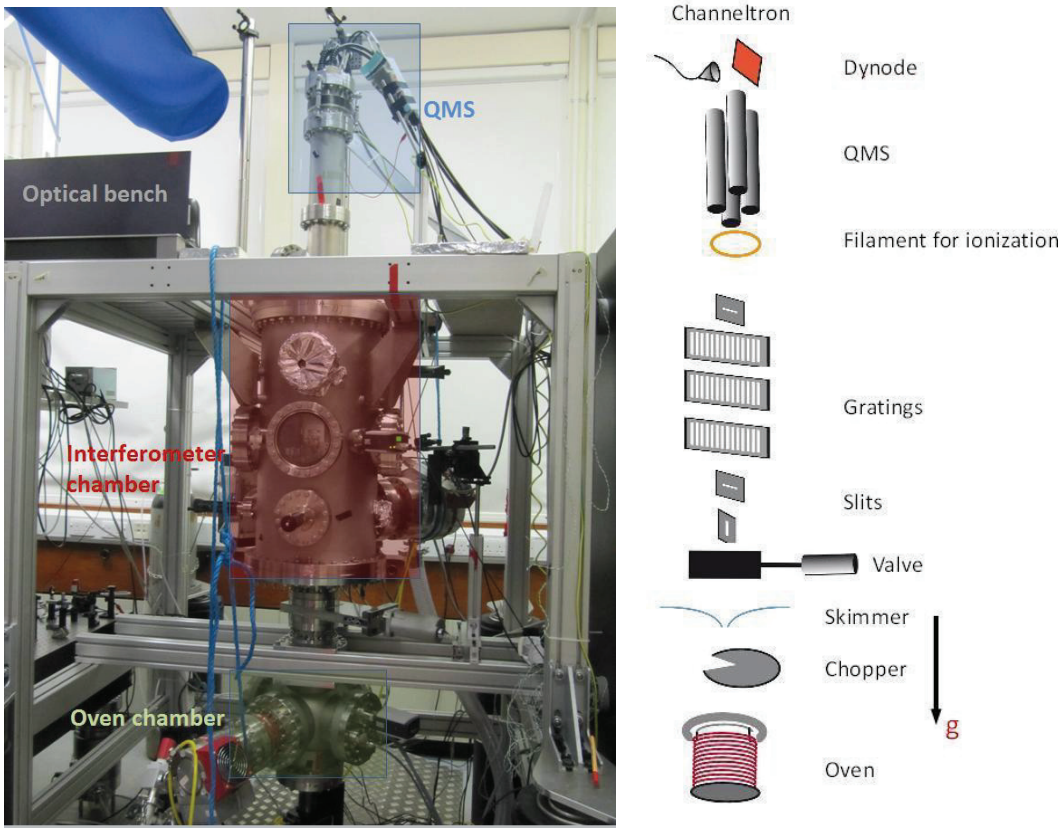

(a) The TLI at the University of Southampton

(b) Schematic of the TLI

Figure 3.1: The experimental setup of the Talbot-Lau interferometer is divided into an oven chamber and an interferometer chamber where the QMS is connected to the interferometer chamber by a thin tube as illustrated in (a). An optical bench for the alignment laser is mounted on top of the rig. All important components of the TLI are illustrated in (b).

3.1 Oven chamber

The oven chamber is made of a six-way-cross vacuum chamber. A molecular oven 3.1.2 is attached at the bottom of the chamber. It can be aligned by a x-y-z translation stage. A rotating chopper [31] modulates the molecular beam before it is directed into the interferometer chamber through a skimmer with an 1 mm diameter. A turbo pump (Pfeiffer HiPace 300) is used in combination with a pre-

pump (Edwards Two Stage 28) to reach the conventional pressure at the operation of $5 \cdot 10^{-7}$mbar.

3.1.1 Molecules

Quantum interference has been observed for various molecules[9, 11, 13, 35, 36, 37, 38, 39, 40, 41, 42, 43]. A large amount of molecules (dozens of milligrams) is necessary. Since the interference pattern is on nanometre scale the drift of the scanning grating needs to be better than 10 nm/min. An intense beam shortens the data acquisition time which makes the effect of grating drift negligible.
C_{60}[2] appears to the perfect candidate. It has a diameter of 1 nm including the π-electron clouds. Its high binding energy of 7 eV/carbon [49] with 174 internal degrees of freedom provide a high structural stability and a sufficiently long energy storage time[3] [45]. A resistively heated oven can easily bring C_{60} into gas phase via sublimation at 580°C without significant fragmentation. Fullerenes are easily ionized by the thermally emitted electron ionization.

3.1.2 Oven structure

Fig. 3.2 illustrates the structure of the oven. The molecules are contained within a Shapal ceramic cell (blue) with an inner volume of 5 mm diameter and 2 cm height. Because of the excellent thermal conductivity, the high electric resistance and low thermal expansion, this Shapal ceramic cell is wound homogeneously by Tantalum heating wires of a diameter of 0.12 mm with a resistance of roughly 10 Ω[4] at room temperature. The Shapal cell is closed by a removable orifice (orange) with a pinhole of 0.5 mm diameter and 1 mm thickness, also made of Shapal[5]. The complete cell is then surrounded by a Macor[6] glass-ceramic cover with a wall

[2]purchased from Sigma-Aldrich Co. LLC with a purity of 99.5%+

[3]Extensive studies of thermal emission of radiation of hot fullerene were carried out between 2000 K and 3000 K in Ref. [49] and also decoherence effect by thermal radiation has been observed at a temperature over 1000 K [50].

[4]Since the thin Tantalum wire is mechanically fragile, we occasionally replaced it by a Nicroalloy B wire (Ni: 65%, Cr: 15% balanced with Fe) of 0.4 mm diameter.

[5]In order to increase the volume for vapour pressure, the bottom plate with a bigger pinhole is removed in the actual setup.

[6]Low thermal conductivity, electric isolating, low thermal expansion

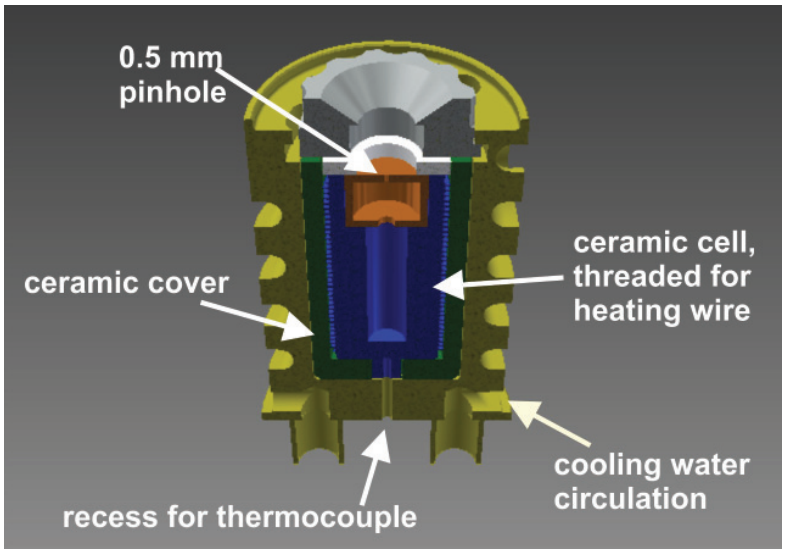

Figure 3.2: The oven cross section. Figure taken from Ref. [53]

thickness of 2.1 mm. A water-cooled stainless steel vessel (yellow) keeps the outer wall of the oven to the room temperature while the inside is hot. This cooled outer wall was planned to serve as an absorber for the heated residual C_{60} in order to keep its contribution to the base pressure low. Finally, a Macor plate (white) is fixed by a stainless steel cover (silver) with a stainless steel string (not shown in Fig. 3.2). However, if the temperature difference between the sublimated molecules and the oven orifice is too large a molecular cloud can be created right above the orifice. This leads signal decrease by scattering.

In addition, we find that the thermo-element in the recess on the bottom side of the oven gives a lower temperature than that the molecules actually have. In a Comsol simulation, Fig. 3.3, the heat distribution of a simplified oven model yields a temperature difference of approximately 50-100°C due to the water cooling which would change the vapour pressure by a factor of 2 to 5 [51].

In the simulation (Fig. 3.3) the heating wires are replaced by a homogeneously heated cladding at 1000 K because of the time consuming Mesh-calculation. We use a cylindrical tube without any fine structure to approximate the stainless steel cover and also the spring is neglected because of the small contact surface with the Macor plate. A large temperature gradient arises when the water cooling is switched on as shown in Fig. 3.3(b) and (c).

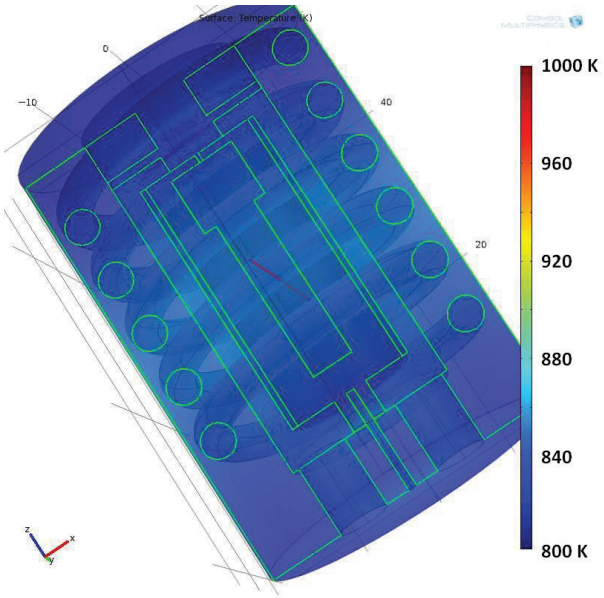

(a)

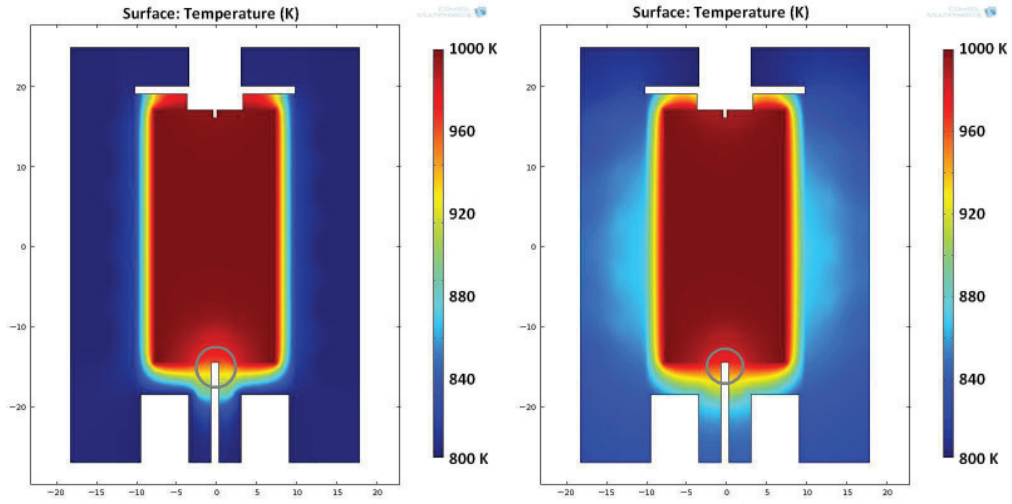

(b) (c)

Figure 3.3: Comsol simulation for the heat distribution for a simplified oven structure illustrated by the green lines in (a). The temperature distributions with (b) and without (c) water cooling are visible. At top of the recess (gray circles in (b) and (c)) where the thermo-element is positioned, a difference in temperature can be clearly seen.

3.1.3 Velocity distribution

The velocity distribution of the sublimated molecules can be described by the Maxwell-Boltzmann distribution

$$f_{\mathrm{MB}}(v) = \sqrt{\frac{2}{\pi}} \left(\frac{m}{k_B T}\right)^{3/2} v^2 \exp(-mv^2/2k_B T) \tag{3.1}$$

where m is the mass of the molecules, v is the velocity of the molecules, T is the oven temperature and k_B is the Boltzmann constant. The most probable and the mean velocities are given by $v_p = \sqrt{\frac{2k_B T}{m}}$ and $v_0 = \sqrt{\frac{8k_B T}{\pi m}}$, respectively.
However, due to the channelling effect of the thick orifice wall, we find that a Gaussian $g(v)$ describes the velocity distribution better than the Maxwell-Boltzmann distribution [55],

$$g(v) = A \cdot \exp\left(-\frac{(v - v_0)^2}{2\sigma_v^2}\right) \tag{3.2}$$

where the amplitude A, the mean velocity v_0 and the velocity spread σ_v are the fitting parameters. Since the time-of-flight technique only determines the molecular arrival time distribution we transform Eq. 3.2 from velocity to time domain using

$$g\left(v(t)\right) dv(t) = -\frac{L}{t^2} g(t) dt \tag{3.3}$$

with the Jacobian $dv = -\frac{L}{t^2} dt$. The red dashed lines in Fig. 3.4(b) indicate the velocity distribution fits with $v_0 = 174$ m/s and $\sigma_v = 40$ m/s which are employed in the velocity domain and time domain, respectively. The data in Fig. 3.4(b) is the summation of the periodic, raw time-of-flight data in Fig. 3.4(a). The duration between the individual peaks is defined by the rotation frequency of the chopper which will be described in the next section.

3.1.4 Chopper

Since the de Broglie wavelength depends on the molecular velocity, a narrow velocity band should be selected to see matter-wave interference. In the earlier setup of the TLI, a helical velocity selector was used. Due to a high level of vibration caused by the driving motor it is replaced by a rotating chopper. The velocity

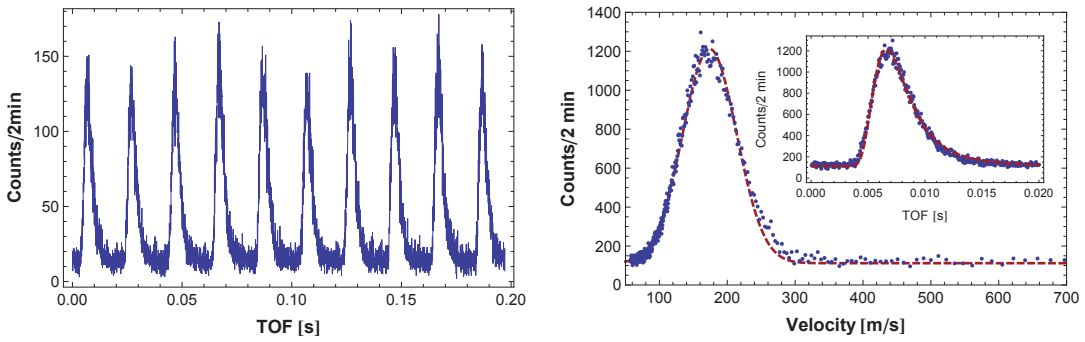

(a) Raw data of 10 time-of-flight peaks

(b) Summed time-of-flight data with the fits.

Figure 3.4: In (a) the raw time-of-flight data are plotted against time-of-flight where the individual time-of-flight curves are visible. Due to the periodicity of the data in (a) we sum up the data of the individual time-of-flight peaks to multiply the signal intensity and employed velocity fits in velocity domain (main plot in (b)) and the time domain (inset in (b)), respectively.

resolved interference visibility shall be recorded using a time-of-flight technique[7]. In this case the time resolution (the dwell time t_{dwell}) of the electronic detecting device defines the precision of the velocity selection.

The chopper disk was manufactured at the University of Southampton. It has 10 equally spaced slits of 1 mm width on a disk with a radius of 24 mm which is driven by a motor (MAXON EC32). The rotation speed is read out by an ultra-high vacuum compatible encoder module (GSI MicroE Systems, Mercury 1500V) and controlled by a servo amplifier module (Maxon, DES 50/5). An optical sensor is placed on top of the motor to provide the trigger signal for the time-of-flight measurement.

The rotating chopper separates the continuous molecular beam into pulses which are detected by a fast digitizer card (FastComtec, MCA-3 P7882) as seen in Fig. 3.4(a). Since the trigger signal does not coincide with the opening edge of the slit, the delay in data acquisition needs to be corrected. This issue is illustrated in Fig. 3.5. We set the chopper rotation frequency to 5 Hz which defines the period between the slits $t_{\mathrm{period}} = 0.02$ s. From this we obtain the opening duration

[7]Details of theoretical prediction of the measurement are in section 4.1

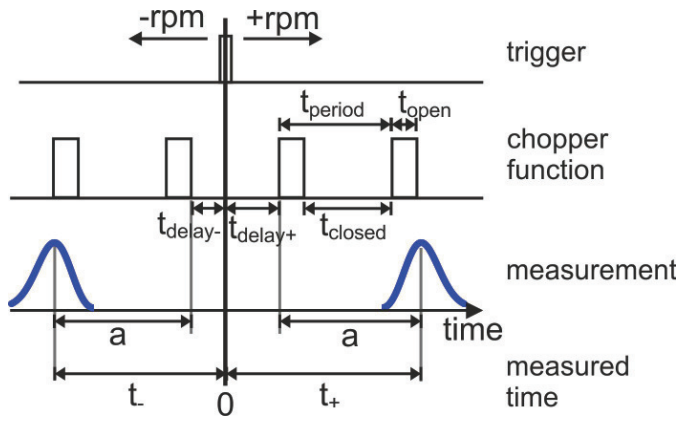

Figure 3.5: The offset of the trigger signal: The maximal signal will be detected at time a after the opening edge of the slit. By measuring t_-, t_+ and t_{close} the offsets $t_{\text{delay}-}$ and $t_{\text{delay}+}$ can be well measured. Figure taken from Ref. [53].

$t_{\text{open}} = 1.3$ ms and the closed duration $t_{\text{closed}} = 18.67$ ms. By running the chopper in both directions the times for acquiring the peak of the first time-of-flight curve are given by $t_+ = 13.6$ ms and $t_- = 17$ ms. After applying

$$t_+ + t_- - t_{\text{closed}} = 2a \tag{3.4}$$

the offsets are estimated to be $d_{\text{delay}+} = 7.64$ ms[8] and $d_{\text{delay}-} = 11.04$ ms for $a = 5.86$ ms.

3.2 Interferometer chamber

As pictured in Fig. 3.1, the interferometer is encased in a cylindrical vacuum chamber with a diameter of 35.6 cm and a height of 73 cm. A tube with a diameter of 15 cm and a height of 50 cm holds the QMS. The entire vacuum complex is pumped by a two stage pumping system with the Edwards Two Stage 40 as the pre-pump and a Pfeiffer HiPace700 turbo pump. The lowest pressure reached in operation is$9 \cdot 10^{-8}$mbar.
The base of the Talbot-Lau interferometer is built upon a support ring which holds the entire interferometer assembly, as seen in Fig. 3.6. A support x-y alignment

[8] A electronic delay time of $50\mu s$ needs to be taken into account in addition.

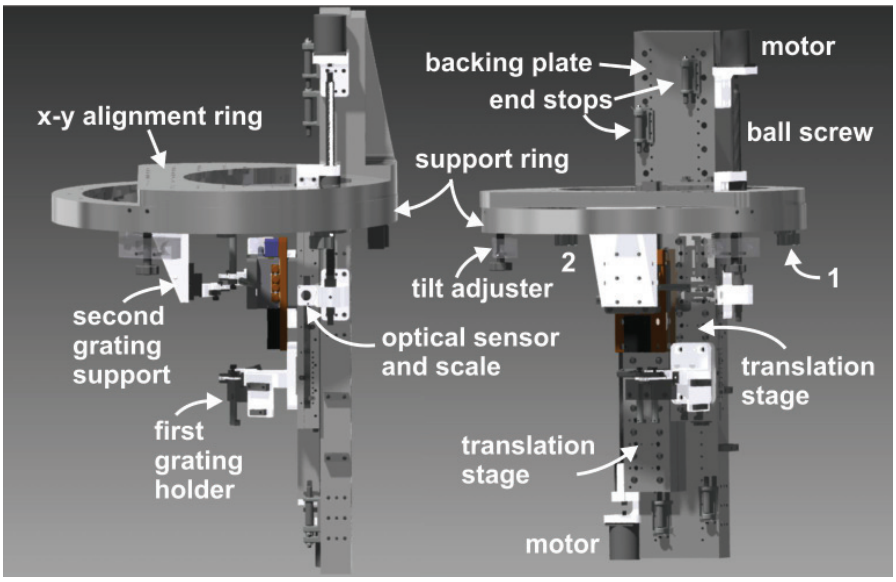

Figure 3.6: Interferometer assembly: the interferometer is based on an alignment ring with a backing plate equipped with two translation stages for the first grating and the third gratings. The support stage for the second grating is separately fixed to the alignment ring. Figure taken from Ref. [53].

ring enables tilting of the interferometer with respect to the rest of the setup by two tilt adjusters. A separated support stage for the second grating and an additional backing plate are also attached to the alignment ring and the backing plate works as the gliding plate for vertically moving translation stages[9] for the first and the third gratings.
Two slits are placed in front and one additional slit is placed behind the interferometer. The slits width can vary between 2 mm, 1 mm, 0.5 mm, 0.2 mm and 0.1 mm. A measure of the molecular beam profile for these openings can be found in section 3.3.2. Finally, the QMS is located on top of the chamber.

3.2.1 Gratings and grating holders

The TLI consists of three identical material gratings. All gratings were provided by Markus Arndt (University of Vienna) and manufactured by Tim Savas at MIT.

[9]Driven UHV compatible stepper motors (VSS32, Pytron-Elektronik GmbH) with optical sensor (MicroE systems, Mercury 1000) as readout

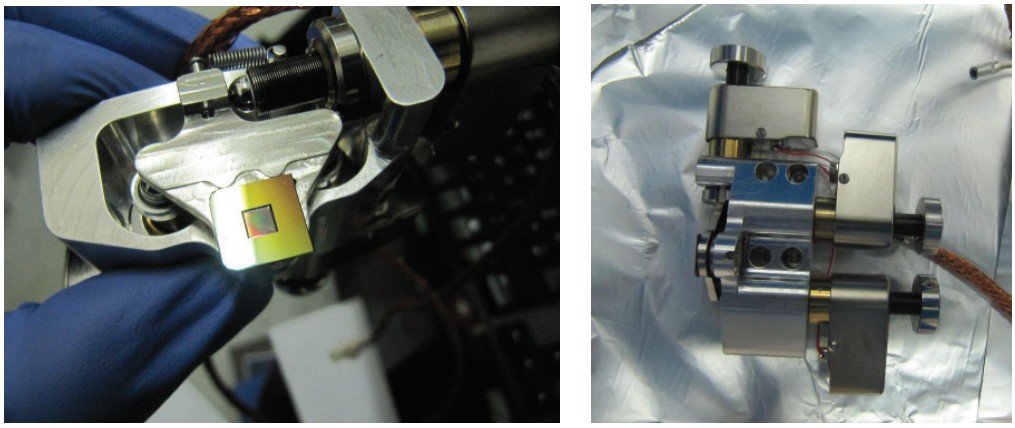

(a) (b)

Figure 3.7: Grating and grating holder: the grating membrane is clearly visible in the front view (a). Three pico motors (b) are attached to the grating holders for grating alignment.

They were fabricated on a silicon wafer using interference lithography followed dry and wet etching [52]. As seen in Fig. 3.7(a) the Si wafer is then cut into single 1×1 cm^2 silicon chips with a membrane of a size of 5×5 mm^2 and a thickness of 190 nm placed in the middle. The actual gratings on these membranes have a period of 257 nm with a supporting structure of period of 1.5 μm. The first and the third gratings are individually mounted on holders whose orientations (pitch/yaw/roll, see section 3.3.2) are adjustable[10] via three Ultra-High Vacuum Picomotors[11] controlled by a New Focus picomotor controller (model 8752). Each grating holder is attached to one of the translation stages, separately. An additional motorized translation stage drives the third grating horizontally for the interference scan (described in section 3.2.3). The grating holder for the second grating has only two manual knobs for Pitch/Yaw control (as seen in Fig. 3.8) and is therefore only used as reference point for the grating alignment since it can not be adjusted in vacuum.

[10] In the previous setup the grating orientation is adjusted by piezo elements which are replaced because of the huge time consumption.

[11] These motors are driven by electrical pulses in kHz repetition rate. However, a precise control of the step size between 10 and 20 nm is not possible.

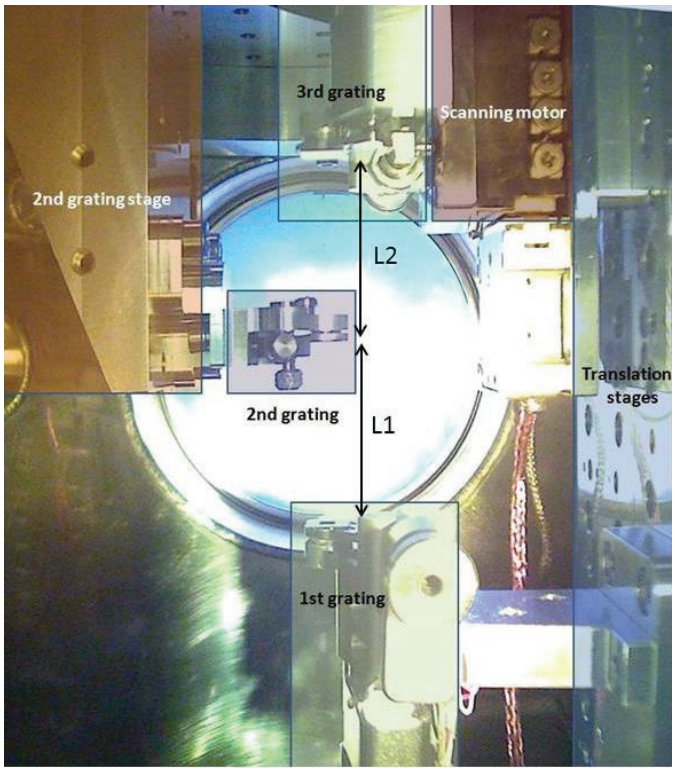

Figure 3.8: A side view of the interferometer. The molecular beam propagates from the bottom (the first grating) to the top (the third grating). The grating distance L2 varies while L1 is fixed at 39 mm.

3.2.2 Translation stages

Two translation stages are necessary in order to correct the distance between the gratings since an accuracy of 6 μm (see section 3.3.2) is necessary. For different molecules and velocity classes we would have to reposition the gratings corresponding to the Talbot length. Therefore, it is beneficial to gain control over the grating distance without venting the chamber.
The translation stages for the first and the third gratings (denoted by **S1** and **S3**, respectively) are positioned vertically along the molecular beam with the middle grating fixed in position. A LabView programme controls the stages. For the calibration of the step size of the translation stage motors we measured the distance between the central grating and the outer gratings at different motor positions.

This was done within three independent series of measurements[12] where the error of measuring the stage position is given by the standard deviation calculated from the measurement series, as shown in Fig. 3.9. We extract the motor step size

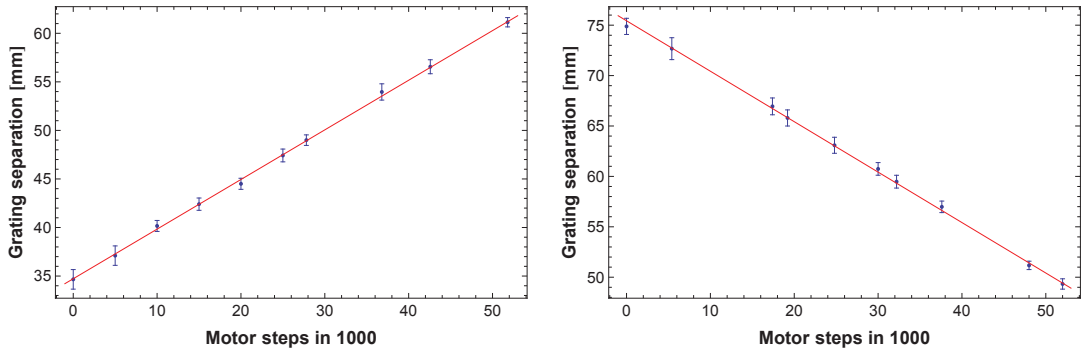

(a) S1 calibration

(b) S3 calibration

Figure 3.9: (a) and (b) show the linear fits of the three independent calibration measurements.

from the linear fits (red lines) which is 500 ± 14 nm. The positioning error of the translation stages[13] is 350 μm, calculated from the mean error of each data point in Fig. 3.9 (a) and (b). The stability is measured to be better than 2 motor steps within 8 hours.

3.2.3 Scanning motor

The scanning motor is connected to a linear stage[14] with a 20 mm travel range and a step size of 2.5 nm. The position readout is provided by the commercial software (Nanomotion FlexDC controller program). The motor is responsible for scanning the third grating across the interference fringe. In order to resolve the 257 nm sinusoidal interference pattern the motor step size needs to be small enough.

[12]The grating separations at given motor positions are measured by three experimentalists independently.

[13]The distances from the starting positions of the S1 and S3 to the second grating are estimated to be 34.7 mm and 75.4 mm, respectively.

[14]Type: FB05 with FLEX DC encoder purchased from Nanomotion Ltd. It performs digital position and velocity control using incremental encoder devices.

According to the product specification, the position repeatability has an uncertainty of ±50 nm. We found that it fails to make step sizes below 50 nm. This makes interference scan impossible. To overcome this problem, we could use the periodicity of the grating by sending the scanning stage to the same point in the next period, i.e. the step size between two scanning points is increased by 257 nm in advance.
However, this concept can not be directly applied to our experiment due to the instability of the scanning motor. The scanning motor was characterized with and without the feedback loop (SERVO) as extensively described in appendix B. We use the following method to compensate this instability.
During the interference fringe visibility measurement 4.2 we sent the scanning stage subsequently to 10 transversely following motor positions which were separated by two grating periods and 23 nm[15]. After this scan the stability of the scanning stage at each transverse scanning position needs to be checked in the data analysis. These positions will also be error-corrected and projected into one grating period by using modulo operation[16] for interference fringe visibility fits. This method has only the disadvantage that projected positions within a single grating period is random, as mentioned in appendix B. We repeated this procedure during the interference search within the positioning uncertainty of G3, as described in section 4.2.

3.2.4 Detection

A quadrupole mass spectrometer (QMS)[17] is used to detect molecules upto 9000 u. It is located 60 cm after the third grating mask to collect the transmitted molecular beam. The housing is mounted on three adjustable legs which enable positioning of the entrance hole at any position across the molecular beam. In general, a QMS consists of three parts, an ionizer, a mass selector and an ion collector.
Here, we use electron impact ionization. The electrons are generated by thermionic emission of heating four tungsten wires placed in a square around the molecular

[15]This value depends on the number of scanning positions within one grating period.
[16]For example, the error-corrected position is at 547 nm which corresponds the position 33 nm (547 mod 257).
[17]Extrel, CMS 9000

beam path. An electro-static field[18] is applied between the filaments and the ion region to extract and accelerate the electrons to 70 eV to ionize the molecules. The ionization efficiency varies between 10^{-4} and 10^{-6} [46] depending on the type of the molecules. By adjusting the voltage applied between the ion region and the quadrupole, the pole bias, the resolution of quadrupole mass filter can be tuned. The theory of quadrupole mass filters is described in Ref. [47] and is therefore omitted here. The basic idea is to build a quadrupole electric field within the quadrupole. Molecules with unstable trajectories will be ejected by the electric field. The transmitted positive charged molecules are mass selected and will be drawn to the negatively charged dynode. At impact upon the dynode, secondary electrons are emitted and multiplied by a channeltron. The resulting electric signal is then amplified by an amplifier whose delimiter level is adjustable to lower the dark counts. In the end, the signal is collected by a computer.
For a high detection efficiency, a multi-parametric alignment procedure is necessary. All tunable parameters regarding ionization, ion focusing, mass selection and ion detection need to be adjusted. A list of optimized parameters is given in the appendix A.

3.3 Alignment

In this section, the alignment requirements for TLI will be shortly listed, followed by a step-by-step description of the alignment procedure.

3.3.1 Alignment requirement

In the table 3.1 we summarize the required and achieved precision of the most important parameters which will be introduced below.
Firstly, one needs to ensure that the **transverse coherence** Δr_{coh} of the molecular beam covers at least two slit openings of the second grating at the first order of the Talbot length. This can be justified by the van Cittert-Zernike theorem (see section 2.4).

[18]The voltage should be low enough to prevent multiple ionization which results in signal reduction.

As the TLI relies on self-image detection at the Talbot distances, these self-images disappear and change if the grating distance deviates from any integer multiple of the Talbot length. Hence we require [48]

$$\frac{\Delta L}{L} < \frac{1}{N} \tag{3.5}$$

where L is the distance between the gratings, N is the number of illuminated slits and ΔL is the imbalance. For a 2.2 mm wide beam with 6200 illuminated slits interference contrast can be maximized if the precision of the grating distance $\Delta L < 3\mu$m is achieved. This corresponds to $\Delta L/L \approx 0.02\%$ for one Talbot length of 1.9 cm. By choosing the second Talbot order the precision is lowered to 6 μm in the current setup. Further relaxation of the precision of the grating distance to 14 μm is possible if the smallest collimation slit is used which prepares a molecular beam with a waist of 0.7 mm (FWHM), as seen in section 3.3.2. However, this relaxation of the precision is at the expense of beam intensity. Due to the weak signal, measurements are in general conducted without any collimation slits.
Tilting the grating forward or backward (**pitch**) would locally change the grating distance, as shown in Fig. 3.10. Assuming a rotational axis at the centre of the grating, we find the precision of the pitch angle alignment needs to be $\alpha_{\text{pitch}} < 2$ mrad (estimated by using $\alpha_{\text{pitch}} <$arctan(ΔL/w) where w is the half beam waist) for a 2.2 mm wide molecular beam.
Similar considerations can be applied for **yaw**, as shown in Fig. 3.10. Additionally, yaw leads to a reduction of the grating period d and of the slit opening a. The effective period given by $d_{\text{eff}} = d \cdot \cos(\beta_{\text{yaw}})$ restricts the yaw angle β_{yaw} to less than 13 mrad. A relative error of 10% of the slit width was shown to affect the interference contrast in a numerical simulation [61]. Therefore, we define the relative slit opening change to be $\Delta a/a < 1/10$ with $\Delta a = a - a_{\text{eff}}$ whereas

$$\Delta a = a/\sin(\beta_{\text{yaw}}) - 2b \cdot \cos(\beta_{\text{yaw}}) \tag{3.6}$$

with the grating thickness $b = 190$ nm. This yields that the yaw angle β_{yaw} needs to be smaller than 28 mrad regarding the width of slit openings.
Gratings can also **roll** around their axes with respect to each other, as seen in Fig.

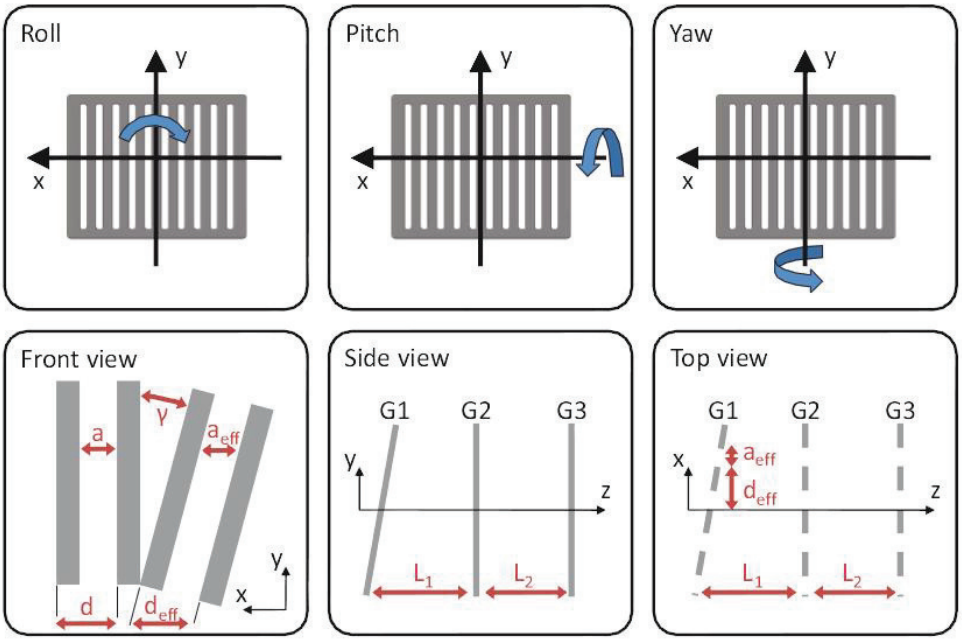

Figure 3.10: Roll, pitch and yaw movement and their effects on the grating period and slit opening. Figure taken from Ref. [61].

3.10. This results in a change of the effective grating period to

$$d_{\text{eff}} = d/\cos(\gamma_{\text{roll}}) \tag{3.7}$$

where γ_{roll} is the roll angle. We define the maximal aberration of the period $\Delta d = d_{\text{eff}} - d$ as such when the first illuminated slits of two gratings fully overlap and the last illuminated slits are shifted by half of grating period, $d/2$. For a 1.6 mm wide beam with 6200 illuminated slits the period should be defined to better than $\Delta d/d < 8 \cdot 10^{-5}$. This corresponds to a maximal roll angle of $\gamma_{\text{roll}} < 13$ mrad. In summary, the alignment requirements and achieved precisions before interference scan are listed in Tab. 3.1[19].

[19]The calculations for the achieved precision are given in section 3.3.2.

Parameter	Required precision	Achieved precision
grating distance	6 μm	350 μm
pitch angle	2 mrad	120 μrad
roll angle	13 mrad	3 mrad
yaw angle	6 mrad (long. distance)	120 μrad
	13 mrad (period)	120 μrad
	28 mrad (slit opening)	120 μrad

Table 3.1: Required and achieved alignment precisions of longitudinal grating distance, pitch, roll and yaw alignment for a 2.2 mm wide molecular beam.

3.3.2 Alignment procedure

The idea is to first optimize the molecular beam. Then, an alignment laser is aligned with the molecular beam. Finally the gratings are inserted using the alignment laser as reference. A fine adjustment of the individual components is based on the data analysis.
Our goal is to optimize the signal intensity by moving position of the oven and the QMS. G1 and G2 are initially removed from the chamber and G3 should be positioned so that the molecular beam is not blocked.

1. Oven and interferometer chambers need to be pumped.

2. The oven position and the QMS position are optimized by the 'walking' technique without any collimation slits in the beam.

3. The chopper frequency[20] and the QMS tune file are optimized.

The molecular beam widths are measured for different slit sizes (1 mm, 0.5 mm, 0.3 mm, 0.2 mm and 0.1 mm) of the first collimation aperture. In order to measure the beam profile, the transmitted signal through the third collimation aperture was measured as it moves across the beam at a distance of 0.5 m away from the first collimation aperture. Due to the finite width ($\approx$ 1 mm) of the third collimation slit, the measured molecular beam shape can be seen as a convolution between the third collimation slit and the true beam intensity distribution. This average over

[20]The chopper frequency needs to be kept low enough so that the time-of-flight peaks do not overlap, as described in section 4.1.

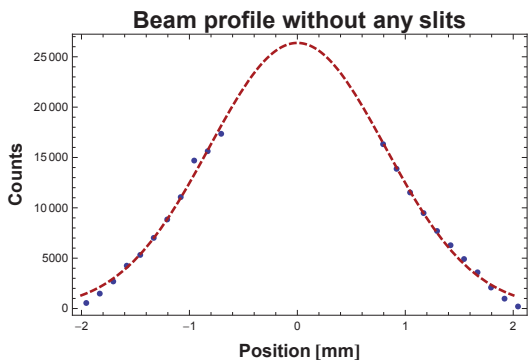

(a) Unperturbed beam with a FWHM of 1.6 mm

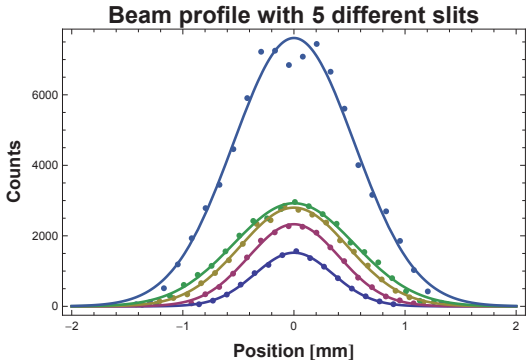

(b) Beam widths (FWHM) with 5 different slits: 1.1 mm for the 1 mm slit(blue), 1 mm for the 0.5 mm slit (green), 0.98 mm for the 0.3 mm slit (yellow), 0.8 mm for the 0.2 mm slit (purple) and 0.7 mm for the 0.1 mm slit (dark blue).

Figure 3.11: Molecular beam profile measurement

the slit changes the beam shape. We find that a Gaussian approximates the beam profile very well, as shown in Fig. 3.11(b) for each individual slit size. We use the full width at half maximum to determine the molecular size.

4. To measure the exact path of the molecular beam, we use all three movable collimation slits to define the molecular beam. The two end positions of the translation stage S3 define two additional positions in the molecular beam using the third grating as a pinhole.

In total, we obtain 7 positions inside the whole setup which define the molecular beam. These are the skimmer, the first two collimation apertures, two positions defined by S3, the third collimation aperture and the entrance hole of the QMS.

5. An alignment laser (445 nm Diode laser) is setup on the optical bench. The optical setup is sketched in Fig. 3.12. The laser is sent through the entire chamber and aligned with the 7 reference points to simulate the molecular beam path. A beam diameter of less than 2 mm was achieved at 3 meters away from the laser head.

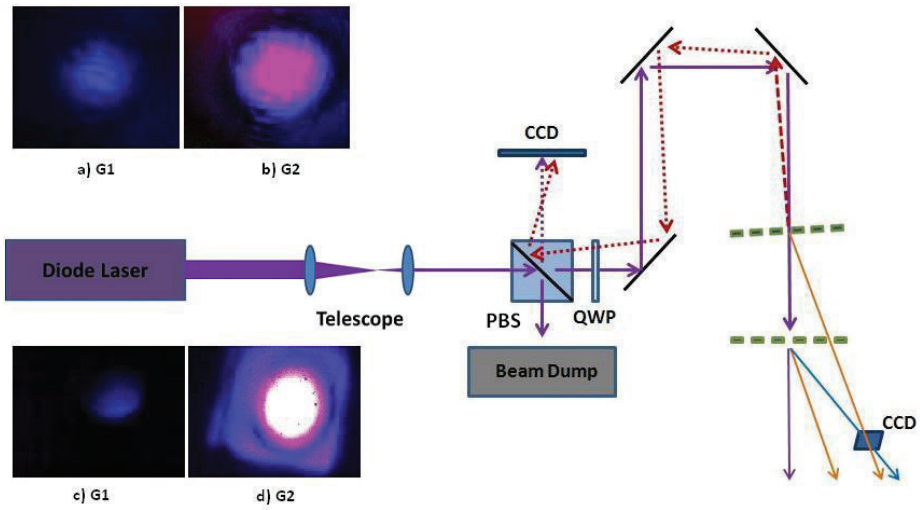

Figure 3.12: The laser alignment setup: a telescope is used to narrow the beam waist for a better alignment precision. A polarization beam splitter (PBS) and a quarter wave plate (QWP) are used to deflect the retro-reflected light (dotted) into the CCD chip. Two pictures of the back reflections from the first and second gratings are shown in a) and b), respectively. Two additional CCD chips are built into the chamber for the grating alignment using different diffraction orders from the supporting structure of the gratings. Overlapping the first (orange) and the second (blue) diffraction order of the gratings enable us an roll alignment with an uncertainty below 3 mrad, as seen in c) and d) for the first and the second gratings, respectively.

The alignment of the gratings is most critical to the experiment. Pitch and yaw were carried out by monitoring the laser beam retro-reflected from the grating surface. These retro-reflections return to the optical bench and are picked up by a quarter wave plate (QWP) and a polarization beam splitter (PBS) from the seed beam. A 5×4 mm^2 CCD camera chip with a resolution of 1600×1200 MP is located at a distance of 2.4 m away from the interferometer to monitor the reflection overlaps. An uncertainty of 90 pixels, corresponding to 280 μm is measurable. Therefore, an accuracy of 0.12 mrad can be easily achieved for pitch and yaw alignments. By overlapping different diffraction orders from the supporting structure of two gratings the roll angle is aligned, as seen in Fig. 3.12. An accuracy of 3 mrad could be achieved by comparing the images taken by the CCD camera.
Once the grating orientations are optimized, the distance between the gratings

needs to be set. The appearance of interference fringes is the indicator of good alignment. Since the uncertainty in S3 positioning tremendously exceeds the alignment requirement, we need to look for interference patterns for each longitudinal grating distance within this uncertainty. For this reason, a systematic scan with a fine step size is implemented using LabView, see section 4.2.
Further procedure for interference contrast optimization is to realign the orientation of each grating according to the change of measured visibility. By repeating this process the interference fringe contrast can be increased, once it is found.

Chapter 4

Interference measurements

In this chapter, we introduce the idea of the interference measurement before we present some data showing possible interference patterns.
In the existing publications [39, 40], a velocity distribution of 10%-20% is prepared to obtain high-interference contrast. Here, we aim for an observation of molecular interference fringes without any velocity selectors, neither gravitational slits nor a rotational rotor. Time-of-flight technique can directly select the velocity class and has the advantage of higher resolution than the common velocity selectors, and is only limited by the dwell time t_{dwell} of the time-of-flight-card. Also the vibrational noise produced during the time-of-flight measurement comes from the motor of a thin chopper plate which is lower than the vibration caused by rotating rotors used in the earlier setup.
One major disadvantage of using time-of-flight technique is the averaging of the velocity distribution over the opening time of the chopper slit. The chopper rotation frequency is set to 5 Hz. This needs to be low enough so that time-of-flight signal peaks are smaller than the separation between adjacent peaks.

4.1 Concept

The velocity distribution of the molecular beam is better approximated by a Gaussian distribution $g(v)$ than by a Maxwell Boltzmann distribution because of nozzle and thin wall effects. In order to estimate the averaging effect within the open-

ing time of each chopper slit let us first determine the transmission through the chopper as the 1 mm slit moves across the molecular beam. Here we assume that the spatial intensity variation of the molecular beam within a radius of 0.5 mm around its axis is negligible at a distance of 20 cm away from the nozzle. Since the skimmer has a diameter of 1 mm it defines the dimension of the molecular beam that enters the interferometer chamber. Hence we only need to observe the effect of the chopper slit on the modified molecular beam.
We define the transmission function $T(x)$ as the convolution between the molecular beam cross section, approximated by $f_{\text{beam}}(x)$ as a circle with 0.5 mm radius and the chopper function $f_{\text{chopper}}(x)$, given by a rectangular function. Therefore, we have

$$T(x) = f_{\text{beam}}(x) \star f_{\text{chopper}}(x) = \int_{-\infty}^{\infty} d\xi f_{\text{beam}}(\xi) f_{\text{chopper}}(\xi - x) d\xi \qquad (4.1)$$

where x is position of the chopper. By normalizing $T(x)$ we receive the relative transmitted signal through the slit with a value between 0 and 1. A numerical conversion of $T(x)$ to time is plotted in the inset of Fig. 4.1. At all positions $T(t) \neq 0$, the molecules have a Gaussian velocity distribution with a shift in time defined by the transmission function $T(t)$. The total signal $S_{\text{aver}}(t)$ is an integration of the velocity distribution over the total opening time whereas the variation of the maximal intensity of the individual velocity distribution is determined by $T(t)$, as shown in Fig. 4.1. We obtain

$$S_{\text{aver}}(t) = \int_{-\infty}^{\infty} d\tau T(\tau) g(t - \tau) d\tau \qquad (4.2)$$

where $g(t) = N_0 \exp\left(-(\frac{L}{t} - v_0)^2 / 2\sigma_v^2\right)$ is the Gaussian velocity distribution converted into time-of-flight, L is the length between the chopper and the detection, v_0 is the mean velocity and σ_v is the width of the velocity distribution.
Now let us analyse the situation with interference. The interference fringes are expected only for certain velocities close to the Talbot condition. The inset of Fig. 4.2(a) shows the dependence of the simulated[48][1] interference fringe visibility on

[1]The programme was written by S. Nimmrichter. The parameters for the simulation were customized for our setup.

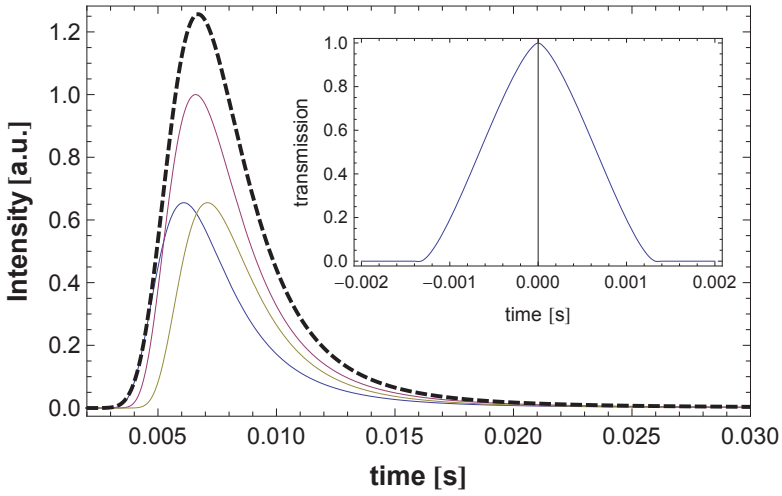

Figure 4.1: The transmission function converted into time is plotted in the inset plot as a 1 mm chopper slit passes across the 1 mm wide molecular beam with a uniformly distributed circular shaped beam profile. The averaging effect is shown in the main plot in arbitrary units where the transmission function is taken into account. The dashed black line is the averaged time-of-flight curve from the converted $g(t)$ at different times (Purple: $t = 0$, blue: $t = -0.5$ ms and yellow: $t = 0.5$ ms).

the velocity of C_{60} and the Gaussian velocity distribution in arbitrary units in order to compare the relative contribution of the visibility peaks.

Without taking the averaging effect into account, we expect the main plot of the Fig. 4.2(a) described by

$$S_{\pm}(t) = g(t)(1 \pm \mathrm{Vis}(t)) \tag{4.3}$$

where $\mathrm{Vis}(t)$ is an interpolated function describing the interference visibility in the inset of Fig. 4.2(a). The red ($+$ in Eq. 4.3) and blue ($-$ in Eq. 4.3) dashed curves indicate the expected signal for the perfect alignment when the scanning grating is positioned at the maximal and minimal transmissions, respectively. For any other scanning grating positions the interference peaks lie within the shadowed area limited by the dashed lines.

The averaged signal can be estimated by

$$S_{\pm}(t) = \int_{-\infty}^{\infty} d\tau g(t-\tau)T(\tau)(1 \pm \mathrm{Vis}(t-\tau)). \tag{4.4}$$

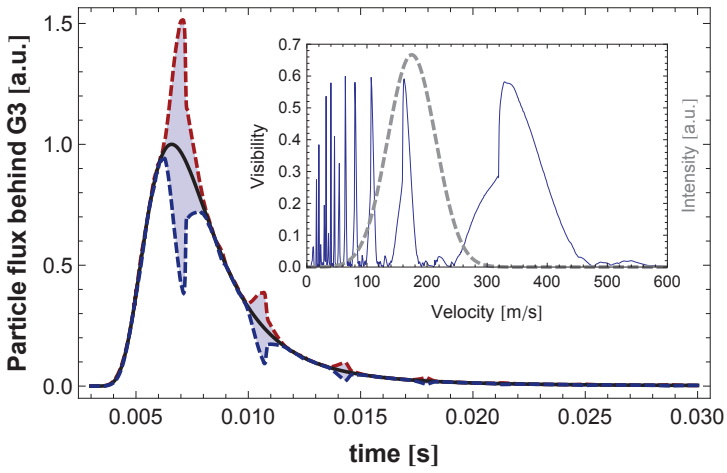

(a) Expected time-of-flight signal behind G3 with infinitely narrow chopper slits

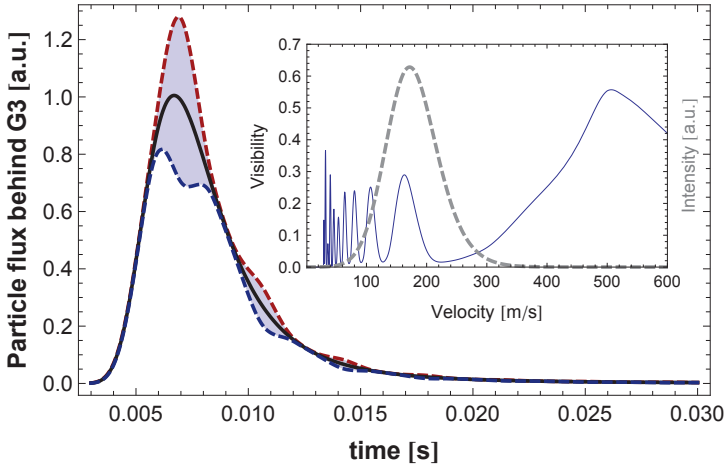

(b) Expected time-of-flight signal behind G3 with 1 mm wide chopper slits at a rotation frequency of 5 Hz

Figure 4.2: For an infinitely narrow chopper slit the averaging of the velocity distribution over opening time of the slit can be ignored. The solid black line indicates the time-of-flight curve without matter-wave interference. The red and blue (dashed) lines describe the expected maximal and minimal signal, respectively in the presence of interference. Taken van der Waals forces into account, the visibility of C_{60} in a TLI is plotted in the inset of (a).
The Gaussian velocity distribution is given in the inset as dashed gray line. If the averaging effect is taken into account, a clear decrease and broadening of the visibility peaks is to be expected in (b).

The integral broadens the visibility peaks and reduces the maximum visibility by almost 50% as shown in Fig. 4.2(b)[2].
A specific velocity selection can be achieved by setting the dwell time t_{dwell} of the time-of-flight-card. An increasing dwell time corresponds to an increasing relative velocity spread $\Delta v/v$ and influences the visibility according to Eq. 4.4. Fig. 4.3 shows this around $v = 164\mathrm{m/s}$, where we expect a strong signal. From this we con-

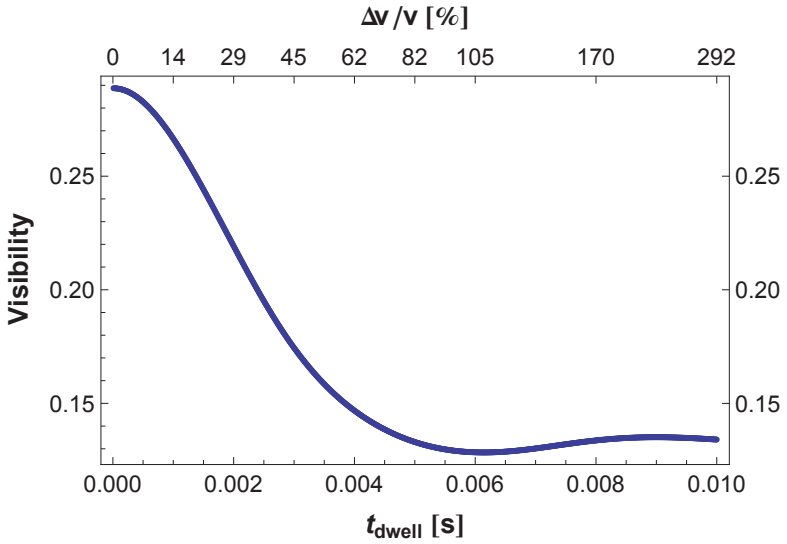

Figure 4.3: The influence of the dwell time on the visibility around 164 m/s is given by the blue line. A decrease of visibility is negligible for $t_{\mathrm{dwell}} < 500\mu$s corresponding to 7% velocity spread.

clude that reducing t_{dwell} below 500μs would not affect the visibility considerably, under the assumption of perfect grating alignment. In reality, any misalignment will lead to a further visibility reduction. For low visibilities, experimental noise can completely hide the interference peaks in the time-of-flight curves. Therefore, a stable signal with a high signal-to-noise ratio is important when searching interference.

[2]The data in the inset is reconstructed from the calculated data in the main plot.

4.2 Data collection and analysis

The interferometer is first set for C_{60} at the most probable velocity of 165 m/s with a Talbot length of 1.95 cm. I choose the grating separation to be twice the Talbot length to enable interference at higher velocities and to increase the transverse coherence at the second grating, see section 2.4.
Due to the large uncertainty in the longitudinal grating distance the grating separations need to be matched by varying G3 position while G1 and G2 are fixed. Once the grating distance between G2 and G3 is close to the distance between G1 and G2, interference fringes can be observed. Therefore, we need to do visibility measurement at each grating position. The method for visibility measurement is described in section 3.2.3.
A LabView program automates the interference search by initially changing the grating distance in steps of 100 μm. At each S3 position the program controls G3 to do a visibility measurement where the scanning stage is powered off for two minutes for signal acquisition at each transverse scanning position of G3.
This procedure has the disadvantage that at each visibility measurement the scanning stage needs to return to its original starting position which is more than 2570 nm apart from its last position. Moving the scanning motor by such step size causes a large drift of the motor position as described in appendix B. Therefore, a large number of data can not be used in the data analysis due to the shift. A better measurement scheme is explained in section 4.3.

Since each data acquisition lasts 120 s the drift of the scanning stage needs to be minimized. This however cannot be manual controlled. Therefore, only data sets with a drift of less than 20 nm are used for the analysis. A Mathematica notebook is written to process the data of interference scans that were recorded over 150 hours of measurement time.

Fig. 4.4 is a numerical simulation of the interference visibility as a function of time-of-flight and grating position within one grating period, according to Eq. 4.4. Density plots provide a clear visualisation of the intensity distribution in case of interference. Brighter colors represent more intense signals. From this, any periodic intensity variation around 0.007 s would indicate quantum interference.

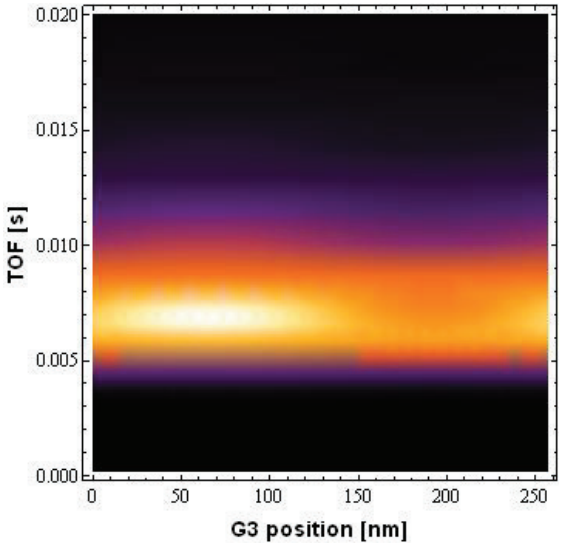

Figure 4.4: Simulated result with maximal visibility

For the data set of each visibility measurement the transverse scanning position of G3 was error-corrected using the method described in section 3.2.3. Fig. 4.5 (a) shows a raw data set without any interference at all due to the random intensity distribution. We interpolate[3] these raw data to make the interference contrast

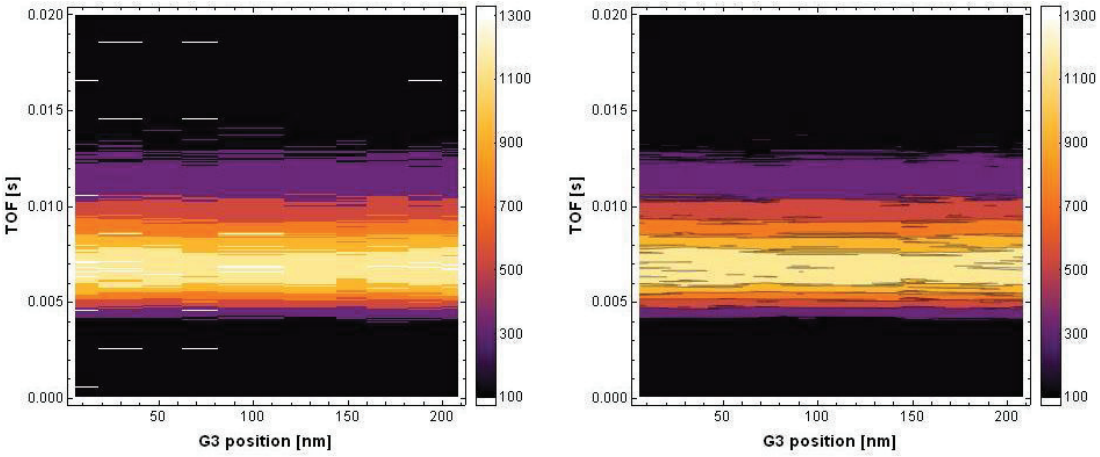

(a) Raw data without any interference

(b) Interpolated data with any interference

Figure 4.5: Data without interference

more visible, as shown in Fig. 4.5 (b). No similarity appears in comparison with Fig. 4.4.

However, there are two S3 positions[4] that show an interesting pattern in Fig. 4.6 and Fig. 4.7, respectively. Also here, I interpolated the raw data for a better visualisation. The intensity variations around 0.007 s have a period close to the grating period. This motivates us to study further. Fig. 4.8 displays 3D maps

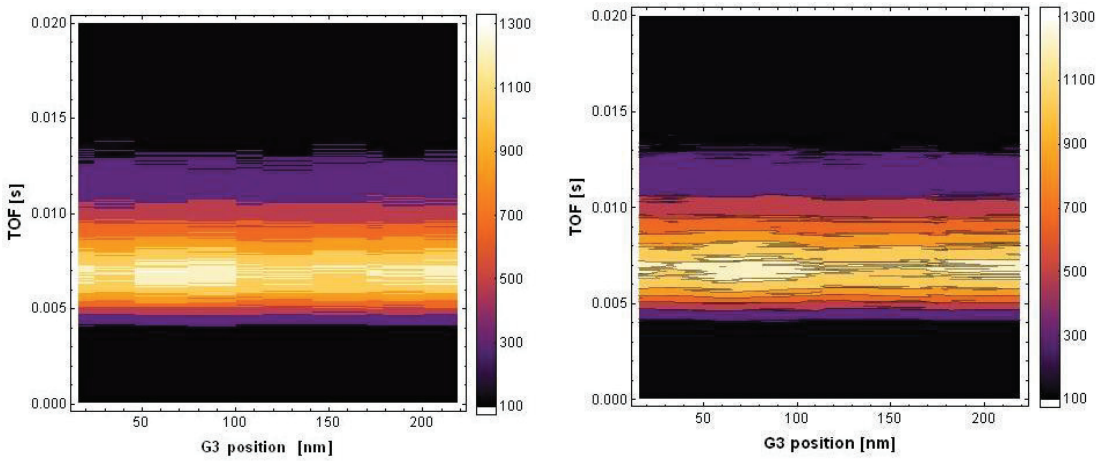

(a) Raw data

(b) Interpolated data

Figure 4.6: Dataset at S3 position: 378300

of the data. The same intensity variation appears at the peaks of the time-of-flight curves. I applied sinusoidal visibility fits to the data in Fig. 4.6 and Fig. 4.7 as shown in Fig. 4.9 where the errors of the grating positions come from the drift of the scanning stage during the 120 s measurement which are indicated by the horizontal error bars. The signal fluctuation could not be determined[5] since several measurements at the same positions are required. Maximum interference visibilities of 7% and 9% are determined around the expected velocity of 162 m/s with a velocity spread of 2%[6], respectively. However, the interference patterns

[3]We use the interpolation function of Mathematica which fits polynomial curves between successive data points.

[4]data collected on 11.08.2013

[5]Signal fluctuation could be estimated by averaging over the signal collected within two time units, $2 \cdot t_{\text{twell}}$. This however would increase the velocity spread.

[6]Determined by the t_{dwell} of the time-of-flight card.

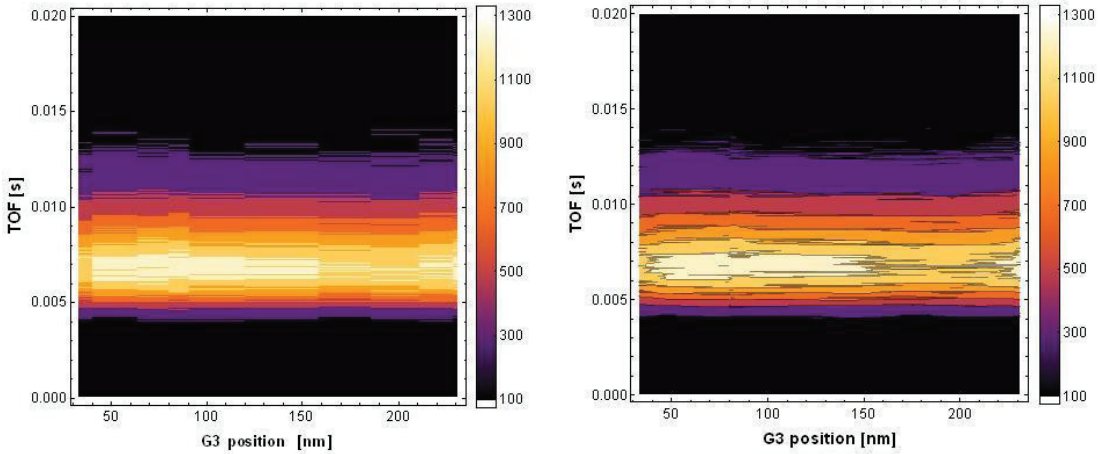

(a) Raw data

(b) Interpolated data

Figure 4.7: Dataset at S3 position: 378400

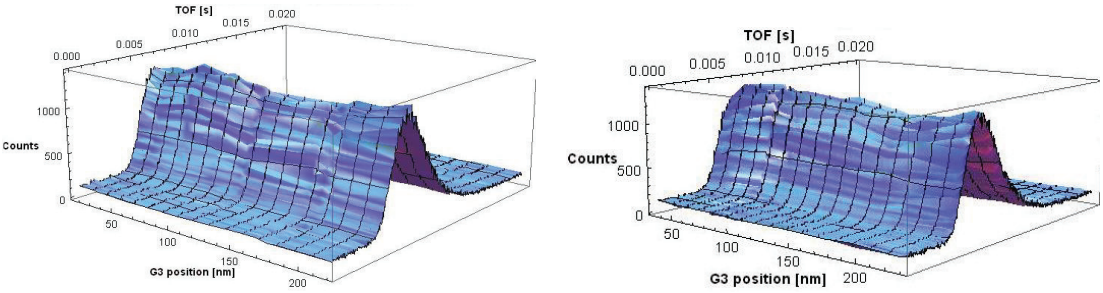

(a) 3D plot at S3 position: 378300

(b) 3D plot at S3 position: 378400

Figure 4.8: The raw time-of-flight data are plotted as a function of time and x-position of G3.

show a smaller periodicity of roughly 170 nm for both positions.

The difference between the fitted period and the expected period of 257 nm can be explained by the linear drift of the other gratings with respect to the scanning grating. During the measurement of one data set, a total drift with a reasonable velocity of 4 nm/min is obtained which is comparable to the drift of 3 nm/min for the light grating mirror in the KDTLI, as seen in section 7.

However, there are few important aspects to be mentioned before the final conclu-

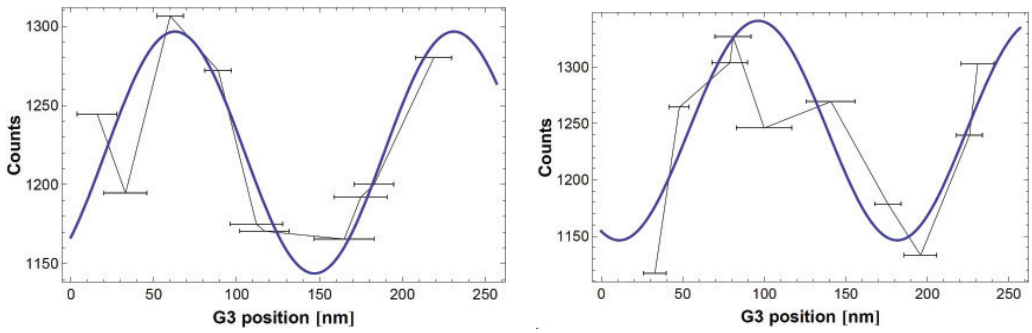

(a) Interference fringe fit at S3 position: 378300 with a visibility of 7% and a period $d = 176$ nm

(b) Interference fringe fit at S3 position: 378400 with a visibility of 9% and a period $d = 170$ nm

Figure 4.9: Sinusoidal visibility fits at the velocity of 162 m/s with a velocity spread of 2%. The horizontal error bars indicate the uncertainty of transverse G3 position while horizontal error bars could not be given since more measurements at these positions are needed.

sion. The observed interference pattern might also occur by accident due to the instability of the oven output. Here, I plotted the peak value of the time-of-flight data with the respect to the grating positions in the order of measurement in Fig. 4.10. Over the course of a single data set a 10% increase and decrease in signal was observed for data plotted in Fig. 4.6 and Fig. 4.7, respectively. Due to the random order of the measured grating positions the interference pattern might be explained. On the other hand, observing interference-like pattern in two subsequent measurements do not appear to be realistic since all other data have clearly shown no such pattern at all. But the alignment requirements clearly state that an extremely high precision of 6 μm is necessary for the longitudinal position. By choosing a step size of 100 μm by which the third gratings is moved one would easily miss the interference.

For these reasons, I believe that a conclusion might be premature at this stage. Further measurements around those positions need to be done.

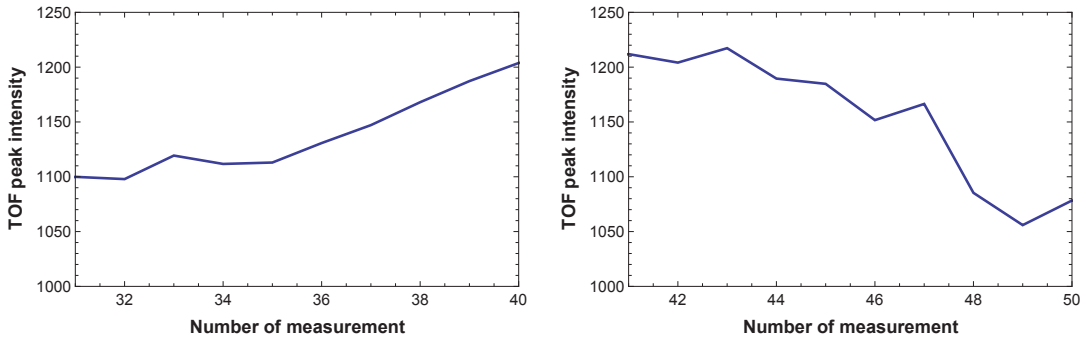

(a) S3 position: 378300

(b) S3 position: 378400

Figure 4.10: Variation of the peak intensity over the measurement process

4.3 Problem analysis and further improvement

In the current measurement scheme a large amount of data need to be dismissed due to the large drift of the scanning stage. This issue can be addressed by changing the interference scan scheme. Instead moving the scanning stage back to its original starting position in a new visibility measurement, it can be moved in the reverse direction to avoid large step sizes. This is illustrated in Fig. 4.11.

From my point of view, the issues regarding the stability and the intensity of the signal might need to be solved primarily. Extending the sublimation duration of the oven would tremendously improve the duration of an interference search procedure. Since the signal has always been weak in our experiment, a 120-s signal integration appears to be necessary for the data analysis. A regular oven refill of roughly 200 to 300 mg C_{60} lasts only few hours at 630°C in this setup. A lower temperature would extend the sublimation duration but the signal becomes even weaker.

On average, 80% of the original filled C_{60} remains in form of black powder after sublimation in the oven. Overheat of the molecules was found because an larger mismatch between the actual oven temperature and the measured temperature than the Comsol simulation predicted in section 3.1.2. On the other hand, the

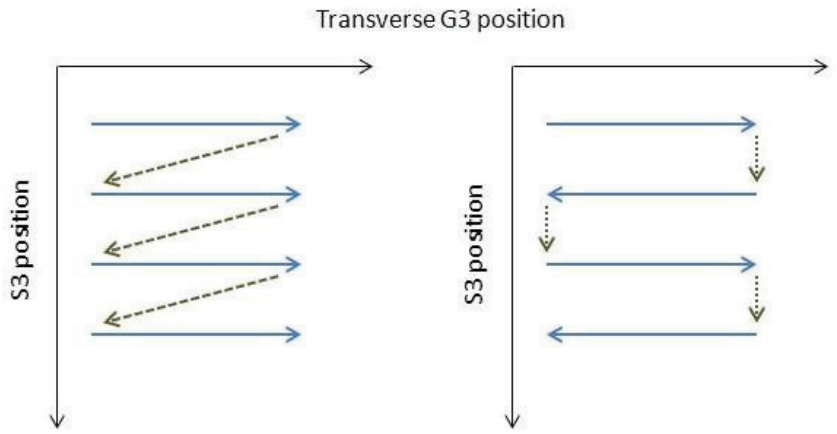

Figure 4.11: Moving scheme of the scanning stage. The current method (left) requires a large jump in G3 position at the beginning of each visibility measurement. The new moving scheme would avoid this.

signal was monitored continuously as the temperature increased and any trace of premature signal was not observed at lower temperature. Since the actual count rate started to increase around the sublimation temperature of 450°C, there might be a non-linear behaviour of the temperature mismatch.

The transmission through the chopper is also responsible for the weak signal. With 1 mm chopper slits, only 7% of the molecules will pass through the chopper. One would increase the signal transmission up to 50% by enlarging the slit width. In order to simplify the data analysis the chopper function needs to be a random function [55] as implemented in the KDTLI at the University of Vienna.

To additionally improve the signal, a two dimensional translation stage for the QMS might be beneficial for better alignment. The pressure within the chamber needs to be as low as possible. I approximated the effective collisional cross section using the experimental data and the equation from Ref. [56] for C_{70} and find out that the mean free path can be doubled to 4 meters by reaching 10^{-8}mbar during measurements, as seen in Fig. 4.12. This would also decrease the collisional decoherence effect [56].

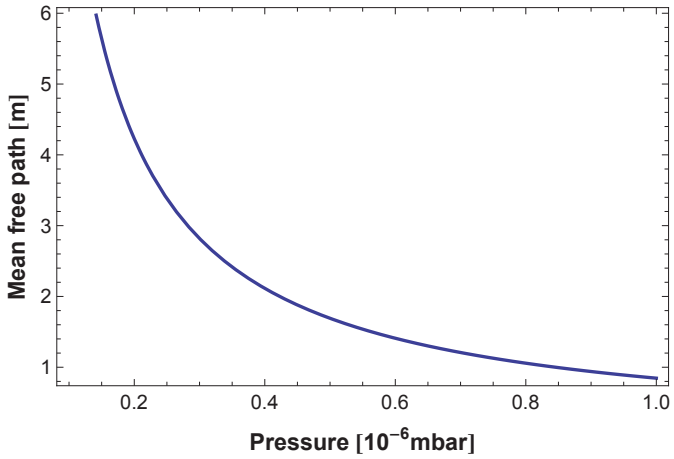

Figure 4.12: Mean free path of C_{70} in N_2 at 300 K

The main difference between the setup at the University of Southampton and the setup at the University of Vienna is the experimental orientation. Since the TLI is vertically mounted gravitational and Coriolis forces are worth discussing. Both forces can lead to additional velocity-dependent phase shift [57] which reduces the interference visibility due to the finite velocity spread. The molecule will be deaccelerated when it propagates through the interferometer. This deacceleration results in a difference in the flight times between the first and the second grating and the second and the third grating. However, for C_{60} with a mean velocity of 170 m/s and a TLI with a grating separation of 39 mm, the phase shift caused by deaccelerating the molecules is estimated to be below $\Delta\phi < 0.0002$. This is negligible.

However if a 1° mismatch in alignment between the grating and the gravitational acceleration is present the visibility could be reduced to 73%[7]. The Coriolis force on the other hand has a smaller contribution to the visibility reduction. Using our experimental data we estimate that the visibility can be reduced to 99.97% for a velocity spread of 2%.

Also, the grating vibration causes further reduction. A more rigours analysis can be found in Ref. [57]. In our setup the grating vibrations caused by the scanning

[7]This estimation is based on Ref. [57]

stage might play a less important role for two reasons. First, due to the horizontal orientation of the grating horizontal movement of the scanning stage might not easily excite the vertical vibrational modes of the grating membrane. Secondly, after moving the scanning stage a 20-s delay is implemented into the Labview program for system stabilization before collecting any data. Since the reasons above are only speculations measuring the grating vibration is necessary. We use Fourier analysis to determine the grating vibrations from the retro-reflected alignment laser from the grating surface. However, this method does not seem to be sensitive enough. An interferometric method might need to be employed.

Part II

The Kapitza-Dirac-Talbot-Lau interferometer (Vienna)

Chapter 5

Theory of the Kapitza-Dirac-Talbot-Lau interferometer

In section 2.5.1, we have analysed the interaction between the molecules and the grating walls in the Talbot-Lau interferometer (TLI). It was suggested to replace the second grating by an optical phase grating using a standing light wave [29] to overcome these interactions. In this chapter the theoretical difference of this new Kapitza-Dirac-Talbot-Lau interferometer (KDTLI) will be compared with TLI. Fig. 5.1(b) illustrates the conceptual setup.

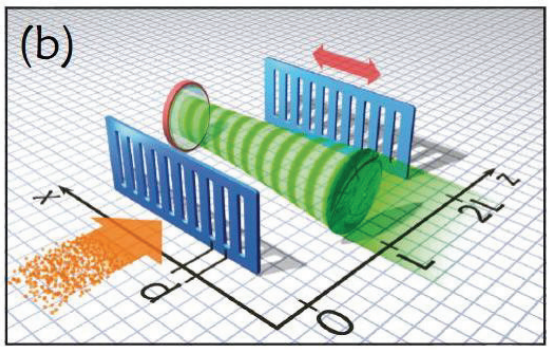

Figure 5.1: The KDTLI consists of two identical material gratings and an optical phase grating. Figure taken from Ref. [19].

5.1 Kapitza-Dirac effect

Kapitza-Dirac effect was first postulated by P. L. Kapitza and P. A. M. Dirac [25] to use a standing light wave to produce a beam splitter for electrons. It was also observed in several experiments for atoms and molecules ([58, 59, 34]...). The interaction between the propagating molecules and the standing light grating is described by the Kapitza-Dirac effect. A detailed description can be found in Ref. [27, 28, 71].

Two counter-propagating identical laser beams create a standing light wave with a period of half the laser wavelength, $\lambda/2$. The electric field E induces an electric dipole potential V^{dip} given by [71]

$$V^{\mathrm{dip}}(x,z) = -\frac{1}{2}\alpha_{\mathrm{opt}}\overline{E^2(x,z,t)} \tag{5.1}$$

where α_{opt} is the optical polarizability of the test particle propagating through this optical grating in the z direction with the velocity v_z. This dipole force induces a position-dependent phase shift $\phi(x)$. For the case of off-resonant interaction between the laser beam and the particle, absorption can be ignored and we can approximate the grating by a pure optical phase grating. The corresponding transmission function t^{dip} is estimated by integrating the potential along a straight line in the eikonal approximation [71]. We have

$$t^{\mathrm{dip}} = \exp(i\phi(x)) = \exp\left(-\frac{i}{\hbar}\int V(x,z,t)dt\right) = \exp\left(i\phi_0 \sin^2(2\pi x/\lambda)\right) \tag{5.2}$$

where

$$\phi(x) = \phi_0 \sin^2(2\pi x/\lambda) \tag{5.3}$$

and the maximal phase shift is given by [71]

$$\phi_0 = \sqrt{\frac{8}{\pi}}\frac{P\alpha_{\mathrm{opt}}}{w_y v_z \hbar c \epsilon_0}. \tag{5.4}$$

w_y is the waist of the standing light grating perpendicular to the particle beam, v_z is the velocity and c is the speed of light. A full description of the Kapitza-Dirac effect includes also the photon absorption which modifies the interference contrast.

The maximal absorbed photon number is given by [71]

$$n_0 = \frac{8}{\sqrt{2\pi}} \frac{\sigma_{\mathrm{abs}} \lambda_L}{hc} \frac{P}{w_y v_z}. \tag{5.5}$$

Each absorbed photon transfers its momentum to the molecular beam which leads to an additional phase shift in the direction of the absorbed photon. Summing up all individual interference patterns of the deflected and undeflected molecules would wash out the interference contrast. Even though many large molecules store the photon energy for a relatively long time, via metastable excitation or internal conversion into vibrational states, any spontaneous emission with the undetermined emission direction would also decrease the interference contrast. However, a systematic control over such decoherence effect appears to be a sensitive tool for molecular metrology, as seen in chapter 8.

5.2 Kapitza-Dirac-Talbot-Lau interferometer

The optical grating avoids interactions between particles and material grating and it improves signal transmission and grating stability. In order to demonstrate the idea of KDTLI let us ignore the absorption in the optical grating.

When the molecular beam propagates through the periodic electric field an additional phase (Eq. 5.4) will be imprinted on the molecular wave function. During the evolution, a modulated particle density pattern is created at the third grating according to the Talbot effect.
The expression of the total transmitted signal in Eq. 2.10 is generally valid. The replacement of the middle grating changes the grating kernel function, Eq. 2.9. Since the absorption in the optical grating is ignored we are only dealing with a purely optical phase grating with

$$T_{\mathrm{phase}}(x,p) = \frac{1}{2\pi\hbar} \int ds e^{ips/\hbar} \exp\left(i\phi\left(x - \frac{s}{2}\right) - i\phi\left(x + \frac{s}{2}\right)\right) \tag{5.6}$$

as the convolution kernel where ϕ is defined by Eq. 5.3. Taking the sinusoidal shape of our light grating, the Fourier coefficient b_m of the transmission function

of the second grating can be described by

$$b_m = (-i)^m \mathrm{e}^{i\phi_0/2} J_m\left(\frac{\phi_0}{2}\right) \tag{5.7}$$

where J_m is the m-th integer order Bessel function and ϕ_0 is given by Eq. 5.4. The B_l coefficient in Eq. 2.11 changes to

$$B_l(\xi) = J_l\left(-\zeta_{\mathrm{phase}}(\xi)\right)$$

where

$$\zeta_{\mathrm{phase}}(\xi) = \phi_0 \cdot \sin(\pi\xi) \tag{5.8}$$

describes the coherent diffraction with $\xi = L/L_T$. Finally, the Visibility can be approximated by

$$\mathrm{Vis} = 2 \cdot \mathrm{sinc}^2(\pi f)\left|B_2\left(\frac{L}{L_T}\right)\right| \tag{5.9}$$

with the opening fractions f of the first and the third grating set equal. The most significant difference between the TLI and the KDTLI is illustrated in Fig. 5.2(a) where the KDTLI shows interference contrast over a much broader range of wavelengths. Here, a numerical prediction of the visibility is plotted as a function of the de Broglie wavelength for C_{70}. A 10% velocity spread, an absorption cross section of $2.1 \cdot 10^{-21}$ m^2 and an optical polarizability of 118 $\mathring{A}$ are used for the simulation. At a diffraction laser power of 5 W the interference contrast is illustrated in dashed line without absorption part. The visibility peaks are affected in their heights and shapes if absorption[1] is included as shown by the red line. For comparison, the visibility of TLI is simultaneously shown as a blue solid line for a narrow velocity spread of $\Delta\lambda/\lambda \approx 0.7\%$. When the velocity spread is increased to 10%, the interference contrast drops to 5%. Due to the wide velocity acceptance range the KDTLI exhibits its higher interference contrast under similar experimental conditions.

[1]The absorption effect was considered at the time as an incoherent process in the standing light wave. An exacter theory of absorption in the light grating is in development where the indistinguishability of photon in the light grating is taken into account. This results in a superposition of opposite photon momentum transfer in the standing light wave [19].

Regarding the classical Moiré effect, the absorption and the momentum exchanging effects of the photon are treated in the same way where the momentum kick is given by [30]

$$Q(x) = -\int_{\infty}^{\infty} dt \frac{dV(x, v_z t)}{dx} \tag{5.10}$$

where the gradient of the optical dipole potential $V(x)$ is the classical force. It was shown in Ref. [71] that the expression for the visibility in the classical regime differs in the B_2 coefficient in Eq. 5.9. Fig. 5.2(b) and (c) show the simulated comparison between the quantum mechanical and the classical model. The quantum visibility is in general higher than the classical prediction. In the Moiré case, the dipole potential acts as lenses focusing the particles beam. The visibility plots are highly dipole potential dependent in both cases. Also the effect of increasing absorption is indicated in black, blue, green and red for $n_0/\phi_0 = 0$, 10, 25 and 50%, respectively.

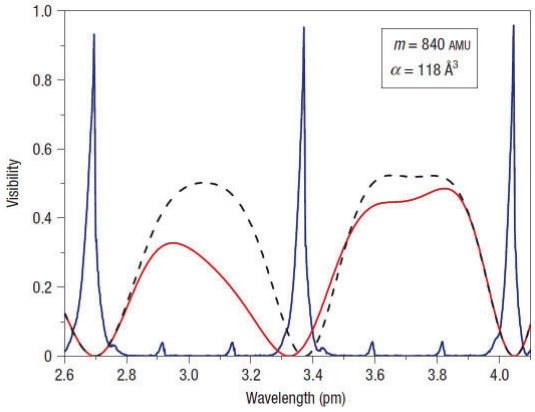

(a) A comparison between the visibility plots of the TLI and the KDTLI with respect to the de Broglie wavelength. Figure taken from Ref. [48].

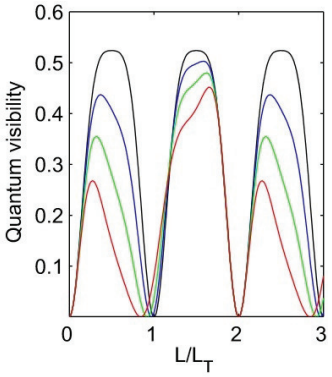

(b) Quantum interference contrast plotted against Talbot length. Figure taken from Ref. [71].

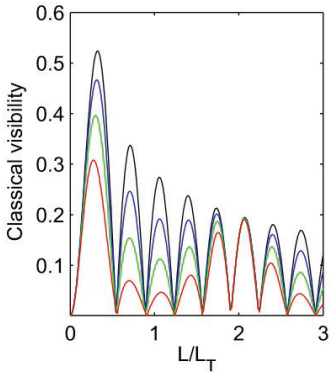

(c) Moire contrast plotted against Talbot length. Figure taken from Ref. [71].

Figure 5.2: Numerical simulations of the visibility plot in dependence on the de Broglie wavelength are plotted here. C_{70} is used as test molecules. The expected visibility peaks of the TLI (blue line) are expected around the tales of the visibility peaks of the KDTLI in (a) where red and dashed lines indicate the simulation with and without having taken the absorption effect into calculation, respectively. In (b) and (c) the quantum and classical visibilities for the KDTLI are shown in dependence of velocity. A generally higher visibility is expected for the quantum interference. The vanishing contrast at the integer numbers of L/L_T is due to the Talbot effect which rebuild the initial particle density at the light grating.

Chapter 6

Experimental setup

In this chapter I will introduce the setup of the Kapitza-Dirac-Talbot-Lau interferometer (KDTLI) at the University of Vienna. I will cover the most significant different experimental components, also in comparison to the TLI setup reviewed in the first part of the thesis.

6.1 Setup

The KDTLI is horizontally orientated which has the advantage of lower vibrations of the entire system than the vertical orientation. The entire setup sits on an floated optical table and is illustrated in Fig. 6.1. The KDTLI is divided into three chambers, the oven, the interferometer and the detection chamber.

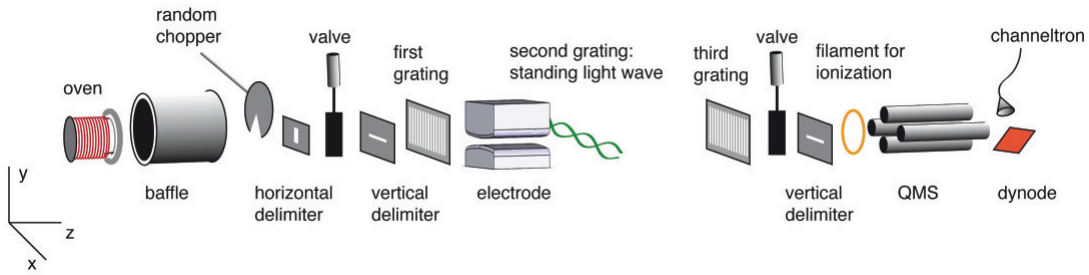

Figure 6.1: Experimental setup of the KDTLI. Figure taken from Ref. [54] and modified by the author.

In the oven chamber, a resistively heated molecular source prepares the molecular

beam. A baffle cooled with liquid nitrogen is used to decrease the residual gas pressure. A chopper is located after the baffle for velocity and time-of-flight measurements. The typical pressure in the oven chamber is below 10^{-8} mbar at room temperature.
A valve separates the oven chamber from the interferometer chamber. Two silicon nitride gratings of period of 266 nm are used as the first and the third gratings where their roll and yaw angles are adjustable using picomotors. We use a standing light beam as an optical phase grating for G2 (see section 6.3.2). A pair of electrodes can be insert between the first and the second gratings for Stark deflectrometry. In addition to the turbo pumps, an ion getter and a sublimation pumps help to reach a base pressure in the 10^{-9} mbar regime.
A commercial QMS (Extrel CMS) with electron impact ionization is employed for the molecule detection in the detection chamber. Velocity selection was achieved using vibration-free gravitational selection where three delimiters define a free fall parabola, as described in section 6.3.1. A more detailed description of the setup is available in the PhD thesis of Stefan Gerlich [61].

6.2 Experimental improvement

In this section I will review the main differences between the KDTLI and the TLI. Specific components such as the pseudorandom chopper, gravitational velocity selection and the light grating will be explained.

6.3 Pseudorandom chopper

In section 3.1.4 a chopper with equally separated slits can be used to measure the velocity distribution under the assumption that the time-of-flight signals from neighbouring slits do not overlap. This sectioning entails a low signal. In section 4.1 we also see that the signal $S(t)$ is given by a convolution of the molecular arrival time distribution with the chopper gate function $f_{\text{chopper}}(t)$. From S and f_{chopper} the original velocity distribution can be reconstructed through a deconvolution.
Another attractive method [55] is to use a chopper with a pseudorandom gate

function. This idea follows: the detected signal can be described by

$$S(t) = \int_0^\infty d\tau f_{\text{chopper}}(t-\tau) g_v(\tau) \tag{6.1}$$

where $f_{\text{chopper}}(t)$ varies from 0 to 1 corresponding to the beam being completely blocked or transmitted, respectively. If we can substitute $f_{\text{chopper}}(t)$ by a delta function $\delta(t)$, the velocity distribution is recovered

$$S(t) = \int_0^\infty d\tau \delta(t-\tau) g_v(\tau) = g_v(t). \tag{6.2}$$

Here, we use the fact that the autocorrelation function of a random function is a delta function [55] and define a new random chopper function $R(t)$ as

$$R(t) = 2 f_{\text{chopper}}(t) - 1 \tag{6.3}$$

which ranges from -1 to 1. Then we cross-correlate $R(t)$ and $S(t)$ [55]

$$I(t) = \int_{-\infty}^\infty d\tau S(t+\tau) R(\tau) \tag{6.4}$$

$$= \int_{-\infty}^\infty d\tau \int_0^\infty d\lambda f_{\text{chopper}}(t+\tau-\lambda) R(\tau) g_v(\lambda)$$

$$= \int_0^\infty d\lambda g_v(\lambda) \cdot \frac{1}{2} \left(\int_{-\infty}^\infty d\tau R_{\text{chopper}}(t+\tau-\lambda) R(\tau) - \int_{-\infty}^\infty d\tau R(\tau) \right)$$

Using the fact that the autocorrelation function of $R(t)$ being a delta function and the integral of a random function being zero, the original g_v yields out

$$I(t) \approx \int_0^\infty d\lambda \delta(t-\lambda) g_v(\lambda) \approx g_v(t). \tag{6.5}$$

In practice, a purely random sequence of chopper openings is not possible. Therefore, a pseudorandom sequence X_n (Fig. 6.2) is chosen which is derived from the chopper sequence $F_{\text{chopper}_n} = (X_n + 1)/2$ as Eq. 6.3. X_n with values ± 1 of a length of N is separated by a given time interval Δt. If this sequence fulfils the condition $\sum_{n=1}^N X_n = +1$ [60] the cross correlation between the sequence X_n and F_{chopper_n}

will be a delta function [60]. By replacing the integral in Eq. 6.5 the velocity distribution can be recovered. In addition, this method also increases the molecular beam transmission up to 50% due to the pseudorandom chopper function.

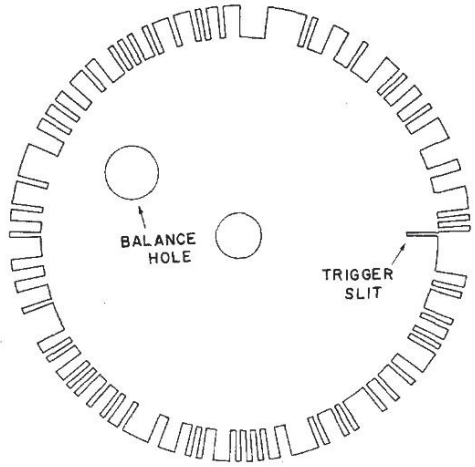

Figure 6.2: A pseudorandom chopper with 255 slots. Figure taken from Ref. [60].

6.3.1 Gravitational velocity selection

Horizontal delimiters in the interferometer in Fig. 6.1 are used to collimate the molecular beam. Vertical delimiters narrow the velocity distribution. The idea of velocity selection is sketched in Fig. 6.3. In a gravitational field, molecules of different velocities follow different free-flight parabolas. Three points are necessary to define such parabolas. We define the oven orifice of 2×0.2 mm^2 as the first point. 1.18 m away from the oven, we insert a piezo slit as the second point (D1). Its width is continuously variable between 5 μm and 1.5 mm for a tunable velocity selection. A translation stage with 25 mm moving range enables free positioning. A third aperture (D2) with 3 optional openings of 100 μm, 200 μm and 500 μm height is placed at 1.9 m away from the source.
These slits are usually aligned to the most probable velocity so that a relative velocity selection $\Delta v/v$ of 10-20% can be achieved.

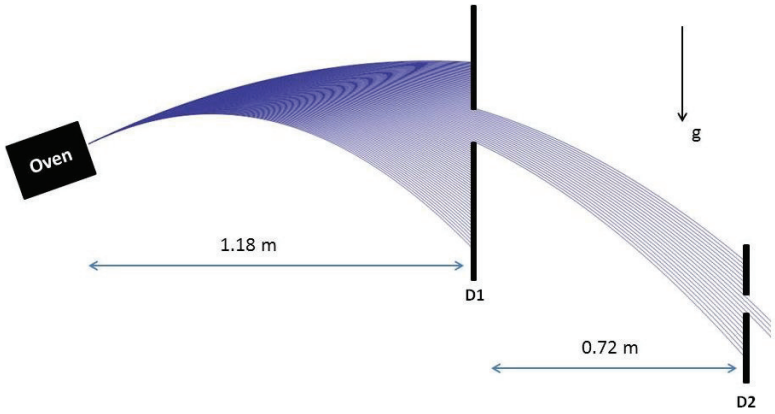

Figure 6.3: Gravitational velocity selection scheme. Oven orifice is used as the first reference position, a slit at position D1 as the second and another slit at D2 as the third reference point. The blue lines show the trajectories of particles coming out of the oven where the highest and lowest trajectories correspond to the fastest and the slowest molecules, respectively.

6.3.2 Light grating

The main difference between the KDTLI and the TLI is the central diffraction grating, G2. The laser beam of a Coherent VERDI V-10 with a wavelength of 532.221 nm is sent into the chamber and retro-reflected by a 0° mirror to create a standing light wave which matches the periodicity of the material gratings. The wavelength can be fine-tuned by changing the intra-cavity etalon temperature. We have monitored the wavelength over the time of each interference scan to ensure that it is stable to reach $\Delta\lambda = 0.001$ nm. By adjusting a half-wave plate (HWP) in front of a polarization beam splitter (PBS) the laser power in the interferometer can be varied. An additional quarter-wave plate (QWP) prevents the retro-reflected light from entering the laser cavity which might damage the laser.
One critical alignment step is to achieve orthogonality between the light grating vector and the molecular beam vector. Any misalignment will lead to an average of the phase imprinted by the nodes and the anti-nodes of the standing light wave as shown in the left box of Fig. 6.4. To alleviate this alignment precision a cylindrical, plano-convex lens with a focal length of 100 mm is insert to decrease the horizontal laser waist to 20μm on the mirror.
The horizontal molecular beam width should not exceed the Rayleigh length which

is given by

$$z_R = \frac{\pi w_0^2}{\lambda} \tag{6.6}$$

where w_0^2 is the waist of the laser beam of a wavelength λ. This is because the radius of the curvature of the laser beam front increases outside of this region. There, the phase imprinted on the molecular wave function will not be contributed only by the part of the standing light wave with constant intensity, rather than an average of the nodes and the anti-nodes of the standing light wave, as seen in the right box of Fig. 6.4. For this reason, the horizontal width of the molecular beam should be approximately equal or smaller to the Rayleigh length of the grating laser.

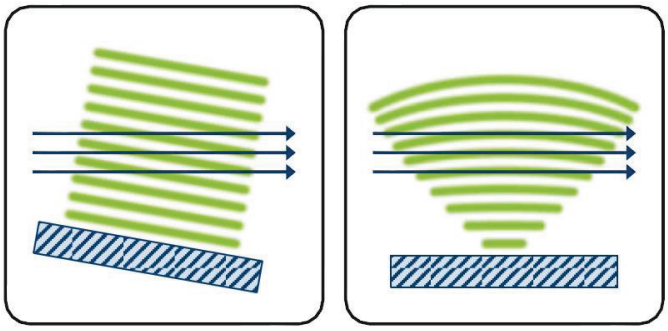

Figure 6.4: For a broad laser beam a higher precision in the laser grating alignment is required since any misalignment influences the effective slit opening (left), as discussed in section 3.3.1. To lower the precision, a focused beam reduces the distance which molecules pass through the light grating. An ideal phase grating can be approximated by narrowing the molecular beam width and by approaching the molecular beam the laser waist (right). Figure taken from Ref. [61].

Chapter 7

Interference measurements

KDTLI was aligned many times in the past, and a sophisticated analysis of the alignment was carried out elsewhere [61]. Therefore, I will only describe some routine procedures necessary to run the interferometer. I will then present some interference measurement.

In order to observe quantum interference the local environment in the apparatus needs to be carefully prepared. Collisional decoherence [56] was observed earlier by increasing the pressure in the interferometer region. The pressure of the interferometer chamber needs to be maintained between 10^{-8}-10^{-9} mbar. Since the KDTLI is sensitive to vibrations one needs also to isolate the interferometer from all possible source of vibration such as various vacuum pumps. In order to decouple the entire apparatus from environmental vibrations the optical table is floated. When the experimental conditions are stabilized we can start our search for interference. First, the molecular beam needs to be aligned to the QMS. Here, we need to assure that all collimation slits are removed from the molecular beam path for maximal transmission and that the laser grating is switched off to prevent any modulation of the signal due to interference while the first and the third grating are fixed in the interferometer. The oven temperature is stable to $\Delta T < 1$K and the signal to $\Delta S/S < 5\%$.

Secondly, when the signal is maximized the gravitational slits and beam delimiters are successively insert into the molecular beam starting from the closest delimiter from the oven. Each slit is aligned for maximal transmission. It is important to

note that the velocity spread can be tuned by varying the width of the piezo-driven slit (D1 in Fig. 6.3) and the QMS slit (D2 in Fig. 6.3), as described in section 6.3.1. In addition, the velocity can be measured by using the pseudorandom chopper.

An important step is to align the laser grating relative to the molecular beam. Since the interference contrast depends on the intensity of the standing light wave it is necessary to adjust the laser grating to the molecular beam. Therefore, we record interference at different positions of the laser grating in order to map out the variation of the interference contrast, as shown in Fig. 7.2(a) and Fig. 7.3(a). We fit a Gaussian to the data to find the position of maximal visibility. However, it is worth adding that the visibility also depends on the laser grating power, as mentioned in Ref. [71]. For this reason the visibility can be improved by optimizing the laser grating power. We collect the data of each interference measurement for different laser grating powers as plotted in Fig. 7.2(b) and Fig. 7.3(b). The dependence is fitted by a Gaussian again. This approximation allows us to have a reasonable guess for the laser grating position and power for maximal interference contrast. The power dependence of the visibility can be also used to determine the optical polarizability of the molecule [62].

The interference visibility is measured by transversely moving the third grating across the molecular beam, while collecting the transmitted signal. A predefined scanning range is divided into equally distanced measurement points with a tunable integration time. A sinusoidal function

$$S(x_3) = S_{\text{off}} + A \cdot \sin(2\pi(x_3 - \Delta x_3)/d) \tag{7.1}$$

is fitted to the data where the offset signal S_{off}, the amplitude of the modulation A, the period d and the phase Δx_3 are the fitting parameters. The visibility can be estimated from $\text{Vis} = A/S_{\text{off}}$.

In the following I will shortly present the interference measurement of β-carotene, C_{70} and resveratrol.

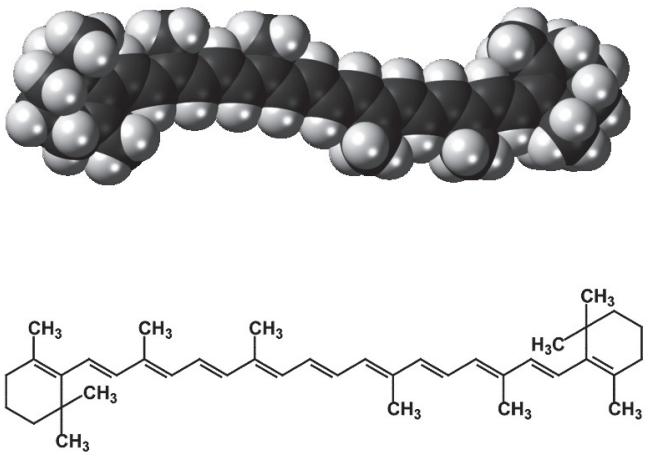

Figure 7.1: The structure of β-carotene.

7.1 β-carotene

One carotenoid which we are interested in is β-carotene with a molecular weight of 536 u. Its structure is sketched in Fig. 7.1. It is red-orange pigment abundant in plants and fruits. It is a non-polar compound dissolvable in non-polar solvent such as acetone. β-carotene was observed to evaporate at a temperature between 170°C-190°C [63]. We confirmed this observation using β-carotene purchased from Sigma Aldrich without further purification. A clear mass peak is visible in the QMS.
In the preparation before mass measurement molecules are dissolved in acetone for an increased packing density. By heating the samples upto 50°C outside of the chamber acetone can be evaporated. The residual acetone results in an increase of the pressure in the oven chamber during heating of the oven. Therefore, the oven chamber needs to out-gas for few hours before β-carotene reaches its sublimation temperature. In addition, "spitting" of the material was observed at around 160°C but this seems to depend on the sample preparation. Decomposition occurs slightly above 196°C.
We ran the experiment at an oven temperature of 190°C. By setting 120 V for the piezo-driven delimiter slit and 200 μm width of the QMS delimiter, a maximal velocity of 193 m/s with 15% velocity spread was measured using time-of-flight measurement. The pure signal intensity is measured to be 120 counts/s with a

dark count of 20 counts/s subtracted.
One interference scan consists of data collected for 42 subsequent positions of the third grating which are separated by 26 nm. The data at each position takes 2 seconds for signal integration. The total interference contrast is calculated as the mean of two interference scans, as shown in Fig. 7.2(c).
For the visibility optimization we set the laser grating power initially to 3.86 W to adjust the laser grating height (Fig. 7.2(a)[1]). Fig. 7.2(b) shows the power dependence of the interference contrast where the reviving effect at 5.3 W indicates two-photon absorption. Each data point is the mean of two interference scans under the same condition and the standard deviations provide the error bars[2]. In the current interferometric setting we achieved a maximal interference visibility of $21.2 \pm 1.9\%$. This is well in the quantum regime and the first observation of a delocalized carotenoid.

7.2 C_{70} and resveratrol

Similar measurements were carried out for the fullerene C_{70}. The oven was heated to 654°C. The molecular beam had a mean velocity of 210 m/s and 18% velocity spread. Using the same procedure for the visibility optimization achieved a maximal visibility of 17.5±1.0%. This is lower than earlier experiments [39], due to imperfect grating alignment. The data shown in Fig. 7.3 are collected on 02.10.2013.

A clear quantum interference was observed for resveratrol with a molecular weight of 228 u. At around 150°C a molecular beam formed. At 235°C we took two interference scans as shown in Fig. 7.3(d). The difference in the mean counts resulted in the empty oven. Despite the low visibility of 4%, we are confident that the interference contrast of resveratrol can be further improved and it has the potential for further investigation.

[1]Data taken from 26.09.2013
[2]The error of the laser power is mainly given by the error of the powermeter of 3-4%.

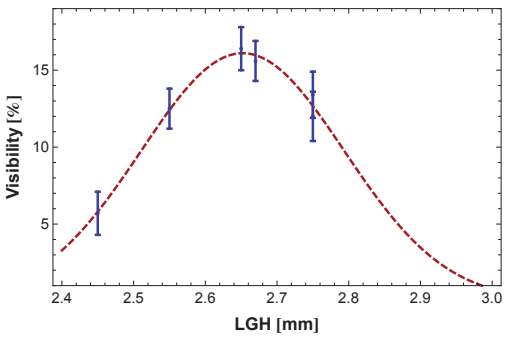

(a) Visibility in dependence of the laser grating height

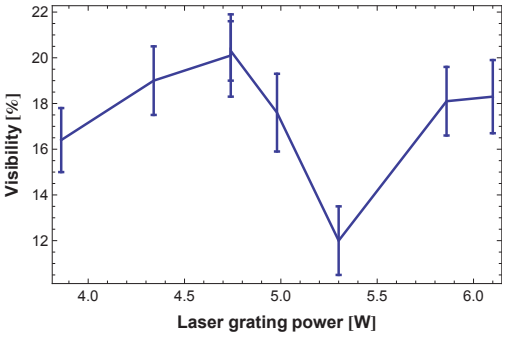

(b) Visibility in dependence of the laser grating power

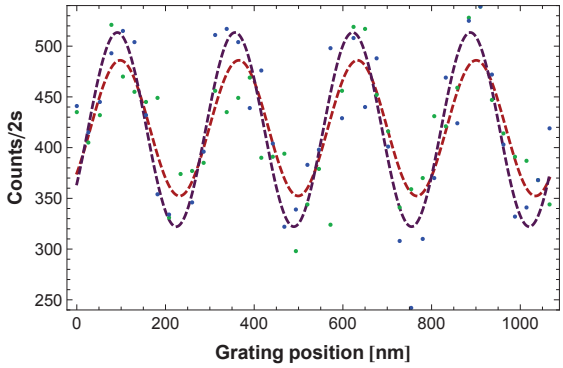

(c) Two interference scans with 2 seconds integration time per data point.

Figure 7.2: Visibility plots for β-carotene: (a) shows the visibility dependence of the laser grating height at a fixed laser power of 3.86 W. In (b) a strong power dependence occurs between 5 and 6 W of laser power due to 2-photon absorption. In (c) two visibility scans yield out a mean interference contrast of 21.2±1.9% with a laser grating power of 5.3 W. The purple and the red dashed lines are the fits of the blue and the green data points, respectively using Eq. 7.1.

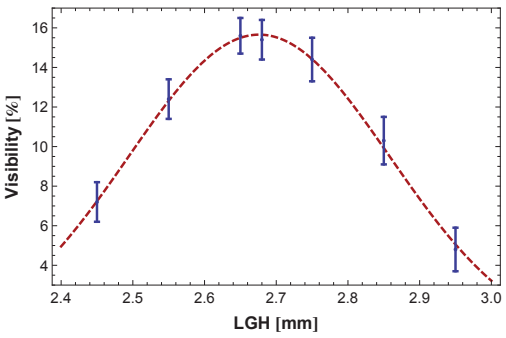

(a) C_{70} visibility in dependence of the laser grating height

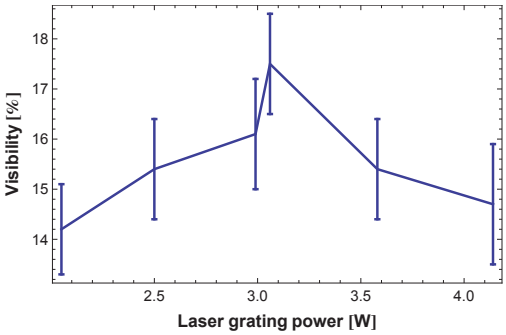

(b) C_{70} visibility in dependence of the laser grating power

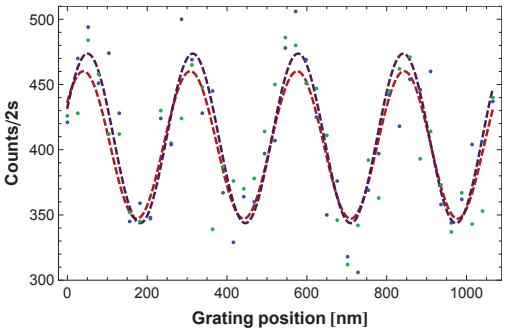

(c) Two visibility scans for C_{70} with a laser grating power of 2.5 W. By taken the dark count of 14/s into account we estimated an mean visibility of 17.5±1.0%.

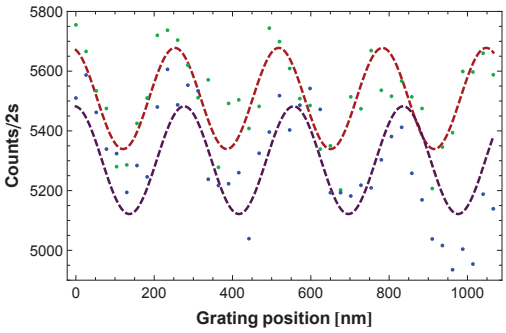

(d) Two visibility data for resveratrol are fitted by red and blue sinusoidal function, respectively. the shift in the mean count rate results in the decreasing signal of a nearly empty oven.

Figure 7.3: Visibility plots for C_{70} and resveratrol

Chapter 8

Application: Absolute absorption cross section measurement

Optical spectroscopy is able to reveal electronic, vibrational, rotational and structural properties of atoms or molecules. Absorption measurement in a vapor cell often only provides relative spectral knowledge. Using methods of photon depletion [65], [66], photon fragmentation [67] or measuring the survival time in a penning trap [68], the absolute photon absorption cross section could be measured for small volatile molecules. However, the accuracy of the absolute absorption cross section is often limited by the knowledge of the particle number density. For larger molecules in the gas phase, knowing this number is a non-trivial task. Due to the low density of complex molecules gas spectra are often extrapolated from solvent analysis [69].

In some cases, a non-invasive method is desirable as well. To bypass the limitations above, the KDTLI is perfectly suited for dilute gas beam. In this chapter, we will demonstrate for the first time an experiment that was initially proposed by Nimmrichter et al. [64]. In this demonstration, we use interference to determine the absolute photon absorption cross section of C_{70} by comparing the deflected and undeflected molecular interference patterns. This photon-induced deflection leads to a reduction of the interference visibility and allows us to precisely determine changes caused by the recoil of single photon.

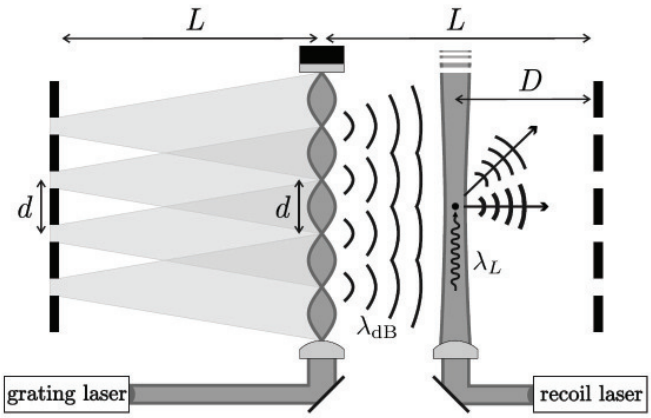

Figure 8.1: Schematic of the experimental setup for the absolute absorption cross section measurement. An additional recoil laser with a wavelength of λ_L is introduced at the distance D between the optical grating and the grating mask. Depending on its position and the photon momentum, the interference fringe of the propagating molecules will be shifted along the k vector of the recoil laser after momentum transfer. Figure taken from Ref. [64].

8.1 Theoretical analysis

A detailed theoretical description is available in Ref. [64]. Here, we introduce the theory shortly and extend it for a finite velocity spread as predicted for the actual experiment. The basic idea is to exert an external force on the propagating molecular wave in the interferometer in order to add an additional phase shift. The magnitude of the phase shift changes the interference visibility. First of all, let's characterize the molecular motional state using the Wigner function $w(x, p)$ of the transverse position x and the momentum p in a longitudinally moving frame of molecules with the velocity v_z.

Figure 8.1 illustrates the basic setup. An additional recoil laser of wavelength λ_L is set parallel to all the gratings and perpendicular to the molecular beam. It is located between the optical phase grating and $G3$. Each photon absorbed from the recoil laser leads to a momentum kick which depends on the wavelength of the absorbed photon $\Delta p = h/\lambda_L$. The interference fringe will then be spatially shifted by an amount s related to the distance D between the recoil laser and the third

grating:

$$s = \frac{\Delta p}{p_z} D = \frac{\lambda_{\mathrm{dB}}}{\lambda_L} D \tag{8.1}$$

where the de Broglie wavelength of the molecules is given by $\lambda_{\mathrm{dB}} = h/mv_z$. The probability distribution of the number of photons absorbed by the flying molecules can be assumed to be Poissonian distributed

$$P_n(n_0) = n_0^n \frac{e^{-n_0}}{n!} \tag{8.2}$$

if the absorption cross section σ_{abs} remains unchanged after the first excitation. The average number of absorbed photons is calculated for a Gaussian laser beam profile to be

$$n_0 = \sqrt{\frac{2}{\pi}} \frac{\sigma_{\mathrm{abs}} P_L \lambda_L}{hc\mathrm{w}_L v_z} \tag{8.3}$$

where P_L the laser power, w_L the waist of the recoil laser beam, h Planck's constant and c the speed of light. Taking this into account, the spatial density distribution at the third grating is given by

$$w_3(x, n_0, s) = \sum_{n=0}^{\infty} P_n(n_0) w_3^{(0)}(x + ns) \tag{8.4}$$

and $w_3^{(0)}$ is the density pattern without the recoil laser. This modified density pattern w_3 can be expanded in a Fourier series as $w_3 = \sum_l w_l \exp(2\pi i l x/s)$ with the Fourier coefficient defined by [64]

$$w_l(x, n_0, s) = w_l^{(0)} \exp\left(n_0 \exp\left(\frac{2\pi i l s}{d}\right) - n_0\right) \tag{8.5}$$

where $w_l^{(0)}$ is the Fourier coefficient of the unperturbed interference pattern which is expanded in the same manner as $w_3^{(0)} = \sum_l w_l^{(0)} \exp(2\pi i l x/d)$.
Eq. 8.4 expresses the final density pattern as a density summation of the shifted and un-shifted interference fringes of the single molecules. Therefore, for a fixed λ_L the position change of the recoil laser D results in a deformation of the interference fringe or a reduction in the amplitude of the modulation. If D is chosen such that the interference fringe is shifted by exactly half a grating period, i.e., $s = d/2$,

additional side peaks are expected. This effect is illustrated in Fig. 8.2. Here, the biodye tetraphenylporphyrin H_2TPP of a mass of 614.75 u is used for the simulation in a TLI. The expected interference fringe for a fixed velocity at $v_z = 175m/s$ is shown in Fig 8.2(a) where the dashed line indicates the fringe without the recoil laser and the solid line for the fringe with the recoil laser. However, from the practical point of view, a finite velocity spread $\Delta v_z/\overline{v_z}$ is to be expected. A spread of 5% would blur the interference fringe, as seen in Fig. 8.2(b).
The appearance of these side peaks in both cases can be used to quantitatively determine the recoil effect. By comparing the amplitudes of the main and side peaks, the absolute absorption cross section can be calculated. However, in the KDTLI, only a reduction of the interference contrast is visible. This is due to the sinusoidal density pattern and the large opening fraction of the scanning grating. We introduce the visibility reduction factor R as $\mathrm{Vis}' = R \cdot \mathrm{Vis}$ where Vis′ and Vis are the modified and unmodified visibility corresponding to the situations with and without recoil laser. As discussed in the previous chapter, the interference contrast is given by

$$\mathrm{Vis} = \frac{S_{\max} - S_{\min}}{S_{\max} + S_{\min}} \approx 2 \left| \frac{S_1}{S_0} \right| \tag{8.6}$$

where S_0 and S_1 are the zero-th and the first Fourier coefficients of the signal function (for more details see Appendix C). With this definition, the reduction factor becomes

$$R = \frac{\mathrm{Vis}'}{\mathrm{Vis}} \approx \left| \frac{S_1'}{S_1} \right|. \tag{8.7}$$

or

$$R(n_0, s) = \exp\left(-n_0 \left(1 - \cos\left(\frac{2\pi s}{d} \right) \right) \right) \tag{8.8}$$

for a fixed velocity v_z.
For a single fixed velocity, $R_{\max} = \exp(-2n_0)$ gives the maximal reduction with respect to the recoil laser position D which occurs at any odd integer multiple of a half a grating period shift. After rearranging $R_{\max}$ in combination with Eq. 8.3, the absolute absorption cross section can be directly deduced at these positions from the linear relation

$$\ln R^{-1} = 2\sqrt{\frac{2}{\pi}} \frac{\lambda_L}{hc\mathrm{w}_L v_z} \sigma_{\mathrm{abs}} P_L. \tag{8.9}$$

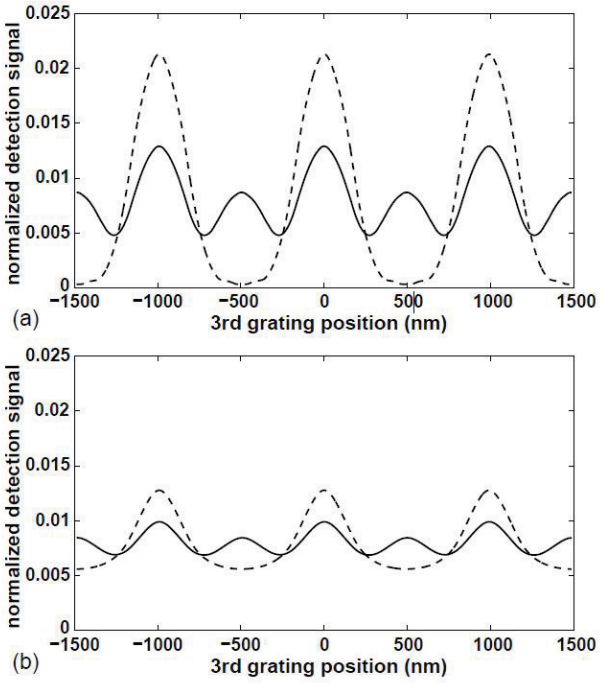

Figure 8.2: Simulation of the expected signal when the recoil laser is set for half-period shift in a TLI. Three identical gratings of period of 911 nm, a thickness of 198 nm and an opening fraction of $f = 1/5$ are chosen. They are separated by the Talbot length $L_T = 26.48$ cm. H_2TPP as the test particle has a mass of 614.75 u, a polarizability of $105\mathring{A}^3$ and $\sigma_{\text{abs}} = 15\mathring{A}^2$. The unperturbed interference patterns are illustrated by dashed lines. The solid lines represent the case with the recoil laser of a 0.5 W 420 nm recoil laser with a waist of 900 μm are shown by dashed lines. at a distance of 5.61 cm away from the third grating for a fixed velocity v_z of 175 m/s and a velocity spread of 5%, respectively in the graphs (a) and (b). Figures taken from Ref. [64].

This method is unaffected by various dephasing mechanism within the interferometer such as grating vibrations, gravitational and the Coriolis forces. Collisions with residual gases and photon absorption in the optical phase grating do not influence the reduction factor because comparisons are made between the fringe contrast with and without the recoil laser.

In order to prevent the absorption of two or more photons in the recoil laser, the laser power needs to be set for $n_0 << 1$. In addition, the velocity spread needs to be taken into account. This results in a reduced visibility $\text{Vis}' = \langle R \rangle_{v_z} \text{Vis}$ with

the reduction factor averaged over the velocity distribution. Since the number of absorbed photons n_0 and the fringe shift s are velocity-dependent, we need also to average over the velocity for each Fourier component [64]. Hence, Eq. 8.8 needs to be replaced by

$$\langle R \rangle_{v_z} = \left| \frac{\langle w_1^{(0)} \exp\left(-n_0 \left(1 - \exp\left(\frac{2\pi i s}{d}\right)\right)\right)\rangle_{v_z}}{\langle w_1^{(0)} \rangle_{v_z}} \right|. \tag{8.10}$$

Here, only the first Fourier coefficient $w_1^{(0)}$ dominates (for more details, see Appendix C). Therefore, we can also write Eq. 8.10 into

$$\langle R \rangle_{v_z} = \left| \frac{\int_0^\infty dv_z P(v_z) \overbrace{A_1^* B_2 \left(\frac{L}{L_T}\right)}^{w_1^{(0)}} \exp\left(-n_0 \left(1 - \exp\left(\frac{2\pi i s}{d}\right)\right)\right)}{\int_0^\infty dv_z P(v_z) \underbrace{A_1^* B_2 \left(\frac{L}{L_T}\right)}_{w_1^{(0)}}} \right|$$

$$\approx \int_0^\infty dv_z P(v_z) \exp\left(-n_0 \left(1 - \exp\left(\frac{2\pi i s}{d}\right)\right)\right). \tag{8.11}$$

with the velocity distribution $P(v_z)$. Here the first Fourier coefficient of the unperturbed interference pattern is given by $w_1^{(0)} = A_1^* B_2 \left(\frac{L}{L_T}\right)$ which is removed from the integral because of the weak velocity dependence. Eq. 8.11 will be required for the data fits for the absorption cross section in chapter 8.3.2.

Fig. 8.3 illustrates the difference between the reduction factors for a fixed velocity and for different finite velocity spreads. For a constant velocity v_0 of 210 m/s, the reduction factor possesses a typical sinusoidal spatial behaviour with respect to the recoil laser position D (dashed line). However, after averaging over a Gaussian velocity distribution, a clear damping effect of the reduction factor is to be expected (coloured lines). For molecules with a low mean velocity or a short recoil laser wavelength, the recoil effect can be simplified by the approximation

$$\langle R \rangle_{v_z} \approx \exp\left(-n_0\right) \tag{8.12}$$

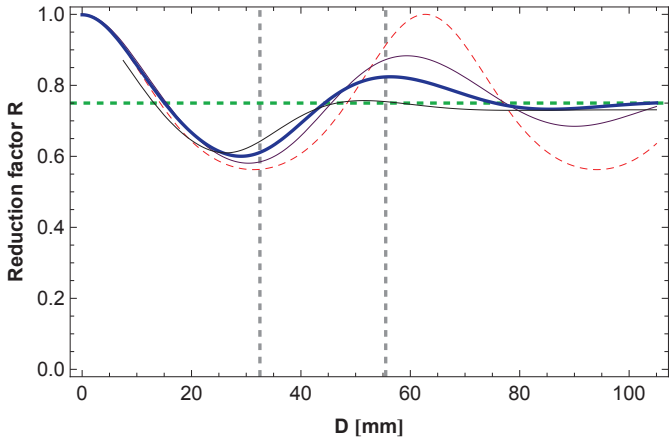

Figure 8.3: The reduction factor as a function of D. The red dashed line shows the periodic effect of R for a fixed velocity $v_0 = 210$m/s. The averaging effects over different finite velocity spreads of $\Delta v/v_0 \approx 17\%$, 26% and 40% are plotted by the purple, blue and black lines, respectively. The approximation for the case insensitive to D is indicated by the green dashed line. The vertical dashed lines give coarsely the range of our experimental accessibility.

if D becomes significantly larger than two times the spatial period of the sinusoidal behaviour of R for a fixed velocity (dashed gray line). In this case, the reduction factor becomes insensitive to D.

8.2 Experimental setup

The measurement scheme is based on the KDTLI setup as described in chapter 6. A schematic of the KDTLI with additional elements for the absorption spectroscopy is shown in Fig. 8.1. An additional 532 nm laser with a waist of 1.23±0.02 mm and a divergence of < 0.5 mrad was purchased from Coherent Inc. as the recoil laser beam, whose beam is set to be parallel to all gratings and perpendicular to the molecular beam. This recoil laser is located between the first and the optical phase gratings due to our experimental accessibility. It is important to note that, for a symmetric interferometer, positioning of the recoil laser beam between the first and the second grating does not change the physical effect. A detailed proof using Wigner function is given in the Appendix D.
C_{70} is effused from a thermal source heated up to 930 K. Using beam delimiters

and gravitational slits we are able to collimate the molecular beam to a width of 1 mm and a height of 200 μm propagating through the interferometer. At the same time, we find that the molecular beam can be described effectively using a Gaussian probability density with a mean velocity of $v_0 = 210.3 \pm 0.7$ m/s with a standard deviation of $\sigma_{v_z} = 38.4 \pm 0.5$ m/s, as described in section 8.2.1.

8.2.1 Velocity distribution of the C_{70} beam

The velocity distribution of the molecules inside the oven can be described by the Maxwell-Boltzmann distribution. However, the shape and the thickness of the oven nozzle have a tremendous influence on the distribution when molecules escape the oven. Despite the complexity, we use the time-of-flight measurement to determine the real molecular velocity distribution.
The trigger signal is produced by a chopper with 64 slits located in a pseudo-sequence, see section 6.3. At a distance of $L = 1.74$ m[1] from the chopper, the beam pulses are detected by the QMS and the signal will be recorded by the MCA-3 Fast ComTec card with a dwell time of 20 μs and a total data acquisition time of 11 s. We deconvolve the raw data from the chopper function to receive the actual time-of-flight curve and repeat this measurement 25 times with the total averaged signals plotted in Fig. 8.4(a). The velocity distribution can be well described by a Gaussian in the domain of time-of-flight t,

$$N(t) = N_0 \exp\left(-\frac{(t-t_0)^2}{2\sigma_t^2}\right) \tag{8.13}$$

where N_0 is the maximal count, t_0 is the expected value for the time-of-flight and σ_t is its standard deviation. From the fit, we obtain $t_0 = 8.28 \pm 0.02$ ms and a standard deviation of $\sigma_t = 1.84 \pm 0.02$ ms, corresponding to a mean velocity of 210.3 ± 0.7 m/s within an asymmetric velocity range between 171.9m/s and 270.2 m/s, as seen in Fig. 8.4(a). However, for further calculations we approximate the velocity distribution by a Gaussian in the velocity domain with a mean velocity of $v_0 = 210.3 \pm 0.7$ m/s and a symmetric standard deviation of $\sigma_v = 38.4 \pm 0.5$ m/s.

[1]The optical phase grating is switched off during the time-of-flight measurement in order to prevent any interference by accident which may reduce or increase the detected signal.

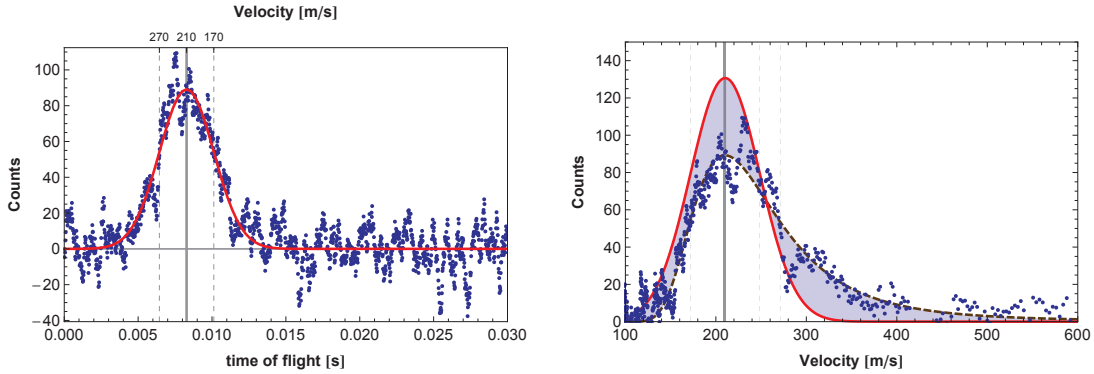

(a) Time-of-flight signal.

(b) Velocity distribution with two fitting statistics.

Figure 8.4: The time-of-flight signal (a) recorded for a distance of 1.74 m between the trigger and the detection. The blue points represent the averaged data over 25 measurements. The density distribution is well fitted by a Gaussian distribution (red curve) with the mean time-of-flight of 8.28 ± 0.02 ms (thick gray line) and a standard deviation of 1.84 ± 0.02ms (dashed gray lines). The velocity distribution is fitted by two fitting statistics in (b). The red curve is the approximated Gaussian distribution of velocity. The brown dashed curve is the Gaussian fit in time converted into velocity. The thick and dashed gray lines indicate the mean velocity and the symmetric/asymmetric standard deviations for each fitting, respectively. The blue shadowed area gives the rearranged statistics.

The effect of this approximation is negligible small which will be demonstrated in the next section. The difference between those fits are plotted in Fig. 8.4(b).

8.2.2 The recoil laser

The ideal requirements for the recoil laser as the probe laser for spectroscopy are the wavelength and power tunablity. However, in our experiment, we aim for experimental demonstration of the method for single wavelength. A cw laser (V-18 of Coherent) provides a stable wavelength λ_L of 532.2199 ± 0.0001 nm which varies by less than one part in 10^4 over the course of the measurement. The power is regulated by a half-wave plate followed by a polarisation beam splitter, similar to the power regulation of the light grating. Using the knife-edge beam profiler of the BeamMaster (BM2421) we find the recoil laser having an almost symmetric

Gaussian profile with a stable mean value for the beam waist of $w_L = 1.23 \pm 0.02$ mm for different powers and a divergence of < 0.5 mrad. The cross sectional intensity distribution is well described by:

$$I(y,z) = \frac{4P_L}{2\pi w_y w_z} \exp\left(-\frac{2y^2}{w_y^2} - \frac{2z^2}{w_z^2}\right) \tag{8.14}$$

where P_L is the recoil laser power, w_y, w_z are the waists in y and z axis which are set equally to the mean value w_L. Taking current literature value for the absorption cross section for C_{70} at 532 nm to be $(2.5 \pm 0.3) \cdot 10^{-21}$ m^2[71], the maximal mean absorbed photon number[2] is ≈ 0.14 at a maximal recoil laser power of $P_{\max} = 17.4 \pm 0.9$ W for a velocity of 170 m/s, calculated by averaging Eq. 8.15. This fulfils the condition of $n_0 << 1$ in our model. We have then a position-dependent averaged photon number:

$$n_0 = \sqrt{\frac{2}{\pi}} \frac{P_L \lambda_L \sigma_{\text{abs}}}{hc w_y v_z} \exp\left(-\frac{2y^2}{w_L^2}\right) \tag{8.15}$$

We use two 45° mirrors to deflect the recoil laser into the chamber. Since there is only one optical port available for the recoil laser in our vacuum chamber, the positioning range of the recoil laser lies between the first and second gratings and the distance relatively to the first grating is limited between $3.5 \leq D \leq 5.5$ cm.
Another reasonable concern regarding the position of the recoil laser is the triplet state of C_{70} which possesses a different optical polarizability, i.e., a different phase will be imprinted upon the wave function of the triplet state in the optical phase grating. This might lead to a further reduction in visibility. However, according to Ref. [72] the lifetime of the triplet state of C_{70} is $\tau = 41\mu s$. A molecule with 270 m/s needs 180 μs to pass a distance of 5 cm between the recoil laser and the optical phase grating. This is significantly longer than the lifetime of the triplet state of C_{70}. We therefore expect very few molecules to be in the excited state.

[2] n_0 decreases with the increasing velocity.

8.3 Measurement

The data are collected within many days with the special care taken on the interferometer conditions, ie., the vacuum pressures, the oven position, the velocities of molecules, powers and wavelengths of the laser grating and the recoil laser. In order to have repeatable measurement conditions, all mentioned parameters are monitored as reference for the entire measurement. In this section, a protocol for the data collection is presented. The final absolute absorption cross section of C_{70} will be estimated by a time consuming data analysis in the last subsection.

8.3.1 Data collection

Due to the experimental accessibility the range for the recoil laser position is limited to 2.5 cm between the first and the second gratings. The molecular beam is due to its dilute density not visible by eyes. In order to find the molecular beam, we use the lower edge of the vertical movable unused electrode to cut the molecular beam. By slowly moving the electrode into the interferometer, we can roughly determine the position of the beam when the count rate drops to the half. With this as reference point, the recoil laser is coarsely aligned to the edge of the electrode. The accurate alignment follows by vertically moving the recoil laser (the recoil laser height) with a finer step size and scanning for the visibility reduction. To maximize the effect, we also set the power of the recoil laser to the maximum of 17.04 W due to the estimate that the reduction effect increases with the laser power. We measured the visibility at the different recoil laser height, as plotted in Fig. 8.5 for 4 randomly chosen recoil laser positions D. Each data point here is the mean value estimated from several visibility scans with the standard deviations as the error bars. The change of the visibility maps the shape of the laser beam profile as expected for the Gaussian intensity distribution of the recoil laser. This is confirmed by fitting a Gaussian through the data points to determine the peak positions yielding maximal visibility reduction.
In Fig. 8.6 we confirm the linearity of the power dependence of the Eq. 8.9 by directly plotting $-\ln(R)$ against the recoil laser power from 0 to 17.05 W at all the 4 randomly chosen D. To trace the molecular beam, we approximated the

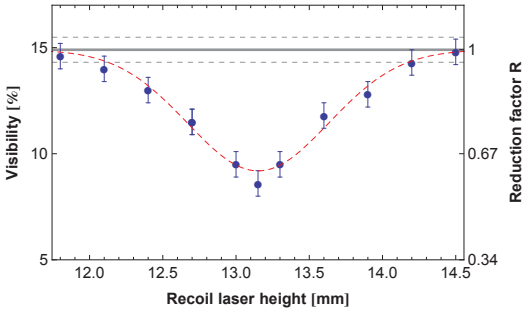

(a) Vis vs. the recoil laser height at $D =$ 35 mm

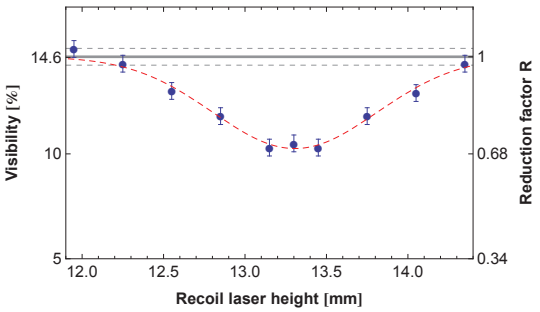

(b) Vis vs. the recoil laser height at $D =$ 40 mm

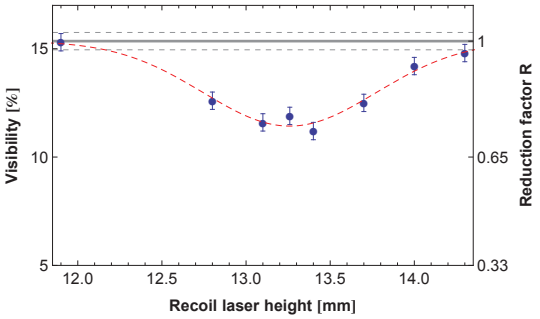

(c) Vis vs. the recoil laser height at $D =$ 45 mm

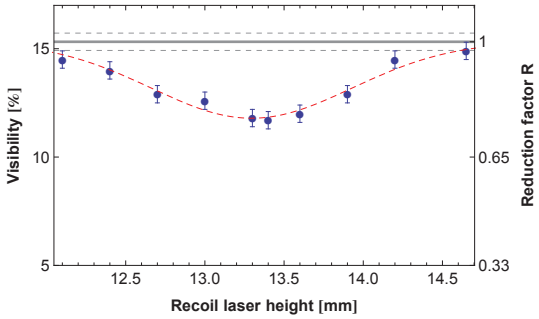

(d) Vis vs. the recoil laser height at $D =$ 54.5 mm

Figure 8.5: Visibility changes in dependence of the recoil laser height at 4 different recoil laser positions at the maximal recoil laser power. The blue points are the data points with the errors estimated from 10 visibility scans. The mean visibility in the absence of the recoil laser is indicated by the solid gray line around 15% with the error bar in dashed thin lines. Each distribution can be well approximated by a Gaussian distribution (red, dashed lines).

trajectory of the molecules with a mean velocity of 210 m/s within 2.5 cm to be linear. Fig. 8.7(a) shows the molecular trajectory by linear fitting through the data points of maximal visibility reduction at the 4 randomly chosen D in Fig. 8.5. Using the trajectory fit we measured the reduction factors along the molecular beam path while the recoil laser power was kept at 17.04 W for the maximal reduction effect. The complete measurement data of the reduction factor is plotted in Fig. 8.7(b) with respect to the recoil laser position D.

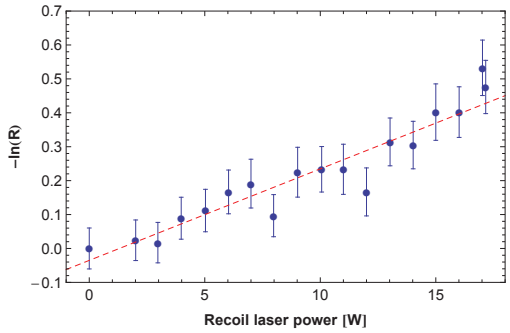

(a) R vs the recoil laser power at $D = 35$ mm

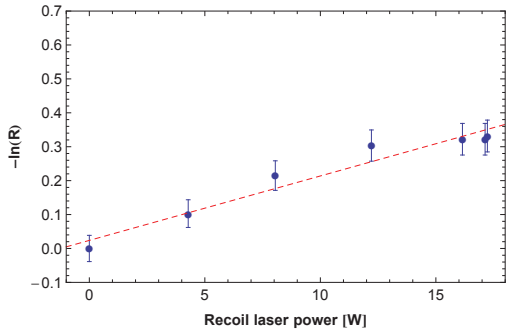

(b) R vs the recoil laser power at $D = 40$ mm

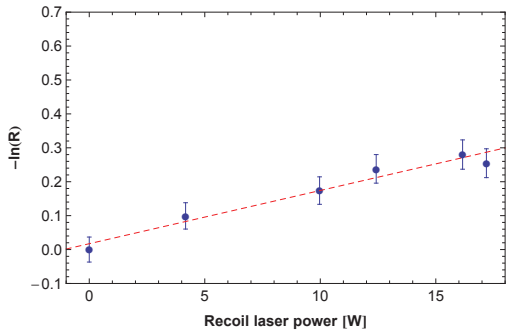

(c) R vs the recoil laser power at $D = 45$ mm

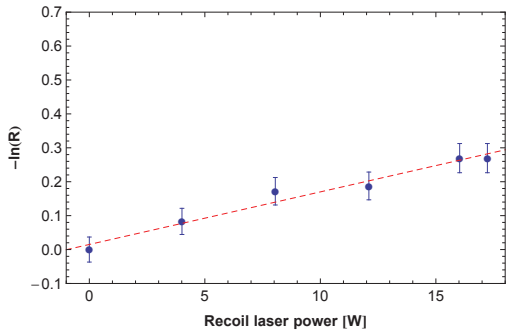

(d) R vs the recoil laser power at $D = 54.5$ mm

Figure 8.6: The reduction factor depends on the recoil laser power which is plotted in logarithmic scale. It seems to possess a linear relation according to Eq. 8.9 for each position. The linear fits are indicated by the dashed red lines. However a reliable absorption cross section can not be deduced from the varying gradients.

As mention in section 8.2.2, the importance of the influence of the C_{70} triplet states can be ruled out by varying the light grating power. If the effect of the triplet state is significant, a higher light grating power would cause a distortion in the typical visibility against light grating power plot because of the different optical polarizability of the excited C_{70}. Fig. 8.8 shows the visibility as a function of the laser grating power with and without the recoil laser, respectively in (a). The corresponding reduction factor (b) remains stable for different light grating powers from $1 - 6.5$ W which supports the argument that the excited C_{70} has no significant influence on the reduction in interference fringe contrast.

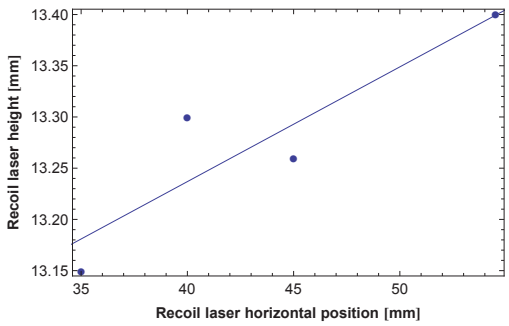

(a) Beam trajectory.

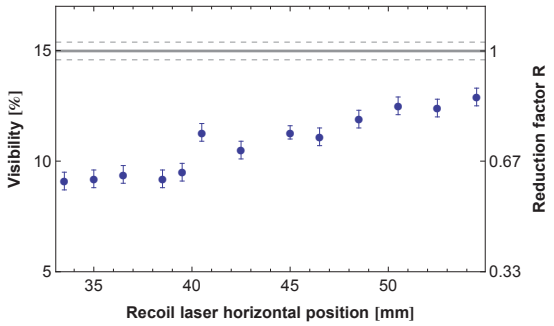

(b) Visibility vs the recoil laser position data collected along the molecular beam.

Figure 8.7: The molecular beam trajectory is approximated by using linear regression for a distance of 2 cm in (a). The change of the visibility in dependence of the recoil laser position is plotted in (b) within the accessible range at the maximal recoil laser power where the gray lines stand for the undisturbed interference contrast.

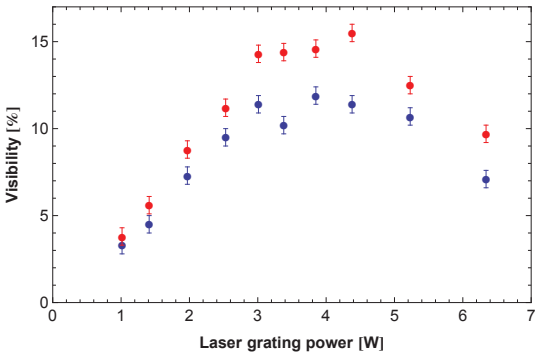

(a)

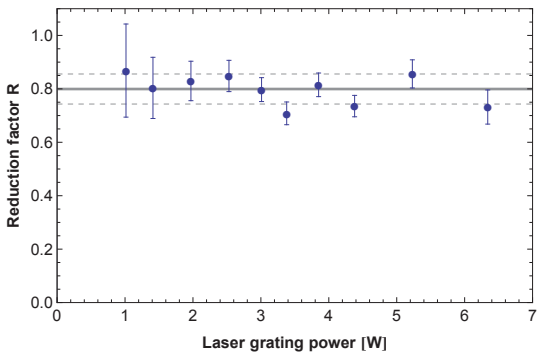

(b)

Figure 8.8: The visibility without the recoil laser is plotted as a function of the light grating power between $1 - 6.5$ W in red while blue data points are collected with the recoil laser. After conversion into the reduction factor (b) a clear constant value of $R = 0.80 \pm 0.06$ yields out where the recoil laser is positioned at $D = 4.85$ mm during the measurement.

The complete data analysis to determine the absorption cross section will be carried out in the next section.

8.3.2 Data analysis

An estimate of the absorption cross section can be already made from the gradient of Eq. 8.9. However, the accurate data analysis is based on fits using Eq. 8.11 upon the data in Fig. 8.7(b). This analysis is time consuming if a higher resolution is required. As discussed in the theory part, Eq. 8.9 is only valid for a fixed velocity v_0 at the first minimum at $D_{\min} = dmv_0\lambda_L/2h$ in the reduction factor in Fig. 8.3. For a more accurate estimate, the finite velocity spread needs to be taken into account.

According to section 8.2.1, we find the velocity distribution $P(v_z)$ in Eq. 8.11 can be well described by a Gaussian in time converted to velocity, $P_t(v_z)$. At the same time, we also consider the approximated Gaussian velocity distribution, denoted by $P_v(v_z)$, separately to see how it affects the final result. These distributions are given by

$$P_t(v_z) = \frac{1}{\sqrt{2\pi}\sigma_t} \exp\left(-\frac{(\frac{L}{v_z} - t_0)^2}{2\sigma_t^2}\right) \tag{8.16}$$

$$P_v(v_z) = \frac{1}{\sqrt{2\pi}\sigma_v} \exp\left(-\frac{(v_z - v_0)^2}{2\sigma_v^2}\right) \tag{8.17}$$

with a total length of $L = 1.74$ m, a mean flight time of $t_0 = 8.28 \pm 0.02$ ms corresponding to $v_0 = 210.3 \pm 0.7$m/s, $\sigma_t = 1.84 \pm 0.02$ ms and $\sigma_v = 38.4 \pm 0.05$ m/s, as shown in Fig. 8.4 respectively. The molecular beam width is narrowed down to 200 μm by the velocity slits. Since it is significant smaller than the recoil laser waist, it is reasonable to assume that n_0 is uniformly distributed within the molecular beam, i.e., the electric field intensity of the recoil laser is the same for all molecules. Hence, the additional exponential factor in Eq. 8.15 can be replaced by unity in our case.

A numerical integration in Eq. 8.11 is carried out for $1 \leq v_z \leq 1000$ with machinery precision. The absorption cross section σ_{abs} can be deduced from fitting Eq. 8.11 as the only fit parameter. Here, we minimize the χ^2 value for both velocity distributions in order to characterize the goodness of the fits where the error distribution of each measurement can be assumed to be Gaussian distributed. For

the one-parametric fit, we use the χ^2 function given by

$$\chi^2 = \sum_{i=1}^{N} \frac{(y_i - f(x_i))^2}{\sigma_{y_i}^2} \tag{8.18}$$

where $y_i(x_i)$ and σ_{y_i} are the measured values and errors, respectively, with x as the variable which corresponds to recoil laser position D. The running index i goes from 1 to N, the total number of the data points, and $f(x_i)$ is the value estimated from theoretical model Eq. 8.11.
The χ^2 values are calculated numerically for a list of σ_{abs} values from $2.0 - 2.2 \cdot 10^{-21} m^2$ for P_t and from $1.9 - 2.1 \cdot 10^{-21} m^2$ for P_v with a step size of $10^{-24} m^2$. Minima of χ^2_{min} at 3.91 and 3.76 are estimated for both distributions, respectively in Fig. 8.9. We take the 1σ uncertainty of the χ^2 by using $\chi^2 \to \chi^2 + 1$ [73]

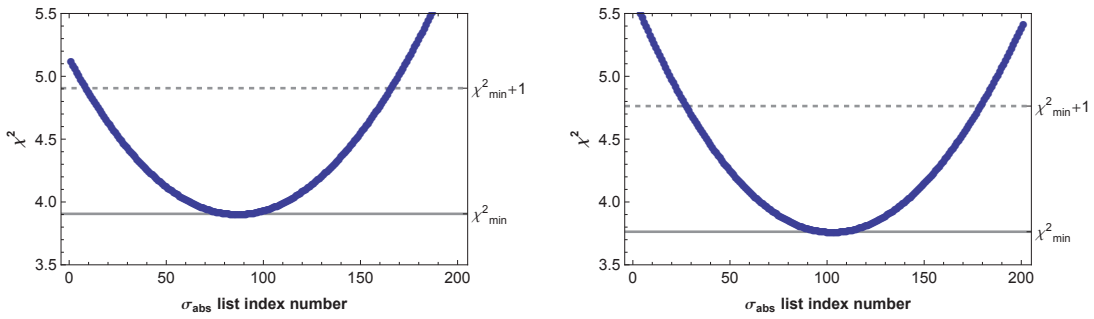

(a) χ^2 - optimization for P_t

(b) χ^2 - optimization for P_v

Figure 8.9: Numerical χ^2 optimization calculated by a list of 200 σ_{abs} values for P_t (a) and P_v (b), respectively. The solid lines indicate the minimum χ^2_{min}. The dashed lines indicate the uncertainty in χ^2 function by varying the parameter by 1σ.

to estimate the parameter errors being $0.08 \cdot 10^{-21} m^2$ for both cases and denote this as statistical error. This 4% error only comes from the χ^2 fit. A general error estimate requires also the contributions of other experimental parameters, such as t_0, σ_t, P_L and w_L[3]. For simplicity, we have varied all of these parameters to determine the worst case scenario which are described by the systematic error

[3]The error of the translation stage was neglected.

bars. The final values for the absorption absorption cross section at 532 nm are given by

$$\sigma_{\mathrm{abs}_t} = 2.04^{\pm 0.07_{\mathrm{sys}}}_{\pm 0.08_{\mathrm{stat}}} \cdot 10^{-21}\mathrm{m}^2 \tag{8.19}$$

$$\sigma_{\mathrm{abs}_v} = 2.00^{\pm 0.06_{\mathrm{sys}}}_{\pm 0.08_{\mathrm{stat}}} \cdot 10^{-21}\mathrm{m}^2 \tag{8.20}$$

respectively for P_t and P_v. These results are plotted with the measurement data and the fit functions in Fig. 8.3.2(a) and (b) where the errors of the fits are added in quadrature [74]. The goodness of the fit using P_t and P_v indicate for equally good fits in both cases. It appears that calculations with P_v will not make significant changes compared to the calculation using P_t. Despite all of those, the final results agree with each other perfectly and hence validate the approximation of the velocity distribution.
We conclude that the absorption cross section can be approximated by taken the data point locating the closest to D_{min} and find that the value to be $\sigma_{\mathrm{abs}} = 1.7 \cdot 10^{-21} m^2$ which is roughly 10% off from the value determined by the full analysis.

8.4 Measurement using β-carotene

The method of measuring the absolute absorption cross section offers promising application for studies of biomolecules. Due to the condition of precise knowledge of the vapour pressure in the common methods, the estimation of the absorption cross section is limited by a large uncertainty. In many cases, solvent analysis is employed to deduce the absorption cross section of complex molecules in gas phase [81, 86, 87]. We applied our method to measure the absolute absorption cross section of β-carotene with the recoil lasers at wavelengths of 405 nm and 445 nm according to the literature values for the relative absorption cross section in Ref. [84, 85, 88]. However, due to the strong solvent effect [82, 83, 84, 85, 86, 87] the predicted absorption lines might be narrowed in the absence of the Doppler broadening in vacuum and shifted therefore by many nanometres. Therefore, it was not possible for us to measure the absorption cross section using the same equipment. We plan spectroscopy using a tunable TiSa laser, see chapter 9.

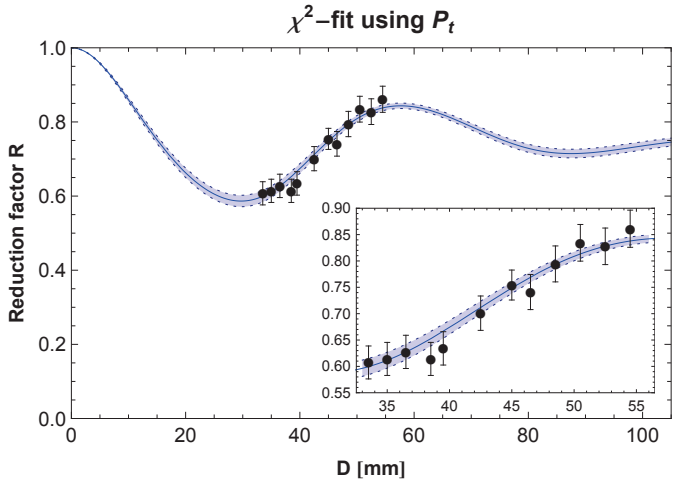

(a) χ^2 fit with P_t distribution

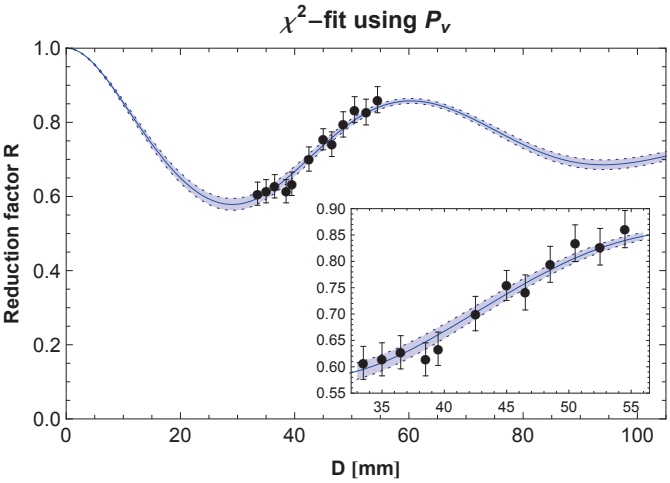

(b) χ^2 fit with P_v distribution

Figure 8.10: χ^2 fits with P_t and P_v distributions in (a) and (b), respectively: The solid line is the calculated value for absorption cross section while the dotted lines indicate the error estimated from systematic and statistic errors added in quadrature. The inserts give a closer look at the fitting function.

Chapter 9

Summary and Outlook

In this thesis, I have reviewed the fundamentals of the matter-wave interferometer in the Talbot-Lau design. This specific grating configuration measures the quantum interference effect in the nanometre scale and thus demonstrates the wave nature of massive objects without the coherence requirement on the source. However, the relaxation of the coherence requirement results in a high alignment precision and in the stability requirement of each components of the setup.
The difficulties in reliable interference scans are extensively shown in chapter 3 for setting up a TLI. We overcome the instability in positioning the third grating by manipulating the data in the data analysis. The high velocity selection is achieved by employing the time-of-flight measurement. Due to the finite width of chopper slits the time-of-flight signal needs to be averaged over the slit width which appears to decrease the interference contrast by 50% in a numerical simulation. Nevertheless, at two longitudinal positions for the third grating we suspect the occurrence of interference with the fringe contrasts of 7% and 9% around 160 m/s, respectively. Possible explanation might be due to the unstable and low molecular flux through the interferometer.
In order to eliminate any doubt, further data collection at these positions is recommended. A pseudo-random sequence of the chopper slits would increase the transmitted signal and also recover the averaging effect. A Michelson-Moore interferometer (MMI) can be used with the retro-reflected alignment laser light from the grating surface. By accessing the spacial intensity variation on the image screen

of the MMI, the grating vibration might be directly measured.
A comparison between the Talbot-Lau and Kapitza-Dirac-Talbot-Lau interferometers in chapter 5 highlights the advantage of the optical phase grating regarding the interference visibility measurement.
By using the KDTLI we have demonstrated a technique[64] to measure the absolute absorption cross section in chapter 8. The decoherence effect introduced by the recoil laser on the interference pattern reveals the absorption cross section of the molecules. Due to the finite velocity spread of the molecular beam, the velocity distribution has to be taken into account. We approximate the molecular density distribution by a Gaussian with respect in time-of-flight. By fitting, the absorption cross section can be estimated with an uncertainty of less than 4%. In addition, we find that the result using the approximated velocity distribution coincides with the one obtained by using the measured velocity distribution.
The demonstrated method is completely independent on the molecular beam density and can be applied to dilute gases. To obtain the absorption cross section for larger range of spectrum, a tunable laser is required. Due to the absence of the solvent effect of biomolecules in the gas phase, the absorption lines are narrowed and blue-shifted to the UV range.
Since molecular absorption cross section is strongly dependent on the temperature of the molecules [75, 76] we expect this dependence to be observed for C_{70} too. Therefore, the most straight forward way to test this behaviour is to vary the oven temperature and repeat the measurement in the nearest future. In addition, isomer-dependent absorption cross section can also be carried out using the mentioned technique. Molecules such as Retinal and Chlorophyll are isomerizable. By applying photo-induced isomerization via UV laser, the ratio between the different conformations of such molecules can be tuned by the laser before the interferometer. Specifically for the absorption cross section measurement, a variation in the reduction factor at fixed recoil laser position and power will be induced by a varying isomerization laser power, i.e. different isomer ratio within the molecular beam. It is appealing to predict that this can be used to extract the absorption cross section of different isomers.
Depending on the externally applied force field, different molecular properties can be measured. Similarly, polarizability can be analysed in the same manner by

replacing the recoil laser by the stark deflectrometry, as mentioned in Ref. [77]. TLI succeed in the static polarization measurement using stark deflector. Further improvement on the precision is planned. The calibration of the phase shift of the interference fringe determines the accuracy of polarizability measurement when an external electric field is applied to. Alkali metals with well known polarizability, such as Cs[78], Na[79], Li[80], can be used for this purpose for calibration. In addition, time-of-flight measurement combined with the random chopper would offer an even higher precision due to the continuum of velocity.
Thus, matter-wave interferometers in Talbot Lau design approve itself as a promising new technique in quantum enhanced metrology.

Part III

Appendix

Appendix A

QMS tune-file

This is a summery of the QMS tune-file at the University of Southampton.

Parameter	Value
Electron energy	-32 eV
Filament current	4.2 A
Ion region	40.0 V
Extractor lens	-19 V
Lens 1 and 3	-60 V
lens 2	1 V
Pole bias	9.28
Entrance lens	-18 V
Exit lens	-51 V
Multiplier	2000 V
Dynode	5000 V

The QMS tune-file optimization is done by maximizing the signal. The tuning is divided into three sections: the filament, the ion transmission and the ion detection.

For the filament, tuning determines the ionization efficiency by changing the electron energy and current flow in the filament. However, a decrease of the signal is observed for an electron energy below 45 eV. While the signal increases for higher current flow, the signal-to-noise ratio drops tremendously at the same time. To improve the ion transmission, a technique similar to 'walk-in' is used to optimize

all parameters. The exit lens appears to be insensitive regarding the optimization and the voltage of the lens 2 of the einzel lens system needs to be set around 0 voltage. A significant signal increase is achieve by lowering the pole bias with expense of the mass resolution which is justified by the purity of 99.5% for C_{60}. Finally, the signal can be enormously increased by rising the dynode and multiplier voltages resulting in a higher noise and dark counts.

Appendix B

Characterizing the scanning stage

To characterize the stability of our scanning stage we monitored the behaviour of the scanning motor during the two-minute data acquisition at an arbitrary transverse position of G3, as shown in Fig. B.1(a). A general shift in position is observed and accompanied with a fluctuation. Where the fluctuation comes from remains still unclear. Over the course of a 5-hour measurement the scanning motor was periodically sent to 10 subsequent transverse positions separated by 543 nm[1]. At each position the scanning motor was powered out for 2 minutes. We collected the behaviour of the scanning motor within the 2 minutes for all 120 transverse positions of G3 and plotted the evolution of the drift and the amplitude of the fluctuation as a function of the chronological number of measured transverse position in Fig. B.1(b) and (c), respectively. The drifts clearly decays and reaches a stable value around 10 nm after 3 hours (from the position number 70 in Fig. B.1(b)). The fluctuation in Fig. B.1(c) shows a periodic behaviour which is independent of the drift of the scanning stage. This periodicity can be explained by the movement sequence of the scanning motor. As expected, the fluctuation depends on the step size the scanning motor makes and is the largest between the last and the first transverse position of the 10 defined positions where the scanning motor is moved by 5430 nm to the opposite direction. For all other positions with 543 nm separation the fluctuation relaxes consistently to 3.5 nm due to the smaller motor steps.

[1]This step size corresponds to a step size of 29 nm with two full grating periods.

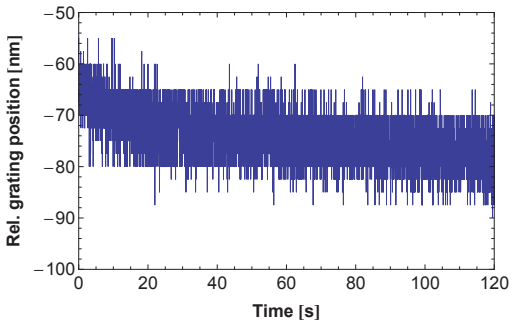

(a) 20 nm drift behaviour of the scanning stage within 120 s

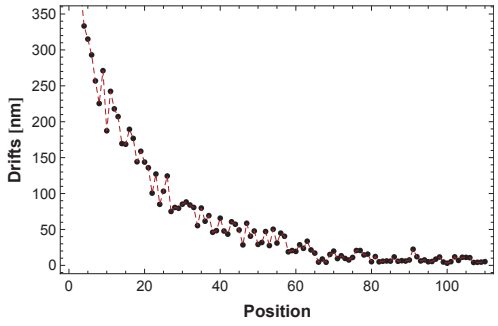

(b) Evolution of the scanning stage drift over 5 hours

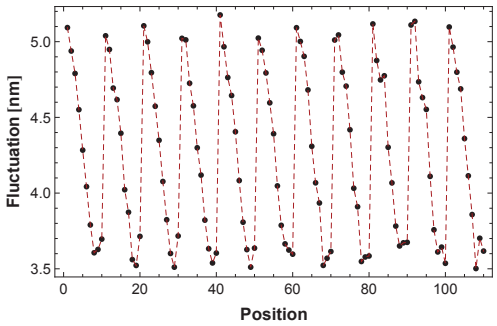

(c) Evolution of the fluctuation over 5 hours

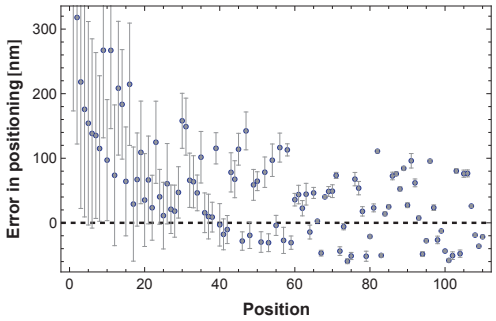

(d) Errors in positioning plotted with the drift as error bars.

Figure B.1: Data plotted here are collected on 19.07.2013 without SERVO and chosen for demonstration.

In addition, the scanning stage also shows an error in positioning. Fig. B.1(d) indicates the evolution of this error with respect to the chronological number of measured transverse position of G3. Here, we took the mean value of the drift data to characterize the error in positioning and used the drift for the error bars. A general decay is clearly visible whereas the positions showing a drift of less than 10 nm start from the position number 70. Since only data collected at these positions are useful in the data analysis, one needs to take these nearly randomly distributed errors in positioning into account for position correction, for more information see chapter 4.2. Moreover, we tested the "SERVO" feature of the scanning stage. In this test the scanning motor is set into a feedback loop for position correction during the two-minute data acquisition at each transverse

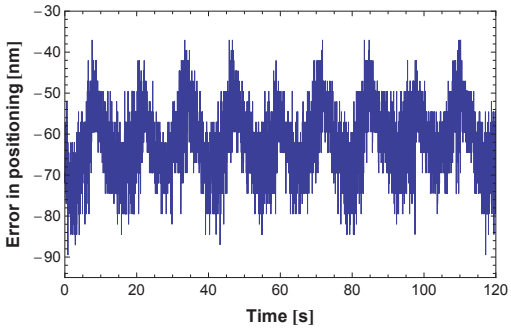

(a) Drift of the scanning stage in 120 s

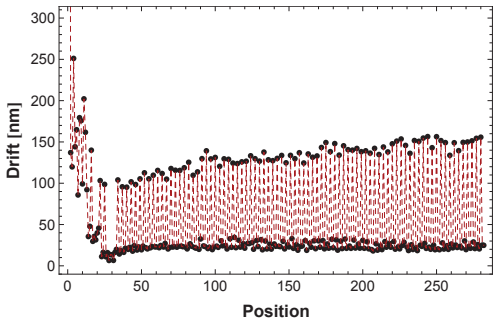

(b) Evolution of the scanning stage drift over 14 hours

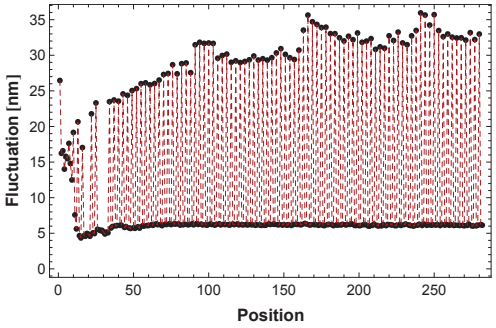

(c) Standard deviation of the fluctuation over 14 hours

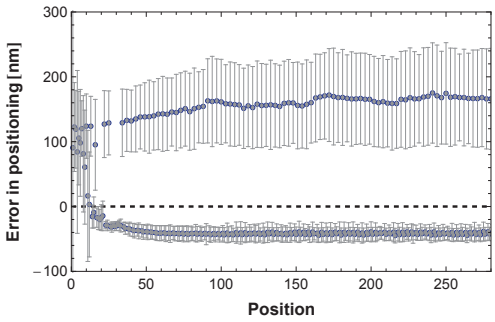

(d) Error of positioning the scanning stage

Figure B.2: Data plotted here are recorded on 25.04.2013 with SERVO and analysed in the same manner as in Fig. B.1.

position of G3 while the motor is powered out in the previous test. Fig. B.2(a) shows a more stable behaviour during the 2 minutes at an arbitrary transverse position of G3. The oscillation of the drift indicates the position correction due to the feedback loop but the fluctuation remains. For a 14-hour measurement similar parameters were chosen. Here, we sent the scanning motor periodically to 3 given positions separated by 335 nm[2]. In total, the drifts and oscillations of 282 positions are plotted in Fig. B.2(b) and (c). A significant large oscillation of the drift and the fluctuation are observable when the scanning motor moved a large step of 670 nm. This is illustrated by the data points between 100 and 150

[2]This corresponds to a separation of 78 nm wit one grating period.

nm in Fig. B.2(b) and data points between 20 and 35 nm in Fig. B.2(c). All data points with smaller step size show a stable and well controlled behaviour. Similar pattern was measured for the error in positioning, shown in Fig. B.2(d). These errors seem to be well controlled for all positions. Transverse positions after a large movement of 670 nm show an error in positioning around +150 nm and positions after a smaller movement has a defined error around -20 nm. Despite the repeatability in positioning, the drift appears to be larger than the case when the "SERVO" feature was switched off. Therefore, the measurement concept with a smaller drift is more feasible.

Appendix C

Consideration of the Fourier coefficients for the reduction factor

In this section, we will calculate the Fourier components for the particle density distribution and show that the visibility can be well approximated by the first Fourier component. Also the velocity dependence of the Fourier components will be compared.
According to [71], the Wigner function of the molecular transversal motion state w_{G3} in front of the third grating is given by the Fourier series

$$w_{G3}(x) = \sum_{l\in\mathbb{Z}} w_l \left(l\frac{L}{L_T}\right) \exp\left(2\pi i l\frac{x}{d}\right) = \sum_{l\in\mathbb{Z}} A_l^* B_{2l} \left(l\frac{L}{L_T}\right) \exp\left(2\pi i l\frac{x}{d}\right) \tag{C.1}$$

where

$$A_l = \frac{1}{d}\int_{-d/2}^{d/2} T(x) e^{-2\pi i l x/d} dx \tag{C.2}$$

and

$$B_m(\xi) = \exp\left(-\zeta_{\text{abs}}(\xi)\right) \left(\frac{\zeta_{\text{coh}}(\xi) - \zeta_{\text{abs}}(\xi)}{\zeta_{\text{coh}}(\xi) + \zeta_{\text{abs}}(\xi)}\right)^{m/2} \tag{C.3}$$

$$\times J_m\left(-\text{sgn}\left(\zeta_{\text{coh}}(\xi) + \zeta_{\text{abs}}(\xi)\right) \sqrt{\zeta_{\text{coh}}^2(\xi) - \zeta_{\text{abs}}^2(\xi)}\right). \tag{C.4}$$

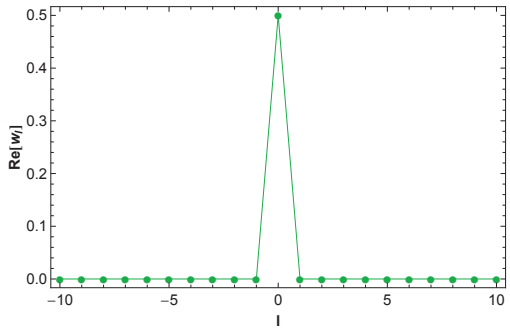

(a) Real part of the Fourier coefficients w_l in dependence of the Fourier order l

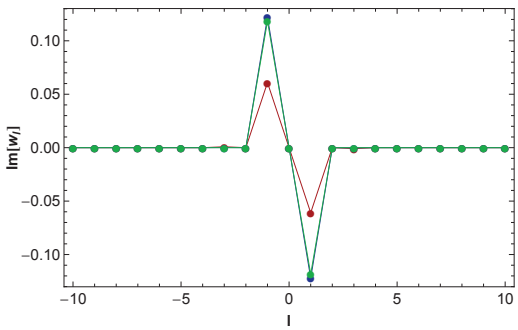

(b) Imaginary part of the Fourier coefficients w_l in dependence of the Fourier order l

Figure C.1: w_l as a function of the order of the Fourier coefficient l for 170 m/s (red), 210 m/s (blue) and 260 m/s (green). The real part of w_l is pictured in (a) and the imaginary part in (b).

For the simulation, we use C_{70} in the KDTLI with three gratings with a grating period of 266 nm and an open fraction of 0.5. The waist of the light grating laser is set to 1.2 mm and the power to 11 W. The real and imaginary parts of w_l are plotted in Fig. C.1 for three velocities of particles 170 m/s (red), 210 m/s (blue, not visible) and 260 m/s (green) whereas the real part remains the same and the imaginary part varies slightly. It can be clearly seen that only components with $l = \pm 1$ contribute to Eq. C.1 beside the zero-th order of coefficient.

Let's take a closer look at the components with $l = \pm 1$ in dependence of a velocity between 170 m/s and 260 m/s, corresponding to the velocity class in our oven. It turns out that $w_0 = 1/2$ is constant for all velocities and only the imaginary parts of w_l exist for odd values of l. Fig. C.2 shows the simulated values for $\mathrm{Im}[w_{l=\pm1,\pm3,\pm5}]$ in dependence of velocity. This proves also the dominance of the first Fourier component which is of a factor 100 greater than the next order.

Formally, the visibility is defined by $\mathrm{Vis} = \frac{S_{\max}-S_{\min}}{S_{\max}+S_{\min}}$ where the signal function after an identical grating mask is given by

$$S(x) = \sum_{l\in\mathbb{Z}} s_l \exp\left(2\pi i l x/d\right) = \sum_{l\in\mathbb{Z}} (A_l^*)^2 B_{2l}\left(l\frac{L}{L_T}\right)\exp\left(2\pi i l x/d\right) \tag{C.5}$$

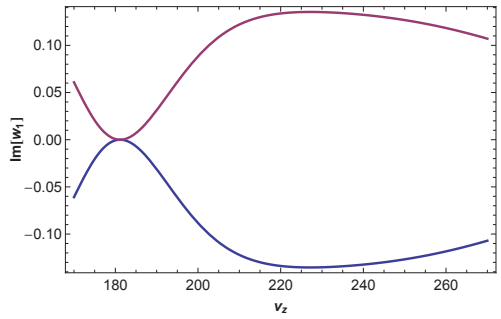

(a) Velocity dependence of the imaginary part of the first order the Fourier coefficient w_1

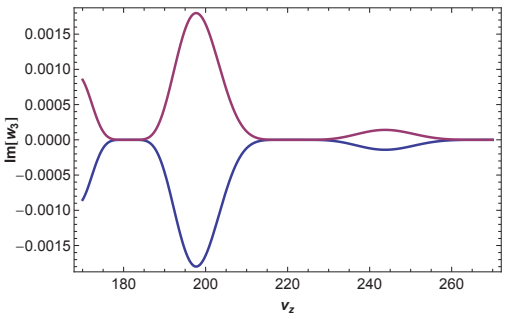

(b) Velocity dependence of the imaginary part of the third order the Fourier coefficient w_3

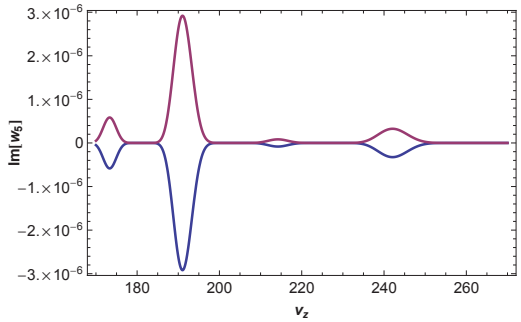

(c) Velocity dependence of the imaginary part of the fifth order the Fourier coefficient w_5

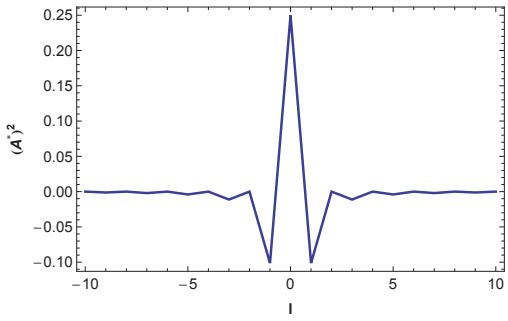

(d) Real part of $(A_l^*)^2$ in dependence of the order of the Fourier coefficient l

Figure C.2: Velocity dependence of the imaginary parts of ±1st (a), ±3rd (b) and ±5-th (c) orders of the Fourier components. As we can see, the $+l$ (blue) and $-l$ (red) components have opponent signs. However, the components vanish for even values of l because of A_l and the real part is zero for all $l \neq 0$. (d) shows the evolution of $(A_l^*)^2$ as a function of l.

$S_{\max}$ and $S_{\min}$ are defined for $x = 0$ and $x = \pm d/2$ respectively which yield global maxima and minima. From the evolution of $(A_l^*)^2$ plotted in Fig. C.2, we see that $(A_l^*)^2$ behaves symmetrically and vanishes for all even values of l in our case. From this we conclude the condition $s_l = s_{-l}$ and allow ourselves to approximate the signal function with the most dominant coefficient s_1 by $S(x) \approx s_0 + 2s_1 \cos(2\pi x/d)$. Taking those into account, we receive a rearranged definition

for experimental accessible visibility

$$\text{Vis} = \left| \frac{\sum_{l=1}^{\infty} s_{2l-1}}{\frac{s_0}{2} + \sum_{l=1}^{\infty} s_{2l}} \right| \approx \left| \frac{2s_1}{s_0} \right|. \tag{C.6}$$

Appendix D

Independence of the positioning of the recoil laser before and after the phase grating

The experimental setup differs from the theoretical model in the position of the recoil laser. The fact that positioning the recoil laser before or after the optical phase grating in Fig. D.1 may cause controversy in the theoretical result. Here, we want to show that the result is independent of the position of the recoil laser in a symmetric interferometer. We use the Wigner function description in [70] and [71] to analyse the density pattern of the molecular state during the propagation through the KDTLI and compare the final density patterns of both mentioned cases. According to K. Hornberger [70], the particle's positional density $w(\mathbf{r})$ can be found by integrating with respect to the momentum $\mathbf{p}$:

$$w(\mathbf{r}) = \int w(\mathbf{r}, \mathbf{p}) d\mathbf{p} \tag{D.1}$$

Free propagation over a distance of L would cause a change in the initial Wigner function $w_i(\mathbf{r}, \mathbf{p})$ as follows:

$$w_L(\mathbf{r}, \mathbf{p}) = w_i \left(r - \frac{L}{p_z} \mathbf{p}, \mathbf{p} \right) \tag{D.2}$$

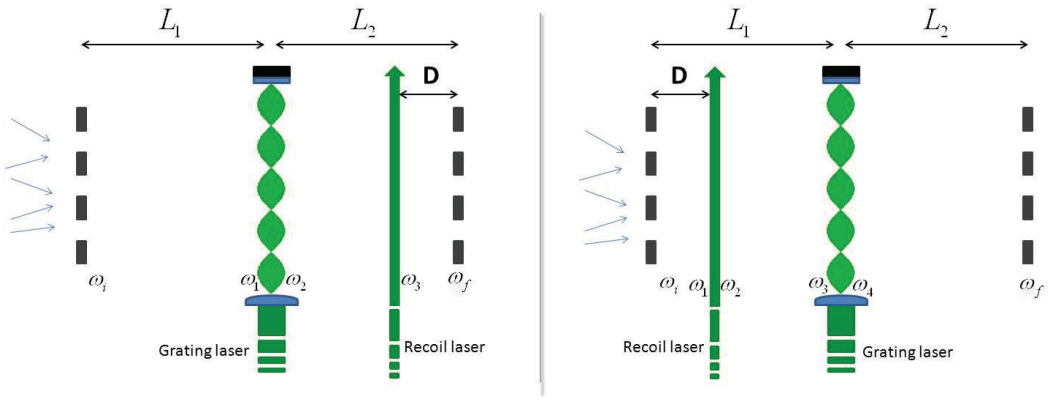

Figure D.1: The position of the recoil is placed between the light grating and the third grating in the left inset and is located between the first and the second grating in the right inset.

and the passage though an optical phase grating can be described by this convolution:

$$w_g(\mathbf{r},\mathbf{p}) = \int d\mathbf{q} T_{\text{coh}}(\mathbf{r},\mathbf{q}) w_i(\mathbf{r},\mathbf{p}-\mathbf{q}) \tag{D.3}$$

where T_{coh} is the coherently transforming convolution kernel under the simplification of an ideal phase grating. For the sake of the proof, we set the photon absorption cross section within the optical phase grating to be vanishing $\sigma_{\text{abs}_{\text{op}}} = 0$. We can further simplify the situation by replacing the Poisson statistics of the recoil laser beam by unity and just take single photon absorption into account. The Wigner function after the recoil laser will evolve into:

$$w_{\text{recoil}}(\mathbf{r},\mathbf{p}) = w_i(\mathbf{r},\mathbf{p}-\mathbf{p}_L) \tag{D.4}$$

where $\mathbf{p}_L$ is the recoil laser photon momentum.
Using the calculations above, we need to show that the final Wigner functions w_f are equal in both mentioned cases and are the same as the shifted distribution of the undeflected Wigner function w_0:

$$w_f(\mathbf{r}) = w_0(\mathbf{r}-s) \tag{D.5}$$

s is given by the recoil photon induced spatial shift $s = \frac{p_L}{p_z} D = \frac{\lambda_{\mathrm{dB}}}{\lambda_L} D$ where λ_{dB} and λ_L are the de Broglie wavelength of the particle and the recoil laser wavelength, respectively. w_0 is then given by

$$w_0(\mathbf{r} - s, \mathbf{p}) = \int d\mathbf{q} T_{\mathrm{coh}} \left(\mathbf{r} - \frac{L_2}{p_z}\mathbf{p}, \mathbf{q} \right) \left| t \left(\mathbf{r} - \frac{L_1 + L_2}{p_z}\mathbf{p} + \frac{L_1}{p_z}\mathbf{q} \right) \right|^2 \tag{D.6}$$

as the expected results where $t(\mathbf{r}, \mathbf{p})$ is the transmission function of the grating.

D.1 Recoil laser after the optical phase grating

For simplicity, we choose a monochromatic wave and set the Wigner function right after the first grating to be:

$$w_i(\mathbf{r}, \mathbf{p}) = |t(\mathbf{r})|^2$$

and the free propagation over the distance L_1 results in:

$$w_1(\mathbf{r}, \mathbf{p}) = \left| t \left(\mathbf{r} - \frac{L_1}{p_z}\mathbf{p} \right) \right|^2$$

After the optical phase grating, we receive:

$$w_2(\mathbf{r}, \mathbf{p}) = \int d\mathbf{q} T_{\mathrm{coh}}(\mathbf{r}, \mathbf{q}) \left| t \left(\mathbf{r} - \frac{L_1}{p_z}(\mathbf{p} - \mathbf{q} \right) \right|^2$$

The Wigner function evolves into

$$w_3(\mathbf{r}, \mathbf{p}) = \int d\mathbf{q} T_{\mathrm{coh}} \left(\mathbf{r} - \frac{L_2 - D}{p_z}\mathbf{p}, \mathbf{q} \right) \left| t \left(\mathbf{r} - \frac{L_1 + L_2 - D}{p_z}\mathbf{p} + \frac{L_1}{p_z}\mathbf{q} \right) \right|^2$$

over the distance $L_2 - D$ before the recoil photon momentum transfer. The recoil laser will change w_3 to:

$$w_4(\mathbf{r}, \mathbf{p}) = \int d\mathbf{q} T_{\mathrm{coh}} \left(\mathbf{r} - \frac{L_2 - D}{p_z}(\mathbf{p} - \mathbf{p}_L), \mathbf{q} \right)$$

$$\left| t \left(\mathbf{r} - \frac{L_1 + L_2 - D}{p_z}(\mathbf{p} - \mathbf{p}_L) + \frac{L_1}{p_z}\mathbf{q} \right) \right|^2$$

The final distribution in front of the scanning grating mask is:

$$w_f(\mathbf{r},\mathbf{p}) = \int d\mathbf{q} T_{\text{coh}} \left(\mathbf{r} - \frac{L_2}{p_z}\mathbf{p} + \frac{L_2 - D}{p_z}\mathbf{p}_L, \mathbf{q} \right)$$

$$\left| t\left(\mathbf{r} - \frac{L_1 + L_2}{p_z}\mathbf{p} + \frac{L_1 + L_2 - D}{p_z}\mathbf{p}_L + \frac{L_1}{p_z}\mathbf{q} \right) \right|^2$$

Since we are only interested in the spatial distribution Eq. D.1, we choose the momentum transformation $\mathbf{p} \to \mathbf{p} + \mathbf{p}_L$. For symmetric interferometer $L_1 = L_2$, we ultimately have:

$$w_f(\mathbf{r},\mathbf{p}) = \int d\mathbf{q} T_{\text{coh}} \left(\mathbf{r} - \frac{L}{p_z}\mathbf{p} - \underbrace{\frac{D}{p_z}\mathbf{p}_L}_{s}, \mathbf{q} \right) \left| t\left(\mathbf{r} - \frac{2L}{p_z}\mathbf{p} + \frac{L}{p_z}\mathbf{q} - \underbrace{\frac{D}{p_z}\mathbf{p}_L}_{s} \right) \right|^2 \tag{D.7}$$

Eq. D.7 and Eq. D.6 clearly fulfil the condition D.5.

D.2 Recoil laser before the optical phase grating

We repeat the same procedure by staring with:

$$w_i(\mathbf{r},\mathbf{p}) = |t(\mathbf{r})|^2$$

At the distance D from the first grating

$$w_1(\mathbf{r},\mathbf{p}) = \left| t\left(\mathbf{r} - \frac{D}{p_z}\mathbf{p} \right) \right|^2,$$

the recoil laser comes into play and we get

$$w_2(\mathbf{r},\mathbf{p}) = \left| t\left(\mathbf{r} - \frac{D}{p_z}(\mathbf{p} - \mathbf{p}_L) \right) \right|^2.$$

The Wigner function propagates $L_1 - D$ towards the optical phase grating and becomes

$$w_3(\mathbf{r},\mathbf{p}) = \left| t\left(\mathbf{r} - \frac{L_1}{p_z}\mathbf{p} + \frac{D}{p_z}\mathbf{p}_L\right)\right|^2 .$$

After the second grating the Wigner function evolves to:

$$w_4(\mathbf{r},\mathbf{p}) = \int d\mathbf{q} T_{\mathrm{coh}}\left(\mathbf{r},\mathbf{q}\right)\left| t(\mathbf{r} - \frac{L_1}{p_z}(\mathbf{p}-\mathbf{q}) + \frac{D}{p_z}\mathbf{p}_L\right)\right|^2 .$$

And finally after the L_2 propagation we have

$$w_f(\mathbf{r},\mathbf{p}) = \int d\mathbf{q} T_{\mathrm{coh}}\left(\mathbf{r} - \frac{L_2}{p_z}\mathbf{p},\mathbf{q}\right)\left| t\left(\mathbf{r} - \frac{L_1+L_2}{p_z}\mathbf{p} + \frac{L_1}{p_z}\mathbf{q} + \frac{D}{p_z}\mathbf{p}_L\right)\right|^2 .$$

Similar to the previous case, we choose the transformation $\mathbf{p} \to \mathbf{p} + \frac{D}{L_1}\mathbf{p}_L$ and acquire the symmetry $L_1 = L_2$:

$$w_f(\mathbf{r},\mathbf{p}) = \int d\mathbf{q} T_{\mathrm{coh}}\left(\mathbf{r} - \frac{L}{p_z}\mathbf{p} - \underbrace{\frac{D}{p_z}\mathbf{p}_L}_{s},\mathbf{q}\right)\left| t\left(\mathbf{r} - \frac{2L}{p_z}\mathbf{p} + \frac{L}{p_z}\mathbf{q} - \underbrace{\frac{D}{p_z}\mathbf{p}_L}_{s}\right)\right|^2 \tag{D.8}$$

which is equal to Eq. D.7 and fulfils the condition Eq. D.5.

Acknowledgements

Finally, I would like to use this opportunity to dedicate my deepest thanks to several people who have been a huge support during this time.
First of all, I sincerely thank Markus Arndt for providing me the opportunity not only to continue my thesis in Vienna but also to work on such an exciting experiment in a vivid and dynamic group. Without his guidance the experiment would not be developed to this stage. Also I honestly appreciate his valuable support and helps even on the experiment at the University of Southampton.
Secondly, a special thank goes to Hendrik Ulbricht. I am grateful for the opportunity to work on the Talbot-Lau interferometer in his group straight away. Without his endless motivation, experimental expertise and guidance, it would not be possible for me to gain such great amount of practical experiences in molecular quantum optics.
A lot thanks to my co-workers/co-supervisors Joseph Cotter and Sandra Eibenberger. I thank Joseph for all of the valuable advises in the lab and in the data analysis and also for proof reading this thesis. At the same time, I thank Sandra for her support on the TLI and the KDTLI. It was pleasant to work with them whom I can always count on.
The course of the master's study would not be possible without the support of my family, in particular my dad, Zhao Cheng, for his patience and generous support in every area of my life. I would also like to express my honest gratitude to my old friends (Ugur Sezer, Christoph Klaushofer, ...) and also the colleagues in the groups of Markus Arndt and Hendrik Ulbricht.
Of course, a huge amount of thank goes to my beloved Xenia Gschnitzer for her generous patience and encouragement.

Bibliography

[1] L. de Broglie, *Waves and quanta*, Nature 112, 540 (1923)

[2] C. Davisson, L. H. Germer, *Diffraction of Electrons by a Crystal of Nickel*, Phys. Rev. 30(6), 705740 (1927)

[3] G. P. Thomson, *The Diffraction of Cathode Rays by Thin Films of Platinum*, Nature 120, 802802 (1927)

[4] I. Estermann, O. Stern, *Beugung von Molekularstrahlen*, Zeitschrift für Physik A: Hadrons and Nuclei, 61(1), 95125 (1930)

[5] A. Zeilinger, R. Gähler, C. G. Shull, W. Treimer, W. Mampe, *Single- and double-slit diffraction of neutrons*, Rev. Mod. Phys. 60, 1067 (1988)

[6] O. Carnal, J. Mlynek, *Youngs double-slit experiment with atoms: A simple atom interferometer*, Phys. Rev. Lett.66(21), 26892692 (1991)

[7] D. W. Keith, C. R. Ekstrom, Q. A. Turchette, D. E. Pritchard, *An interferometer for atoms*, Phys. Rev. Lett. 66(21):26932696 (1991)

[8] F. Shimizu, K. Shimizu, H. Takuma, *Double-slit interference with ultracold metastable neon atoms*, Phys. Rev. A 46, R17(R) (1992)

[9] Ch.J. Bord, N. Courtier, F. du Burck, A.N. Goncharov, M. Gorlicki, *Molecular interferometry experiments*, Phys. Lett. A 188, 187 (1994)

[10] C. Adams, M. Sigel, J. Mlynek, *Atom optics*, Phys. Rep. 240(3), 143210 (1994)

[11] C. Borde, N. Courtier, F. du Burck, A. Goncharov, M. Gorlicki, *Molecular interferometry experiments*, Phys. Lett. A 188(3), 187197 (1994)

[12] J. F. Clauser, S. Li, *Talbot-vonLau atom interferometry with cold slow potassium*, Phys. Rev. A 49, R2213 (1994)

[13] M. S. Chapman, C. R. Ekstrom, T. D. Hammond, R. A. Rubenstein, J. Schmiedmayer, S. Wehinger, D. E. Pritchard, *Optics and Interferometry with Na_2 Molecules*, Phys. Rev. Lett. 74(24), 47834786 (1995)

[14] M. S. Chapman, T. D. Hammond, A. Lenef, J. Schmiedmayer, R. A. Rubenstein, E. Smith, D. E. Pritchard, *Photon Scattering from Atoms in an Atom Interferometer: Coherence Lost and Regained*, Phys. Rev. Lett. 75, 3783 (1995)

[15] K. Hornberger, S. Gerlich, P. Haslinger, S. Nimmrichter, M. Arndt, *Colloquium: Quantum interference of clusters and molecules*, Rev. Mod. Phys. 84, 157 (2012)

[16] L. Hackermüller, K. Hornberger, B. Brezger, A. Zeilinger, M. Arndt, *Decoherence in a Talbot Lau interferometer: the influence of molecular scattering*, Appl. Phys. B 77, 781 (2003)

[17] M. Arndt, K. Hornberger, A. Zeilinger, *Probing the limits of the quantum world*, Physics World 18, 35 (2005)

[18] L. Hackermüller, K. Hornberger, S. Gerlich, M. Gring, H. Ulbricht, M. Arndt, *Optical polarizabilities of large molecules measured in near-field interferometry*, Appl. Phys. B 89, 469 (2007)

[19] S. Nimmrichter, *Macroscopic Matter-wave Interferometry*, Ph.D thesis (2013)

[20] H. F. Talbot, *Facts relating to optical science*, Philos. Mag., 9, 401 (1836)

[21] W. B. Case, M. Tomandl, S. Deachapunya, M. Arndt, *Realization of Optical Carpets in the Talbot and Lau Configurations*, Optics Express, 17 20966 (2009)

[22] J. Jahns, A. W. Lohnmann, *The lau effect (a diffraction experiment with incoherent illumination)*, Opt. Comm. Vol. 28, 263 (1979)

[23] E. Lau, *Beugungserscheinungen an Doppelrastern*, Ann. Physik 6, Bd 2 (1940)

[24] M. Born, E. Wolf, *Principles of Optics: Electromagnetic Theory of Propagation, Interference and Diraction of Light*, Cambridge University Press (1999)

[25] P. L. Kapitza, P. A. M. Dirac, *The reflection of electrons from standing light waves*, Proc Cambridge Phil Soc 29, 297 (1933)

[26] P. Meystre, *Atom Optics*, Springer (2001)

[27] H. Batelaan, *The Kapitza-Dirac effect*, Contemporary Physics 41, 369 (2000)

[28] O. Nairz, et. al., *Diffraction of complex molecules by structures made of light*, Phys. Rev. Lett., 87, 160401 (2001)

[29] B. Brezger, et. al., *Concepts for near-field interferometers with large molecules*, J. Opt. B: Quantum Semiclass. Opt. 5, 82 (2003)

[30] K. Hornberger, et. al., *Theory of decoherence in a matter wave Talbot-Lau interferometer*, Phys. Rev. A 70, 053608 (2004)

[31] O. Stern, *Eine direkte Messung der thermischen Molekulargesehwindigkeit*, Z. Phys. 2, 49 (1920)

[32] R. E. Grisenti, et. al., *Determination of Atom-Surface van der Waals Potentials from Transmission-Grating Diffraction Intensities*, Phys. Rev. Lett. 83, 1755 (1995)

[33] H. Casimir, D. Polder, *The Influence of Retardation on the London-van der Waals Forces*, Phys. Rev. 73, 360 (1948)

[34] O. Nairz, B. Brezger, M. Arndt, A. Zeilinger, *Diffraction of Complex Molecules by Structures Made of Light*, Phys. Rev. Lett. 87, 160401 (2001)

[35] R. Brühl, R. Guardiola, A. Kalinin, O. Kornilov, J. Navarro, T. Savas, J. P. Toennies, *Diffraction of Neutral Helium Clusters: Evidence for "Magic Numbers"*, Phys. Rev. Lett. 92, 185301 (2004)

[36] Ch. Lisdat, M. Frank, H. Knöckel, M.-L. Almazor, E. Tiemann, *Realization of a Ramsey-Bord matter wave interferometer on the molecule*, Eur. Phys. J. D 12, 235 (2000)

[37] T. Reisinger, A. A. Patel, H. Reingruber, K. Fladischer, W. E. Ernst, G. Bracco, H. I. Smith, B. Holst, *Poissons spot with molecules*, Phys. Rev. A 79, 053823 (2009)

[38] M. Arndt, O. Nairz, J. Voss-Andreae, C. Keller, G. van der Zouw, A. Zeilinger, *Wave-particle duality of C60 molecules* , Nature 401, 680-682 (1999)

[39] B. Brezger, L. Hackermüller, S. Uttenthaler, J. Petschinka, M. Arndt, A. Zeilinger, *Matter-Wave Interferometer for Large Molecules*, Phys. Rev. Lett. Vol. 88, 100404-1-4 (2002)

[40] L. Hackermüller, S. Uttenthaler, K. Hornberger, E. Reiger, B. Brezger, A. Zeilinger, M. Arndt, *The wave nature of biomolecules and fluorofullerenes*, Phys. Rev. Lett. Vol. 91, 090408-1-4 (2003)

[41] S. Gerlich, et. al., *A Kapitza-Dirac-Talbot-Lau interferometer for highly polarizable molecules*, Nature Physics 3, 711 - 715 (2007)

[42] S. Gerlich, M. Gring, H. Ulbricht, K. Hornberger, J. Tüxen, M. Mayor, M. Arndt, *Matter-Wave Metrology as a Complementary Tool for Mass Spectrometry*, Angew. Chem. Int. Ed. 47, 6195619 (2008)

[43] S. Eibenberger, S. Gerlich, M. Arndt, M. Mayor, J. Tüxen, *Matter-wave interference with particles selected from a molecular library with masses exceeding 10 000 amu*, Phys.Chem. Chem. Phys. 15, 14696 (2013)

[44] S. Eibenberger, X. Cheng, J. P. Cotter, M. Arndt, *Absolute absorption cross sections from photon recoil in a matter-wave interferometer*, Phys. Rev. Lett. 112, 250402 (2014)

[45] M. S. Dresselhaus, G. Dresselhaus, P.C. Eklund, *Science of Fullerenes and Carbon Nanotubes*, Elsevier Science (1996)

[46] *Axial Molecular Beam Ionizer User Manual*, Extrel, CMS, L.P. (2004)

[47] R. E. March, *Quadrupole ion traps*, Mass Spec. Rev. 28, 961-989 (2009)

[48] S. Nimmrichter, K. Hornberger, *Theory of near-field matter-wave interference beyond the eikonal approximation*, Phys. Rev. A 78, 023612 (2008)

[49] R. Mitzner, E. Campbell, *Optical emission studies of laser desorbed C60*, J. Chem. Phys. 103, 2445 (1995)

[50] L. Hackermüller, K. Hornberger, B. Brezger, A. Zeilinger, M. Arndt, *Decoherence of matter waves by thermal emission of radiation*, Nature, Vol. 427, 711(2004)

[51] K. Yase, Y. Takahashi, N. Ara-Kato, A. Kawazu, *Evaporation rate and saturated vapor pressure of functional organic materials*, Jpn. J. Appl. Phys. 43, 636 (1995)

[52] T. A. Savas, et. al., 38th International symposium on electron, ion, and photon beams, Vol 13, p. 27322735(1995)

[53] C. Szewc, *Molecule Interference in the Near-Field Talbot Regime*, Ph.D. Thesis, University of Southampton (2012)

[54] L. Mairhofer, *Deflectometry in a Kapitza-Dirac-Talbot-Lau interferometer for matter waves*, Master's thesis, University of Vienna (2013)

[55] G. Scoles, *Atomic and molecula rbeam methods: Volume 1.*, Oxford University Press (1988)

[56] K. Hornberger, S. Uttenthaler, B. Brezger, L. Hackermüller, M. Arndt, A. Zeilinger, *Collisional Decoherence Observed in Matter Wave Interferometry*, Phys. Rev. Lett. 90, 160401 (2003)

[57] A. Stibor, K. Hornberger, L. Hackermüller, A. Zeilinger, M. Arndt, *Talbot-Lau interferometry with fullerenes: Sensitivity to inertial forces and vibrational dephasing*, Laser Physics, 15, 10-17 (2005)

[58] S. Altshuler, L. M. Frantz, *Reflection of atoms from standing light waves*, Phys. Rev. Lett. 17, 231 (1966)

[59] P. L. Gould, G. A. Ruff, D. E. Pritchard, *Diffraction of atoms by light: The near-resonant Kapitza-Dirac effect*, Phys. Rev. Lett. 56, 827 (1986)

[60] V. L. Hirschy, J. P. Aldridge, *A cross correlation chopper for molecular beam modulation*, Rev. Sci. Ins. 42, 381 (1971)

[61] S. Gerlich, *Interferometry and Metrology with Macromolecules*, Ph.D. Thesis, University of Vienna (2011)

[62] L. Hackermüller, K. Hornberger, S. Gerlich, M. Gring, H. Ulbricht, M. Arndt, *Optical polarizabilities of large molecules measured in near-field interferometry*, Appl. Phys. B 89, 469 (2007)

[63] M. Beck, et. al., *Evaluation of the energetic position of the lowest excited singlet state of L-carotene by NEXAFS and photoemission spectroscopy*, Biochimica et Biophysica Acta 1506, 260-267 (2001)

[64] S. Nimmrichter, K. Hornberger, H. Ulbricht, M. Arndt, *Absolute absorption spectroscopy based on molecule interferometry* , Phys. Rev. A 78, 063607 (2008)

[65] C. R. C. Wang, S. Pollack, D. Cameron, M. M. Kappes, *Optical absorption spectroscopy of sodium clusters as measured by collinear molecular beam photodepletion* , J. Chem. Phys. 93, 3787 (1990)

[66] M. B. Knickelbein, W. J. C. Menezes, *Optical response of small niobium clusters*, Phys. Rev. Lett. 69, 1046 (1992)

[67] T. Pino, N. Bounding, P. Brchignac, *Electronic absorption spectrum of cold naphthalene cation in the gas phase by photodissociation of its van der Waals complexes*, J. Chem. Phys. 111, 7337 (1999)

[68] B. Concina, M. Neumaier, O. Hampe, M. M. Kappes, *Electron emission from laser-heated fullerene dianions: Probing the repulsive Coulomb barrier* , J. Chem. Phys. 128, 134306 (2008)

[69] J.P. Hare, H.W. Kroto, R. Taylor, *Preparation and UV / visible spectra of fullerenes C60 and C70*, Chem. Phys. Lett. 177, 394398(1991)

[70] K.Hornberger, J. E. Sipe, M. Arndt, *Theory of decoherence in a matter wave Talbot-Lau interferometer*, Phys. Rev. A 70, 053608 (2004)

[71] K. Hornberger, S. Gerlich, H. Ulbricht, L. Hackermüller, S. Nimmrichter, I. Goldt, O. Boltalina, M. Arndt, *Theory and experimental verification of Kapitza-Dirac-Talbot-Lau interferometry*, New J. Phys. 11, 043032 (2009)

[72] R.E. Haufler, L. Wang, L.P.F. Chibante, C. Jin, J. Conceicao, Y. Chai, R.E. Smalley, *Fullerene triplet state production and decay: R2PI probes of C60 and C70 in a supersonic beam*, Chem. Phys. Lett. 179, 449 (1991)

[73] P. R. Bevington, D.K. Robinson, *Data reduction and error analysis for the physical sciences*, 3rd Ed., McGraw-Hill Inc.(2003)

[74] R. J. Barlow, *Statistics*, John Wiley & Sons Ldt.(1989)

[75] A. Fahr, A. Nayak, *Temperature dependent ultraviolet absorption cross sections of propylene, methylacetylene and vinylacetylene*, Chem. Physics 203, 351-358 (1996)

[76] A. Smith, *Comparison of the ultraviolet absorption cross section of C_{60} buckminsterfullerene in the gas phase and in hexane solution*, J. Phys. B 29, 4975 (1996)

[77] M. Berninger, A. Stefanov, S. Deachapunya, M. Arndt, *Polarizability measurements of a molecule via a near-field matter-wave interferometer*, Phys. Rev. A 76, 013607 (2007)

[78] J. M. Amini and H. Gould, *High Precision Measurement of the Static Dipole Polarizability of Cesium*, Phys. Rev. Lett. 91, 153001 (2003)

[79] C. R. Ekstrom, J. Schmiedmayer, M. S. Chapman, T. D. Hammond, D. E. Pritchard, *Measurement of the electric polarizability of sodium with an atom interferometer*, Phys. Rev. A 51, 3883 (1995)

[80] A. Miffre, M. Jacquey, M. Büchner, G. Trnec, J. Vigu, *Measurement of the electric polarizability of lithium by atom interferometry* , Phys. Rev. A 73, 011603(R) (2006)

[81] E. Hernandez-Marin, A. Galano, A. Martinez, *Cis Carotenoids: Colorful Molecules and Free Radical Quenchers*, J. Phys. Chem. B, 117, 4050 (2013)

[82] D. G. Harris and F. P. Zscheile, *Effects of Solvent Upon Absorption Spectra of Chlorophylls A and B; Their Ultraviolet Absorption Spectra in Ether Solution*, Botanical Gazette 104, 4, 515 (1943)

[83] H. Christen, P. A. Straub, *Über den Einfluss nichtpolarer Lösungsmittel auf Lage und Intensität von Absorptionsbanden in den Elektronenspektren apolarer Moleküln: I. Modell*, Helvetica Chimica Acta 56, 739 (1973)

[84] Z. Z. Ho, T. A. Moore, S. H. Lin, R. C. Hanson, *Pressure dependence of the absorption spectrum of beta-carotene*, J. Chem. Phys. 74, 873 (1981)

[85] A. B. Myers and R. R. Birge, *The effect of solvent environment on molecular electronic oscillator strengths*, J. Chem. Phys. 73, 5314 (1980)

[86] W. L. Liu, Z. R. Zheng, Z. F. Dai, Z. G. Liu, R. B. Zhu, W. Z. Wu, A. H. Li, Y. Q. Yang, W. H. Su, *Effect of solvent on absorption spectra of all-trans-β-carotene under high pressure*, J. Chem. Phys. 128, 124501 (2008)

[87] G. Qu, S. Li, C. Sun, T. Liu, Y. Wu, S. Sun, X. Shan, Z. Men, W. Chen, Z. Li, S. Gao, *Difference in effect of temperature on absorption and Raman spectra between all-trans-β-carotene and all-trans-retinol*, Chin. Phys. B 21, 127802 (2012)

[88] G. Britton, S. Liaaen-Jensen, H. Pfander, *Carotenoids Handbook*, Springer Basel AG (2004)

Declaration

I declare that this thesis is the product of my own work, that it has not been submitted before for any degree or examination in any other university, and that all the sources I have used or quoted have been indicated and acknowledged as complete references.

Signature:

Xiaxi Cheng

Curriculum Vitae

Education

10/2011-09/2014 **Master of Science**, Quantum Optics, Quantum Nanophysics and Quantum Information, Faculty of Physics, University of Vienna, Austria
Title of the Master's thesis:
"Exploration of matter wave interferometry in the Talbot-Lau design"
Supervisor:
Prof. Markus Arndt (University of Vienna)

10/2012-06/2013 **Student Exchange programme**, Physics and Astronomy, University of Southampton, UK

10/2008-09/2011 **Bachelor of Science** (with distinction), Faculty of Physics, University of Vienna, Austria
Title of the Bachelor's thesis:
"Bell's Theorem and experimental tests"
Supervisor:
Prof. Reinhold A. Bertlmann (University of Vienna)

09/2000-06/2008 **Matura** (Austrian university entrance qualification), Erich Fried Realgymnasium, Vienna, Austria
Title of the final thesis:
"Laser principle and generation of ultrashort light pulses"

Research Experience

09/2013-07/2014 **Master's thesis project**, Group of Prof. Markus Arndt, Faculty of Physics, University of Vienna, Austria

10/2012-08/2013 **Exchange student/Master's thesis project**, Group of Dr. Hendrik Ulbricht, Physics and Astronomy, University of Southampton, UK

07/2012-09/2012 **Summer student project**, Group of Prof. Arno Rauschenbeutel, Institute of atomic and subatomic physics, Vienna University of Technology, Austria
Project title:
"A study of atomic susceptibility and refractive index measurement of erbium doped fiber"

03/2011-06/2011 **Bachelor's thesis project**, Group of Prof. Reinhold A. Bertlmann, Faculty of Physics, University of Vienna, Austria

Publication

"Absolute absorption cross sections from photon recoil in a matter-wave interferometer",
published on **Phys. Rev. Lett.**, 112. 250402 (2014)